
Solar Wind Influences on Saturn's Magnetospheric and Auroral Dynamics

Thesis submitted for the degree of
Doctor of Philosophy
at the University of Leicester

by

Sarah V. Badman

Radio and Space Plasma Physics Group
Department of Physics and Astronomy
University of Leicester

September 2007

UMI Number: U231166

All rights reserved

INFORMATION TO ALL USERS

The quality of this reproduction is dependent upon the quality of the copy submitted.

In the unlikely event that the author did not send a complete manuscript and there are missing pages, these will be noted. Also, if material had to be removed, a note will indicate the deletion.



UMI U231166

Published by ProQuest LLC 2013. Copyright in the Dissertation held by the Author.
Microform Edition © ProQuest LLC.

All rights reserved. This work is protected against
unauthorized copying under Title 17, United States Code.



ProQuest LLC
789 East Eisenhower Parkway
P.O. Box 1346
Ann Arbor, MI 48106-1346

Abstract

Solar Wind Influences on Saturn's Magnetospheric and Auroral Dynamics

Sarah V. Badman

This thesis is concerned with the interaction between the solar wind and Saturn's magnetic and plasma environment. Four studies are presented, each investigating a different aspect of this interaction. In the first study estimates of the amount of open flux in Saturn's magnetosphere were made by analysing a sequence of images of Saturn's southern aurorae. Cassini spacecraft measurements of the upstream interplanetary conditions were then used to estimate the rate at which flux was opened on the dayside. These rates were compared with the observed amounts of open flux to deduce the average rate of flux closure between successive auroral images. Two types of flux closure event were identified: small, intermittent bursts during solar wind rarefaction regions, and large events during solar wind compressions. More auroral images were analysed in the second study as part of a statistical analysis of the location and width of Saturn's southern aurorae. The auroral oval was found typically to lie at $\sim 15^\circ$ co-latitude, with a width of $\sim 2^\circ$, although with much variability between images. This typical location and the variability in the location suggest that Saturn's aurorae are generated by the varying interaction with the solar wind, rather than by steadier corotation-enforcement currents deeper within Saturn's magnetosphere. Next, the significance of the solar wind-driven flows in both Saturn's and Jupiter's magnetospheres was investigated. Under solar wind compression conditions these flows were predicted to form a significant layer a few planetary radii wide, adjacent to the dayside magnetopause, and composed of light solar wind ions. Finally, an investigation into the effect of solar wind compressions on the emission of Saturn Kilometric Radiation (SKR) was carried out, concluding that the intensity of the SKR emissions increased during solar wind compressions, but the intensified emissions continued to pulse with the same periodicity as before the compression.

Declarations

The research undertaken during the course of this doctoral programme has led to the submission and publication of the following scientific papers:

Badman, S.V., E.J. Bunce, J.T. Clarke, S.W.H. Cowley, J.-C. Gérard, D. Grodent, and S.E. Milan: Open flux estimates in Saturn's magnetosphere during the January 2004 Cassini-HST campaign, and implications for reconnection rates, *J. Geophys. Res.*, 110, A11216, doi: 10.1029/2005JA011240, 2005.

Badman, S.V., S.W.H. Cowley, J.-C. Gérard, and D. Grodent: A statistical analysis of the location and width of Saturn's southern auroras, *Ann. Geophys.*, 24, 3533-3545, 2006.

Badman, S.V. and S.W.H. Cowley: Significance of Dungey-cycle flows in Jupiter's and Saturn's magnetospheres and their identification on closed equatorial field lines, *Ann. Geophys.*, 25, 941-951, 2007.

Acknowledgements

I am grateful to many people for their support over the course of my PhD, so I won't try to keep this short - it is after all the only part of my thesis that most people will read! Firstly I acknowledge PPARC/STFC for funding my studentship. I would also like to thank Jean-Claude Gérard, Denis Grodent, and John Clarke for providing the HST data, and Laurent Lamy, Philippe Zarka, and Baptiste Cecconi for processing the Cassini RPWS data; without these data this thesis would have been considerably shorter. I am grateful to my supervisor Stan Cowley for following Kylie's advice that it's 'better the devil you know', and thus taking me on as his student after already suffering four years as my undergrad tutor. Stan has the rare combination of seemingly endless knowledge and, importantly, the ability to convey that knowledge clearly to somewhat lesser mortals. I would also like to thank my thesis committee members Tim Yeoman and Nigel Bannister for giving their time when needed.

As many people have said before me, the members of the Radio and Space Plasma Physics group make it a friendly and supportive group to work in and there's always someone up for a drink and a curry (phaal!). A few of the group I would like to mention in particular: Emma Bunce for work and non-work chats; Steve Milan for having his door open for random questions and for 'dad-dancing'; Darren Wright for inspirational sandwiches; Rob Fear for knowing random sh*t; the girls for wearing so much pink. Special thanks to my wonderful office mates: Caitriona "Sudoku" Jackman, Jonny "Pants" Nichols, Lisa "Big Badders" Baddeley and Suzie "Imber" Imber for chocolate, gossip and listening to me swear at my computer.

Outside of work there are other lovely people who have kept me sane. LUKC, especially Rangan and Partner Stiffy, for providing an outlet. David, for sharing an enjoyment of cheese, being on MSN and writing the only song about my house. Jim and Dawn for friendship, good food and Côtes du Rhône. The wonderful Kate Weller and Snue for tea and listening to physics talk for seven years. Sas for being my bestest buddy through the good and the blue. My mum and dad for encouraging me, and Claire, Jay, Foxa and Tadpole for giving me the utter pleasure and distraction of being an aunty.

Finally, to Ade for being the gin in my tonic.

Table of Contents

Chapter 1: Introduction	1
1.1 Introduction	1
1.2 The sun and the solar wind	1
1.3 Solar and interplanetary magnetic fields	3
1.4 Corotating interaction regions	6
1.5 Planetary magnetospheres	7
1.5.1 Interaction with the solar wind	7
1.5.2 Effects of planetary rotation	8
Chapter 2: The structure and dynamics of Saturn's magnetosphere	9
2.1 Introduction	9
2.2 Saturn's magnetic field morphology and plasma populations	9
2.2.1 Saturn's internal field	10
2.2.2 The inner magnetosphere	10
2.2.3 The ring current region	11
2.2.4 The outer magnetosphere	12
2.3 Magnetospheric dynamics	12
2.4 Magnetosphere-ionosphere coupling	14
2.5 Saturn's aurora	15
2.6 Saturn Kilometric Radiation	18
Chapter 3: Instrumentation	21
3.1 Introduction	21
3.2 The Cassini orbiter and mission	21
3.2.1 The Cassini magnetometer	22
3.2.2 The Cassini Radio and Plasma Wave Science Investigation	23
3.3 The Hubble Space Telescope	24
3.3.1 Space Telescope Imaging Spectrograph	24

Chapter 4:	Open flux estimates in Saturn's magnetosphere during the January 2004 Cassini-HST campaign and implications for magnetospheric dynamics	26
4.1	Introduction	26
4.2	Cassini observations, HST images, and open flux estimates	27
4.2.1	Overview of the January 2004 HST-Cassini campaign data	27
4.2.2	Determination of the auroral boundary and open flux estimates	31
4.3	Magnetospheric dynamics during the January 2004 Cassini-HST campaign	33
4.3.1	Variation of the open flux	34
4.3.2	Magnetopause and tail reconnection rate estimates	37
4.3.3	Relationship of reconnection rates and auroral morphology	41
4.4	Summary	44
Chapter 5:	A statistical analysis of the location and width of Saturn's southern aurora	47
5.1	Introduction	47
5.2	Observations	47
5.2.1	Data description and selection	47
5.2.2	Determining the auroral boundaries and widths	49
5.3	Distributions of auroral boundaries and widths	52
5.4	Summary and discussion	54
Chapter 6:	Significance of Dungey-cycle flows in Jupiter's and Saturn's magnetospheres and their identification on closed equatorial field lines	61
6.1	Introduction	61
6.2	Equatorial flows	61
6.3	Rotational and Dungey-cycle flux transport at Jupiter and Saturn	62
6.3.1	Flux transport associated with Dungey-cycle flow	63
6.3.2	Flux transport associated with rotational flow and comparison with the Dungey-cycle	65
6.4	Identification of Dungey-cycle flows in the equatorial magnetosphere	70
6.5	Summary	73

Chapter 7: Relationship of solar wind compressions and the intensity and phasing of Saturn kilometric radiation	75
7.1 Introduction	75
7.2 Cassini measurements of interplanetary magnetic field strength and SKR	76
7.3 Drifting period of SKR	77
7.4 Examples of solar wind compression events and the corresponding SKR detections	78
7.4.1 Event 1: 2004 DOY 49-55	78
7.4.2 Event 2: 2004 DOY 133-139	80
7.4.3 Event 3: 2004 DOY 206-219	80
7.5 Discussion and Conclusions	82
Chapter 8: Summary and Future Work	85
8.1 Summary	85
8.2 Future Work	88
Appendix	90
References	91

Chapter 1

Introduction to solar-planetary physics

1.1 Introduction

Solar-planetary physics encompasses a vast range of topics from small-scale particle motions in a magnetic field to large-scale plasma flows across the solar system. This subject is concerned with studying how the Sun, the source of light and energy in the solar system, interacts with the environments of all solar system bodies. Studying these interactions not only helps us understand our ‘local’ environment but also allows us to gain information that can be used in studies of other planets outside our solar system. This thesis focuses on the magnetic and plasma interactions of the Sun with the gas giant Saturn, the sixth planet from the Sun. Following the arrival of the Cassini spacecraft at Saturn in 2004, the last few years over which this research has been carried out have been extremely important for gathering information about the Saturn system. The data obtained by the multi-instrument Cassini mission, along with telescope imaging campaigns of the planet, form the basis of much of the analysis described in this thesis. Chapter 2 gives a review of the current knowledge of Saturn’s magnetic and plasma environment, and the underlying physics. Chapter 3 introduces the instruments employed to collect the data used in this thesis. Chapter 4 describes a study of images of Saturn’s polar aurora (ultraviolet emissions of light) and how their changing size and shape relates to the concurrent solar wind conditions. Chapter 5 discusses a statistical analysis of the location and width of Saturn’s aurora, and the implications this has for theories about the origins of the aurora. The significance of the plasma flows associated with the solar wind interaction at both Saturn and Jupiter are discussed in Chapter 6. Chapter 7 then describes an investigation into how the solar wind pressure affects the emission of radio waves from Saturn’s auroral regions. Finally, Chapter 8 summarises the main findings of these studies and suggests possible future work. To begin, this chapter provides an introduction to the magnetic and plasma environments of the Sun and the planets, and the essential plasma physics required to understand them.

1.2 The Sun and the solar wind

Astronomically-speaking, the Sun is a relatively ordinary star of spectral type G2V. However, it is of vital importance to us as the source of light and energy in our solar system.

It is a massive ball of gas composed of approximately 90% hydrogen, 10% helium, and small amounts of heavier elements (Priest, 1995). The radius of the Sun (the distance from its centre to the bottom of its atmosphere) is $\sim 6.96 \times 10^8$ m - over 100 times larger than that of the Earth. The solar interior and atmosphere are illustrated in Figure 1.1. The Sun's core extends radially to one quarter of the total radius and is at such high temperature and pressure, $\sim 1.5 \times 10^7$ K and $\sim 10^{16}$ Pa respectively, that it forms a nuclear reactor, converting hydrogen into helium. These nuclear reactions are the source of the Sun's energy. The energy radiates outward from the core through a thick radiative zone. The interior temperature decreases severely outside the core such that the outermost layer of the Sun's interior, about one quarter of a solar radius thick, is a turbulent convection zone at an average temperature of $\sim 5 \times 10^5$ K. Above the convection zone lies the Sun's atmosphere, which is composed of three layers. The bottom layer, the photosphere, is at a temperature of ~ 6000 K and is only ~ 500 km thick. This layer emits most of the Sun's light. Above the photosphere is the less-dense chromosphere where the temperature drops to ~ 4200 K and above this is the corona. The temperature in the corona increases dramatically to $\sim 10^6$ K in the regions close to the Sun, hot enough to strip atoms of their electrons to form ions. The corona extends away from the Sun in all directions, filling the solar system with low-density plasma (ionized gas). This is the origin of the solar wind, the continuous existence of which was first proposed by Biermann (1951) by studying the anti-sunward direction of comet tails.

The region of space containing solar coronal plasma and controlled by the Sun is called the heliosphere and is surrounded by the local interstellar medium (LISM). Assuming that the Sun's atmosphere is in static equilibrium, the pressure of solar plasma at large distances from the Sun can be shown to reach a limiting value of $\sim 2 \times 10^{-5}$ N m⁻². If the pressure of the LISM were greater than this limiting value of the solar coronal plasma then the Sun's atmosphere would be confined by the LISM and reach hydrostatic equilibrium. However, estimates of the density and temperature of the LISM (3 cm^{-3} and 3×10^3 K, respectively) yield a pressure of $\sim 10^{-13}$ N m⁻², several orders of magnitude smaller than the limiting pressure of the solar plasma, therefore the solar atmosphere does not reach hydrostatic equilibrium. This results in the solar wind: a continual outflow of plasma from the Sun at a rate of $\sim 10^9$ kg per second (Priest, 1995). The solar wind is composed of mainly hydrogen ions and electrons, with a small number of helium ions, and fewer heavier ions. Some typical properties of the solar wind at the orbital distances of the Earth, Jupiter and

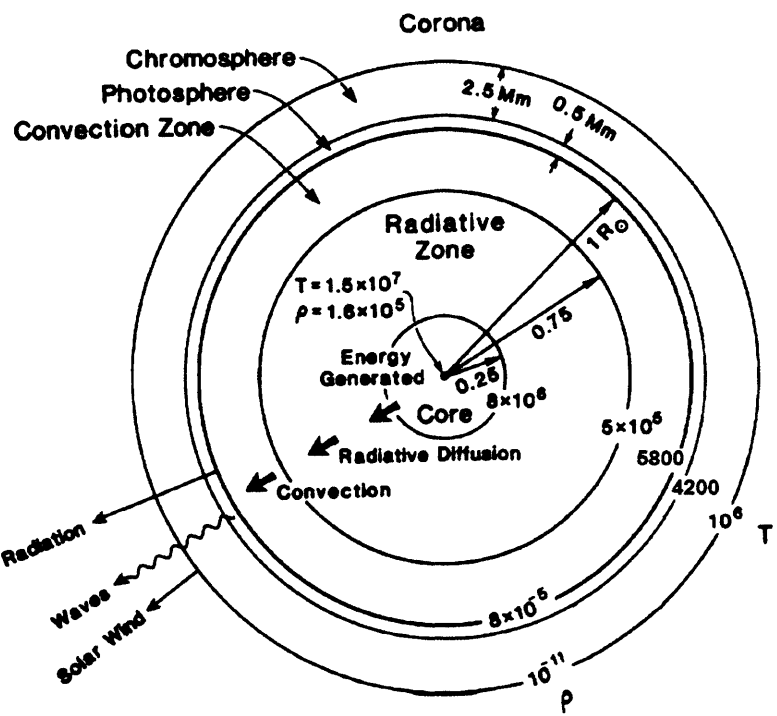


Figure 1.1 Cross section of the Sun's interior showing the different zones and the variations in temperature (T / K) and density ($\rho / \text{kg m}^{-1}$). From Priest (1995).

Table 1.1 Typical plasma and field conditions at the Earth, Jupiter, and Saturn

Typical plasma and field conditions	Earth	Jupiter	Saturn
Distance from the Sun / AU ⁽¹⁾	1	5.2	9.5
Solar wind speed / km s ⁻¹	450 ⁽²⁾	450	450
Solar wind proton density / cm ⁻³	6.6 ⁽²⁾	0.2	0.07
Solar wind dynamic pressure / nPa	2.5	0.07	0.03
IMF magnitude / nT	7 ⁽²⁾	1	0.7
Solar wind sound speed / km s ⁻¹	50	20	15
Solar wind Alfvén speed / km s ⁻¹	55	45	55
Planet radius / km (IAU mean value)	6 370	71 323	60 268
Polar radius / km	6 357	66 854 ⁽³⁾	54 364 ⁽⁵⁾
Equatorial radius / km	6 378	71 398 ⁽⁴⁾	60 268 ⁽⁵⁾
Rotation period / hr	24	9.92	10.75
Planetary equatorial surface field strength / nT	31 000	426 400 ⁽⁴⁾	21 100 ⁽⁶⁾
Magnetopause stand-off distance / R _{planet}	10 R _E ⁽⁷⁾	63 R _J ⁽⁸⁾	22 R _S ⁽⁹⁾
Bow shock stand-off distance / R _{planet}	15 R _E ⁽¹⁰⁾	84 R _J ⁽⁸⁾	30 R _S ⁽¹¹⁾

(1) 1 AU = 1.5 × 10¹¹ m

(2) Hundhausen (1995)

(3) Millward et al. (2002)

(4) Connerney et al. (1998)

(5) Trauger et al. (1998)

(6) Dougherty et al. (2005)

(7) Sibeck et al. (1991)

(8) Joy et al. (2002)

(9) Arridge et al. (2006)

(10) Peredo et al. (1995)

(11) Achilleos et al. (2006)

Saturn are given in Table 1.1. One of the properties listed in Table 1.1 is the sound speed in the solar wind, which is given by

$$C_s = \sqrt{\frac{\gamma P}{\rho}}, \quad (1.1)$$

where P is the gas pressure, ρ is the mass density of the gas and γ is the ratio of the specific heats at constant pressure and volume. For a monatomic ionized hydrogen gas, applicable to the solar wind, $\gamma = 5/3$. (For a diatomic gas $\gamma = 7/5$.) Due to the presence of the Sun's magnetic field in the solar wind (see Section 1.3 below) we must also consider the solar wind Alfvén speed, which is the speed at which a wave will propagate supported by magnetic tension along the magnetic field in the solar wind. The Alfvén speed is given by

$$V_A = \frac{B}{\sqrt{\mu_0 \rho}}, \quad (1.2)$$

where B is the magnetic field strength, and ρ is the mass density. It is evident that the average flow speed of the solar wind is an order of magnitude larger than both the sound speed and the Alfvén speed in each case shown in Table 1.1. The flow speed is also larger than the speed of fast magnetosonic waves perpendicular to the magnetic field, whose speed is related to the sound and Alfvén speeds by $v_{FAST} = \sqrt{C_s^2 + V_A^2}$. This means that the solar wind flow is supermagnetosonic.

1.3 Solar and interplanetary magnetic fields

Solar activity follows an 11-year cycle, which can be monitored by measuring the number of sunspots visible on the Sun's surface. A sunspot is a dark, cooler region of the sun's photosphere, up to thousands of kilometres in diameter, from which the magnetic field protrudes in a near-vertical direction. At solar minimum the number of sunspots is low and the solar magnetic field is approximately dipolar. Moving towards solar maximum, the number of sunspots increases and the magnetic field becomes highly disordered. After 11 years the number of sunspots has reached a minimum again and the field is reordered. Then the polarity of the field reverses and the cycle begins again. The monthly averaged sunspot number over the period 1975-2007 is shown in Figure 1.2. The times of the Pioneer-11, Voyager-1 and -2 spacecraft fly-bys of Saturn, which occurred near solar maximum, are

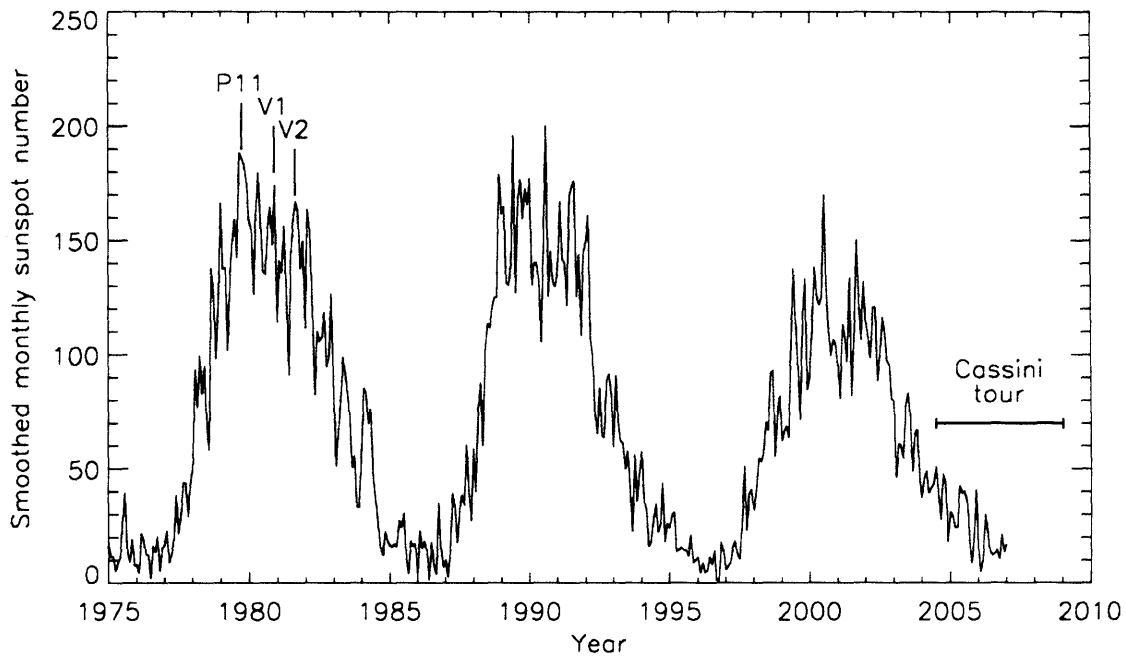


Figure 1.2 Smoothed monthly sunspot number from 1975 to 2007. The times of the Pioneer-11, Voyager-1 and -2 spacecraft fly-bys of Saturn are marked by the vertical lines. The Cassini orbital tour is shown by the horizontal line. Sunspot data is courtesy of SIDC, RWC Belgium, World Data Center for the Sunspot Index, Royal Observatory of Belgium, 1975-2007.

marked by the vertical lines. The Cassini spacecraft's tour of Saturn occurs around solar minimum, as indicated in the figure.

The Sun's magnetic field is carried out into the interplanetary space by the solar plasma, i.e. the field is frozen-in to the plasma. By considering the motion of a single particle of charge q and velocity \mathbf{v} in a magnetic field of strength \mathbf{B} the force acting on the particle is given by

$$\mathbf{F} = q \mathbf{v} \times \mathbf{B}. \quad (1.3)$$

This force is always perpendicular to \mathbf{v} and \mathbf{B} such that the particle gyrates around the field line as well as drifting along the field line. This results in a helical motion of the particle along the field line. If an electric field \mathbf{E} is also present perpendicular to \mathbf{B} then the charged particle will experience an $\mathbf{E} \times \mathbf{B}$ drift (i.e. perpendicular to both \mathbf{E} and \mathbf{B}) as well. This drift velocity is given by

$$\mathbf{v}_d = \frac{\mathbf{E} \times \mathbf{B}}{B^2}. \quad (1.4)$$

Alfvén's theorem states that if particles on a field line experience only these motions i.e. motion along the field line, around the field line due to their gyration, and an $\mathbf{E} \times \mathbf{B}$ drift, then the particles and field are frozen-in, i.e., if the particles have their gyrocentres on a particular field line then at any time later they must still lie on the same field line. In this collision-free case, Ohm's Law can be written simply as $\mathbf{E} + \mathbf{v} \times \mathbf{B} = 0$. This is illustrated in Figure 1.3. If, however, the particles experience other motions due to e.g. particle-particle collisions or a gradient or curvature of the magnetic field, then the frozen-in approximation breaks down. Gradient and curvature drifts are dependent on the charge of the particle, meaning that electrons and protons will move in opposite directions and so set up a current. Higher energy particles have stronger gradient and curvature drifts (because these drift velocities are proportional to the particle energy) relative to the $\mathbf{E} \times \mathbf{B}$ drift so the frozen-in approximation is more likely to break down. The simplest description of the breakdown of frozen-in flow is as a diffusion process where the field and plasma can move relative to each other. To determine if the plasma and field are frozen in we must then consider a simplified form of Ohm's law for a plasma of finite conductivity σ :

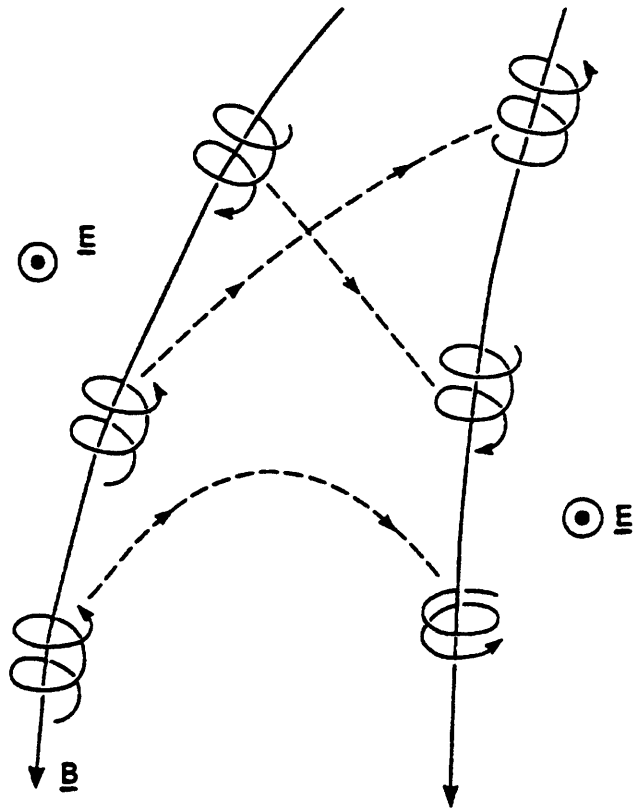


Figure 1.3 Illustration of Alfvén's frozen-in theorem, showing the motion of charged particles in the presence of a non-uniform magnetic field \mathbf{B} and a perpendicular electric field \mathbf{E} . The magnetic field line on the left shows the positions of the gyrocentres of particles at some initial time, after which the particles can move both along the field line and due to $\mathbf{E} \times \mathbf{B}$ drift. The line on the right then shows the relative positions of the particles some time later when, as they are frozen-in, their gyrocentres are still located on the field line. From Cowley (1993).

$$\mathbf{E} + \mathbf{v} \times \mathbf{B} = \frac{\mathbf{j}}{\sigma}, \quad (1.5)$$

where \mathbf{j} is the current density. Substitute into Faraday's law

$$\text{curl } \mathbf{E} = -\frac{\partial \mathbf{B}}{\partial t}, \quad (1.6)$$

and apply Ampère's law (neglecting the displacement current because we are considering a slow change over a large distance relative to the particle motion)

$$\text{curl } \mathbf{B} = \mu_0 \mathbf{j}, \quad (1.7)$$

to obtain an expression for the 'motion' of the magnetic field:

$$\frac{\partial \mathbf{B}}{\partial t} = \text{curl}(\mathbf{v} \wedge \mathbf{B}) + \frac{\nabla^2 \mathbf{B}}{\mu_0 \sigma}. \quad (1.8)$$

The first term on the right-hand side of this equation is the transport term representing how the plasma and field move together. The second term is the diffusion term. Taking the ratio of these two terms in dimensional form we obtain the magnetic Reynolds number $R_m \sim Lv\sigma\mu_0$, where L is the scale length for changes in the field or flow. If L and σ are large, as in the solar wind, then $R_m \gg 1$ and the transport term dominates i.e. the field and plasma are frozen-in. A direct consequence of frozen-in flow is that thin boundaries form between different plasma and field regions. Because there is a gradient in the magnetic field across the boundary, Ampere's law requires that a current sheet is formed at the boundary, as shown by the shaded region in Figure 1.4a. In these thin current sheets, scale lengths are short so the frozen-in approximation breaks down and the fields can diffuse into the current sheet (Figure 1.4b). Magnetic reconnection can then occur, whereby the field lines 'break' and 're-connect' with each other to form a highly bent configuration. Magnetic tension then causes the field lines to straighten, and accelerates them away from the reconnection site, allowing more field lines to diffuse in (Figure 1.4c). The magnetic force acts to accelerate the plasma up to approximately the local Alfvén speed (Eq. 1.2).

The solar wind is a magnetized plasma that is carried away from the Sun by the solar wind flow. It is composed of the interplanetary magnetic field (IMF). Near the surface of the Sun the IMF is frozen into the solar wind plasma and is carried away from the Sun by the solar wind. The radial component of the field is directed outwards (away from the Sun) in the northern hemisphere and towards the Sun in the southern hemisphere and a current sheet lies between the two hemispheres (the heliospheric current sheet (HCS)). The

(a) a dipole axis is tilted with respect to its spin axis, therefore the HCS wobbles up and down out of the ecliptic plane as the Sun rotates (e.g. Gosling and Pizzo, 1989) as shown in

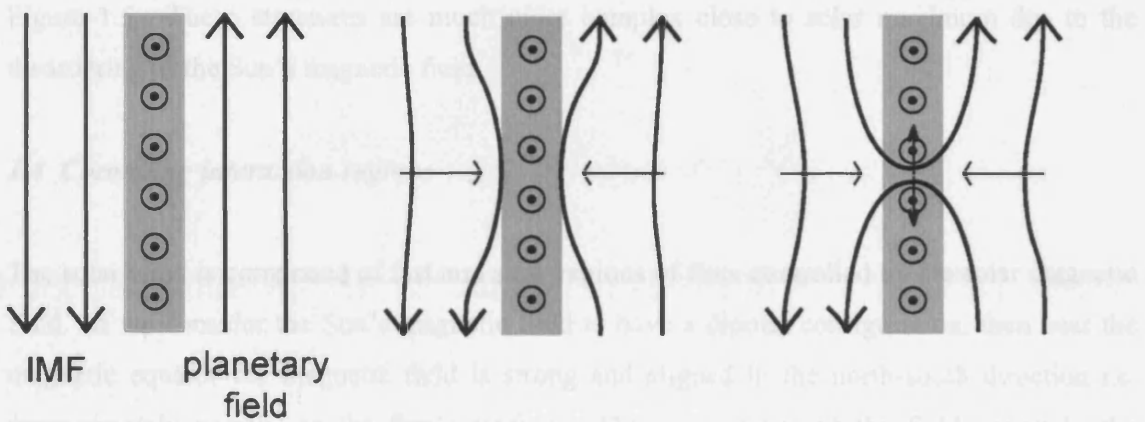


Figure 1.4 Magnetic reconnection occurring between oppositely-aligned IMF and planetary fields. In (a) the current sheet between the two fields is indicated by the grey-shaded region. (b) As the frozen-in approximation breaks down, the field diffuses into the current sheet. (c) The field lines break and reconnect with each other then move away from the reconnection site, allowing the next field lines to enter.

As the Sun's magnetic field is transported away from the Sun by the solar wind flow, it is now called the interplanetary magnetic field (IMF). Due to the rotation of the Sun the field lines do not extend radially but become wound into a spiral, first described by Parker (1958). In addition, around solar minimum when the Sun's field is approximately dipolar, the radial component of the field is directed in opposite directions in each hemisphere (e.g. away from the Sun in northern hemisphere and towards the Sun in the southern hemisphere) and a current sheet lies between the two hemispheres (the heliospheric current sheet (HCS)). The Sun's dipole axis is tilted with respect to its spin axis, therefore the HCS wobbles up and down out of the ecliptic plane as the Sun rotates (e.g. Gosling and Pizzo, 1999) as shown in Figure 1.5. These structures are much more complex close to solar maximum due to the disordering of the Sun's magnetic field.

1.4 Corotating interaction regions

The solar wind is comprised of fast and slow regions of flow controlled by the solar magnetic field. If we consider the Sun's magnetic field to have a dipolar configuration, then near the magnetic equator the magnetic field is strong and aligned in the north-south direction i.e. approximately parallel to the Sun's surface. These properties of the field constrain the coronal plasma, forming closed magnetic field arcades joining the north and south hemispheres. Further away from the Sun the field is weaker so the plasma pressure forces the field loops to open and a dense, slow ($\sim 400 \text{ km s}^{-1}$) solar wind streams away from the Sun. Nearer the poles of the Sun, the magnetic field is aligned radially so the plasma can escape from magnetically open coronal holes to form a tenuous high-speed ($\sim 700 \text{ km s}^{-1}$) wind away from the Sun (Gosling and Pizzo, 1999). These source regions of fast and slow flows are illustrated in Figure 1.6a for conditions pre-solar minimum and at solar minimum. Because the Sun's dipole is tilted with respect to the spin axis, regions of both fast and slow wind will be experienced by a fixed observer. Regions of fast solar wind run into slow flows forming compression regions as the flow speed increases. The field and plasma density are increased in compression regions. The tailing regions where the flow speed is falling and the plasma is depleted form low pressure rarefaction regions. Although the solar plasma moves radially outward, the compression and rarefaction structures rotate with the Sun hence they are called corotating interaction regions. The configuration of these structures in the equatorial plane is illustrated in Figure 1.6b.

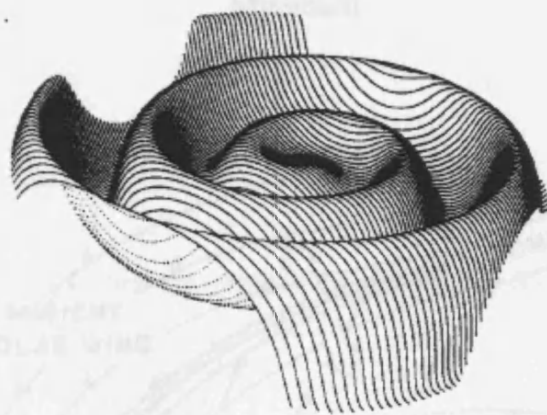


Figure 1.5 Heliospheric current sheet configuration resulting from a large tilt of the Sun's magnetic axis relative to its spin axis. From Gosling and Pizzo (1999).

1.5 Planetary magnetospheres

Having described the properties and structure of the solar wind, we must now consider what happens when the solar wind reaches an obstacle such as a planet. This thesis is concerned with the interaction of the solar wind with magnetised planets i.e. those with their own internally-generated magnetic field. Planetary magnetic field lines join the north and south magnetic poles, forming a protective bubble around the planet as shown for the Earth in Figure 1.7. This is the magnetosphere; the region that contains and is controlled by the planet's magnetic field. This concept of a magnetosphere as a closed cavity was first introduced by Chapman and Ferraro in 1931, by application of the frozen-in theorem. Using the frozen-in condition, when the solar wind encounters a magnetosphere the interplanetary and planetary plasmas and frozen-in magnetic fields cannot mix, so a current sheet forms at the boundary between the two fields (the magnetopause), and the solar wind is deflected around the magnetosphere. The impact of the solar wind squashes the magnetosphere on the dayside (sunward side) until a balance between the internal and external pressures is reached. No such simple pressure balance occurs on the nightside of the planet so the field stretches out to form a long magnetotail. A bow shock is formed upstream of the magnetosphere in the supermagnetosonic solar wind flow, across which the solar wind is slowed, compressed and heated. The region of shocked solar wind between the bow shock and the magnetosphere is the magnetosheath. In our solar system, six planets (Mercury, Earth, Jupiter, Saturn, Uranus, and Neptune) and one moon (Ganymede) are known to have intrinsic magnetic fields. The relative sizes of the known planetary magnetospheres are shown in Figure 1.8. Some important magnetic and plasma properties at the Earth, Jupiter and Saturn are summarised in Table 1.1.

1.5.1 Interaction with the solar wind

Across the magnetopause there can be high gradients in strength and direction between the interplanetary and planetary magnetic fields. This requires a current to flow at the boundary, the direction of which depends on the orientation of the planet's field and the IMF. A similar current layer is also formed in the magnetotail between the northern and southern tail lobes. The directions of these currents for the Earth's magnetosphere are indicated in Figure 1.7 by the circled dots (outward) and crosses (inward). At the magnetopause current sheet, in regions where the IMF has a component anti-parallel to the planet's field, the frozen-in

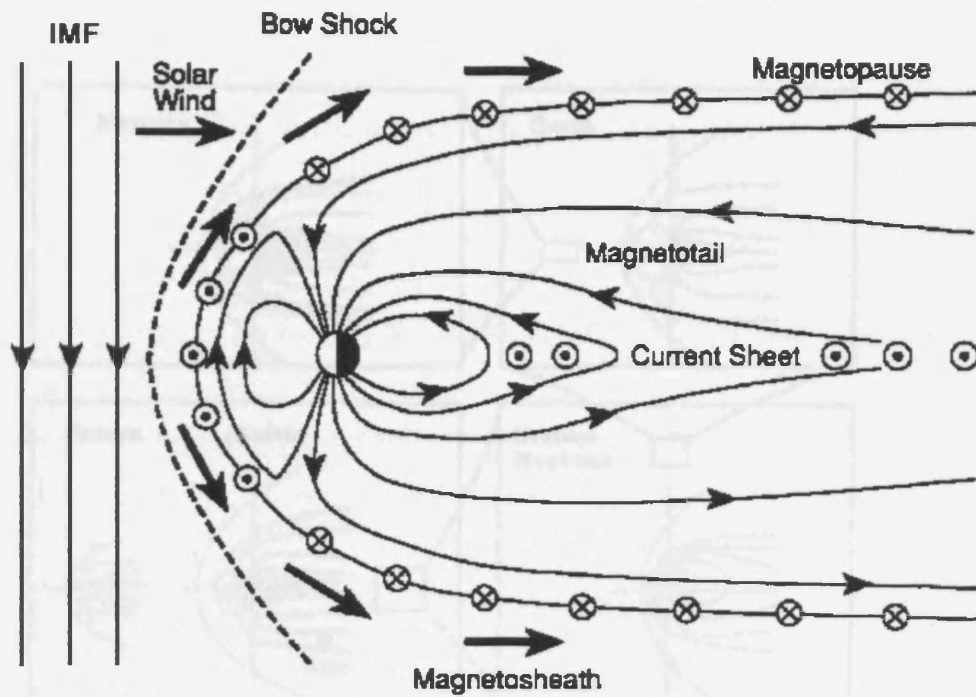


Figure 1.7 Simple schematic of the solar wind impinging on a planetary magnetosphere. The narrow solid lines represent planetary and interplanetary magnetic field lines (the planetary field polarity shown applies to the Earth). The thick short arrows show the large-scale flows of the solar wind. The directions of the magnetopause and tail currents are represented by the circled dots (out of the page / duskward) and crosses (into the page / dawnward). Adapted from Hughes (1995).

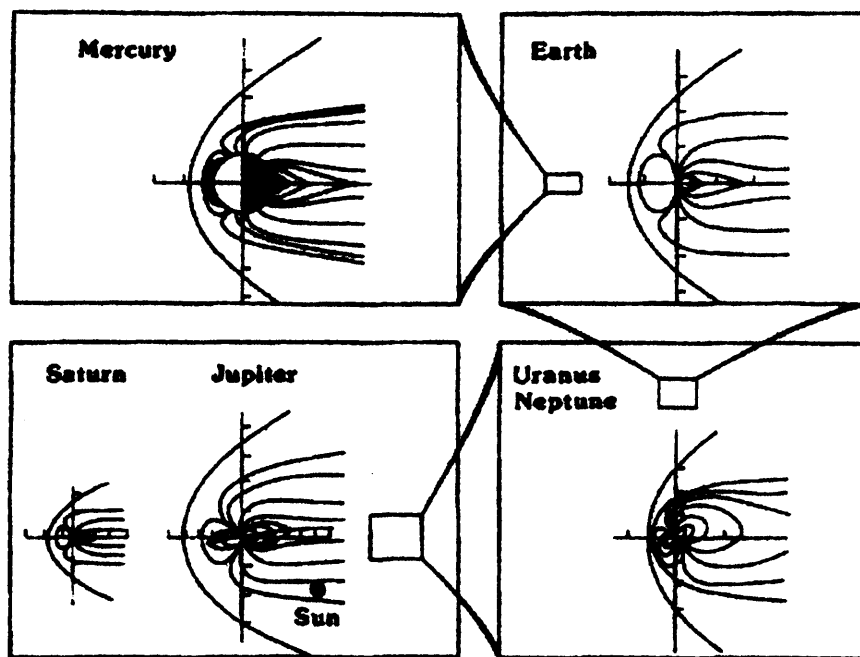


Figure 1.8 Relative sizes of planetary magnetospheres in our solar system. From Russell and Walker (1995).

theorem can break down and reconnection occurs between the two fields, as described above. The numbered field lines in Figure 1.9 show the changing configuration of field line 1 following reconnection with IMF field line 1'. Reconnection at the magnetopause produces 'open' planetary field lines that have one end at the planet and the other in the solar wind, allowing solar wind plasma to enter the magnetosphere (field lines 2 - 5). The motion of the solar wind carries the newly-opened field line anti-sunward to form an extended open magnetotail. The field line sinks towards the centre of the tail, where reconnection occurs again in the tail current sheet (field line 6). The closed field line then contracts toward the planet and convects back round to the dayside (field line 9), completing its cycle of motion. The disconnected field loop (line 7') produced by tail reconnection is lost downtail as a plasmoid. This cyclical process, driven by the solar wind, is known as the Dungey-cycle after its proposal by Dungey (1961). The Dungey-cycle is the dominant magnetospheric driving process at the Earth, but its significance is still a matter of much debate for Jupiter and Saturn, as will be discussed below and in depth in Chapter 6.

1.5.2 Effects of planetary rotation

As a planet rotates it carries its atmosphere with it due to viscous forces and waves. In the absence of any external forces the ionized upper atmosphere (ionosphere) also rotates due to collisions between the ions and the neutral atmosphere molecules, and, as the magnetic field is frozen in to the ionospheric plasma, the magnetic field will corotate with the planet. At lower altitudes in the ionosphere the collision frequency between the ions and neutrals becomes comparable to the ions' gyrofrequency so that the ions are no longer frozen in to the field. This also occurs for the electrons but at even lower altitudes (higher density of neutrals) due to their higher gyrofrequency. Jupiter and Saturn have rotation periods of ~10 hours and ~11 hours respectively, i.e. less than half that of the Earth (see Table 1.1). Their rapid rotation then has a strong influence on the dynamics of their magnetospheres relative to that at Earth. The extent to which the magnetic field corotates can be affected, however, by the presence of mass sources inside the magnetosphere, e.g. Jupiter's moon Io and Saturn's icy moons and rings. The implications of this mass-loading will be discussed in Chapter 2. As mentioned above, however, the solar wind can also transfer momentum to a magnetosphere and set up a convection cycle different to that generated by the planet's rotation. The significance of the solar wind-driving at Jupiter and Saturn relative to their rapid rotation will be discussed quantitatively in Chapter 6.

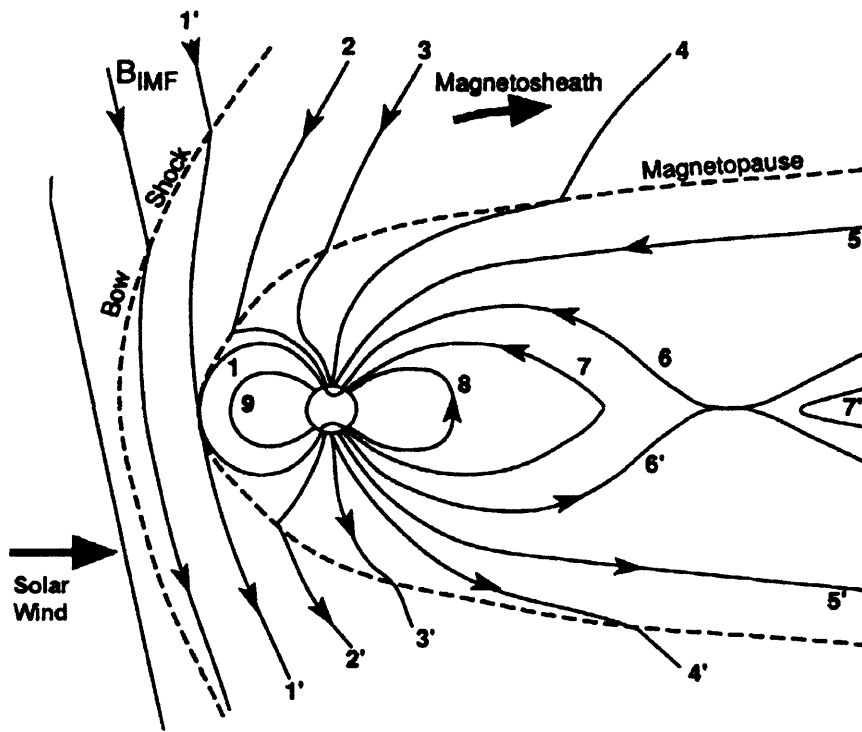


Figure 1.9 The 'open' magnetosphere. The numbers indicate the changing configuration of a magnetic field line following reconnection with an IMF field line (labelled 1') at the dayside magnetopause. From Hughes (1995).

Chapter 2

The structure and dynamics of Saturn's magnetosphere

2.1 Introduction

This chapter reviews current understanding of the structure and dynamics of Saturn's magnetosphere, including the planet's magnetic field, magnetospheric plasma populations, and coupling between the magnetosphere and the ionosphere. Saturn is one of the four gas giant planets in our solar system; the others being Jupiter, Uranus and Neptune, and is the second largest planet in the solar system after Jupiter. Models and spacecraft observations suggest that Saturn is composed of ~75% hydrogen and ~25% helium, with small amounts of heavier elements (e.g. Guillot et al., 1995). Currents within the planet's deep interior are believed to generate Saturn's magnetic field, which has, at the planet's surface, roughly the same strength as that at the Earth. The Saturn system has been visited by four spacecraft to date. The three flybys by Pioneer-11 in 1979, Voyager-1 in 1980, and Voyager-2 in 1981 covered limited local time ranges and distances in the magnetosphere but provided a highly useful data set for the first models of Saturn's magnetospheric and plasma dynamics. The ongoing orbital tour by the Cassini spacecraft, which arrived at Saturn in 2004, is significantly enhancing these models by providing data from a comprehensive range of local times and latitudes, as well as identifying new magnetospheric processes.

2.2 Saturn's magnetic field morphology and plasma populations

Saturn's magnetic field was first detected by instruments onboard the Pioneer-11 spacecraft as it flew close to Saturn in September 1979 (Acuña and Ness, 1980). This pass, which reached a closest approach of 1.35 R_S (here 1 R_S = 60 330 km) was soon followed by the flybys of the Voyager-1 and -2 spacecraft in November 1980 and August 1981 (e.g. Acuña et al., 1981; Ness et al., 1981; 1982). These early results showed that Saturn's field has a magnetic moment of ~20 000 nT R_S^3 , smaller than had been predicted by scaling from the measured fields of the Earth, Mercury and Jupiter. The magnetic moment is closely aligned with the planet's spin axis (less than 1° tilt angle), a unique feature among the planets in the solar system. The field polarity is opposite to the Earth's but the same as Jupiter's, i.e. magnetic

north is located in the north kronographic hemisphere, and magnetic south is in the southern hemisphere. The following sections give more detailed descriptions of Saturn’s magnetic field and the different regions of the magnetosphere, which are illustrated in Figure 2.1

2.2.1 Saturn’s internal field

The latest model of Saturn’s internal field was derived from Cassini magnetometer measurements taken during Saturn orbit insertion (SOI) during the interval 28 June – 14 July 2004 (Dougherty et al., 2005). This model describes the field using dipole, quadrupole and octupole components symmetric about the planet’s spin axis. These components are listed in Table 2.1 along with those previously derived from Pioneer-11 and Voyager spacecraft data for the Saturn Pioneer Voyager (SPV) model (Davis and Smith, 1990). The first two columns list the Cassini and SPV model components referenced to a Saturn radius of 60 268 km, while the third column lists those derived from the original SPV model referenced to a Saturn radius of 60 330 km, which was the standard value at that time. In this thesis both models have been employed separately for different studies. The Davis and Smith (1990) SPV model was used in the analysis presented in Chapters 4 and 5 to allow comparison with the results of other studies that also used this field model. The more recent analysis described in Chapter 6 used the latest Cassini model, employing the ‘new’ Saturn radius of 60 268 km.

2.2.2 The inner magnetosphere

The inner magnetosphere is the region within $\sim 6 R_S$ of the planet where the field lines maintain an approximately dipolar configuration. Here the field strength is greatest, and the field lines corotate with the planet due to ion-neutral collisions in the upper atmosphere. The plasma in the inner magnetosphere comes mainly from the icy moons and rings (see Figure 2.2), such as Enceladus and Dione. Cassini data has recently identified an atmospheric plume near Enceladus’s south pole as a significant source of water molecules for the E-ring (Dougherty et al., 2006; Tokar et al., 2006). The source of the plume is the region of surface cracks, or ‘tiger stripes’, discovered near the south pole (Porco et al., 2006). The gas is released at a rate of up to $\sim 300 \text{ kg s}^{-1}$, and forms a neutral water cloud between $\sim 2\text{-}10 R_S$, peaking at Enceladus’s orbital distance ($\sim 4 R_S$), which will eventually be ionized by charge exchange and electron impact and then picked up by the magnetic field (Shemansky et al., 1993; Jurac et al., 2002; Jurac and Richardson, 2005; Dougherty et al., 2006; Hansen et al.,

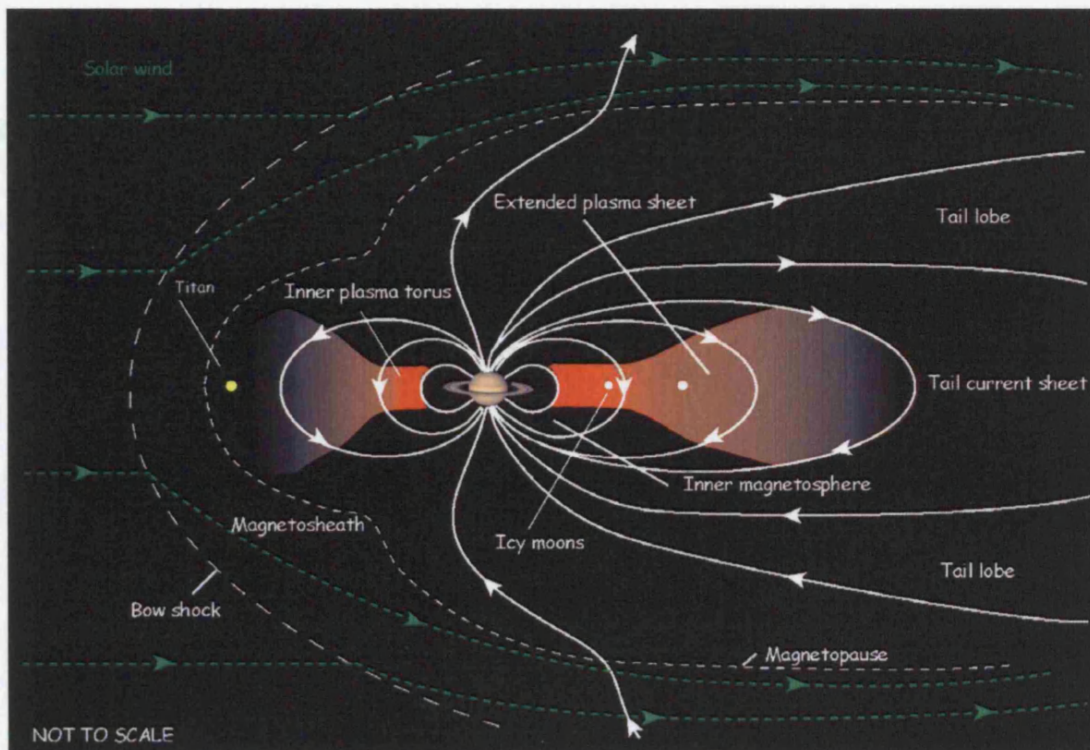


Figure 2.1 Schematic of Saturn's magnetosphere showing the different plasma regimes and the relative locations of the icy moons and Titan. Image courtesy of Dr E.J. Bunce (University of Leicester).

Table 2.1 Multipole components of the Cassini and SPV models of Saturn's magnetic field

Multipole term	Cassini model ⁽¹⁾	SPV model ⁽¹⁾	SPV model ⁽²⁾
g_1^0	21 084	21 225	21 160
g_2^0	1 544	1 566	1 560
g_3^0	2 150	2 332	2 320

(1) Dougherty et al. (2005). These values are referenced to a Saturn radius of $1 R_S = 60\,268$ km.

(2) Davis and Smith (1990). These values are referenced to a Saturn radius of $1 R_S = 60\,330$ km.

Saturn's Satellites and Ring Structure

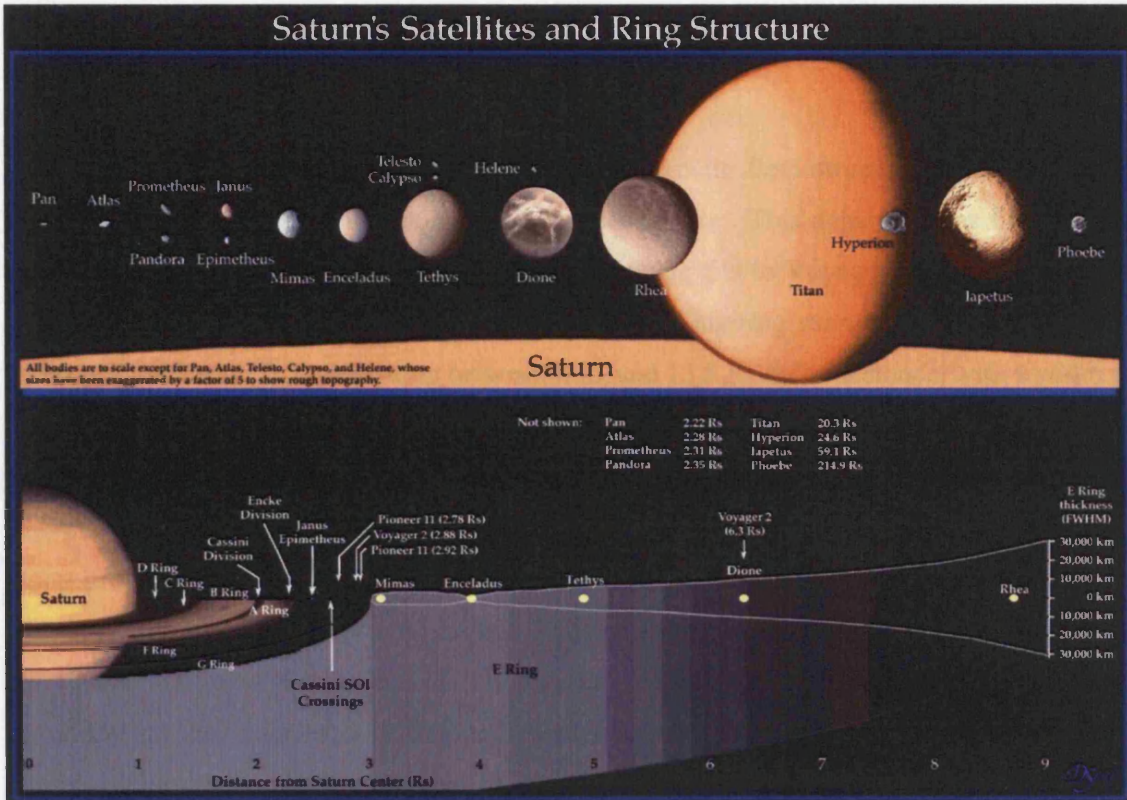


Figure 2.2 Saturn's moons and ring structure, including the relative sizes of the moons and their location relative to the rings. From NASA GSFC website.

2006). The plasma in the inner magnetosphere consequently consists mainly of water group ions, i.e. O^+ , OH^+ , H_2O^+ and H_3O^+ , with smaller numbers of protons (H^+), nitrogen ions (N^+), and molecular oxygen (O_2^+) (Young et al., 2005; Sittler et al., 2005; Williams et al., 2007). The molecular and atomic oxygen ions are dominant over the A and B rings indicating that they have an O_2 gas atmosphere (Waite et al., 2005; Young et al., 2005).

2.2.3 The ring current region

At distances greater than $\sim 6 R_S$ from Saturn, the magnetic field structure departs from the dipolar configuration exhibited in the inner magnetosphere. This departure was first noticed in the Pioneer-11 data and subsequently modelled using fits to Voyager data as a system of azimuthal currents by Connerney et al. (1981, 1983). This *ring current* region was taken to be an axi-symmetric disk, extending between $8 R_S$ and $15.5 R_S$ radial distance, with a width of $6 R_S$ across the equatorial plane. The eastward azimuthal current flowing in this disk decreases as radial distance increases. The current can be separated into two components: the 'thermal' current, which is carried by the relative motions of hot ions and electrons moving along gradient and curvature drifts on closed field lines, and the 'inertia' current associated with the rotation of the field and plasma. Other than producing the radial distension of the field lines, the magnetic effect of the current is that a northward field perturbation is introduced at the inner edge of the ring current region, which opposes the planetary field, while a southward field perturbation is introduced at the outer edge which enhances the planetary field strength.

The Connerney ring current model has since been applied to the Pioneer-11 data (Bunce and Cowley, 2003; Giampieri and Dougherty, 2004) and to a subset of Cassini orbits (Bunce et al., 2007). These studies varied the inner and outer radii of the current disk and the current density to best fit each set of data. Bunce et al. (2007) then compared these parameters with the subsolar magnetopause distance for each Cassini orbit to show how they vary with the size of the magnetosphere. They find that while the inner radius of the ring current region remains fairly constant at $\sim 6 R_S$ as the size of the magnetosphere increases, the outer radius of the region increases from $\sim 14 R_S$ to $\sim 22 R_S$. The current density parameter increased only slightly with the size of the magnetosphere, indicating a relatively constant ring current, and hence relatively constant mass sources in the magnetosphere. However, the magnetic moment of the ring current increased with its size, which is not a feature of the

thermal contribution to the ring current, thereby indicating that the inertia currents are dominant in Saturn’s ring current region. The hot ions in the ring current region are predominantly H^+ and O^+ (Sergis et al., 2007).

2.2.4 The outer magnetosphere

The outer magnetosphere extends from the outer edge of the ring current region to the magnetopause on the dayside, occupying a region a few Saturn radii wide. In this region the field strength is weakest, being the furthest from the planet, and the field lines map to high latitudes in the ionosphere. Voyager magnetometer data suggested that the field was mainly north-south aligned in the outer magnetosphere (Ness et al., 1981; 1982), but recent analysis of Cassini data has shown that the azimuthal ring current system described above can extend almost to the magnetopause on the dawnside, distorting the field lines radially to form a flattened disk of magnetic flux (Krupp et al., 2005; Arridge et al., 2007). The plasma in the outer magnetosphere originates from both internal (icy moons and rings) and external (solar wind) sources and is therefore a mixture of hot, tenuous water group ions, protons, and singly and doubly charged helium, originating from the ionosphere and the solar wind, respectively, and a dominant population of protons (Cowley et al., 2004a; Krimigis et al., 2005; Young et al., 2005). Titan, orbiting at $\sim 20 R_S$ radial distance in the outer magnetosphere, has so far proved to be a much lesser source of nitrogen ions (N^+) than was expected from its thick nitrogen atmosphere (Krimigis et al., 2005; Young et al., 2005). The relative contributions of the internal and external sources to the outer magnetosphere will be discussed in Chapter 6.

2.3 Magnetospheric dynamics

We now describe how the plasma and field dynamics in the regions described above fit within a global picture of flows in Saturn’s magnetosphere. The theoretical picture of magnetospheric dynamics that forms the basis of the analyses in this thesis is illustrated in Figure 2.3, as described by Cowley et al. (2004a). This is a view looking down on the equatorial plane of the magnetosphere with the planet marked by the circle in the centre. The sunward direction is at the bottom, dawn to the left, and dusk to the right. The solid arrowed lines indicate plasma streamlines and the dashed lines mark the boundaries between flow regimes. In the regions close to the planet the field and plasma are corotating with the planet

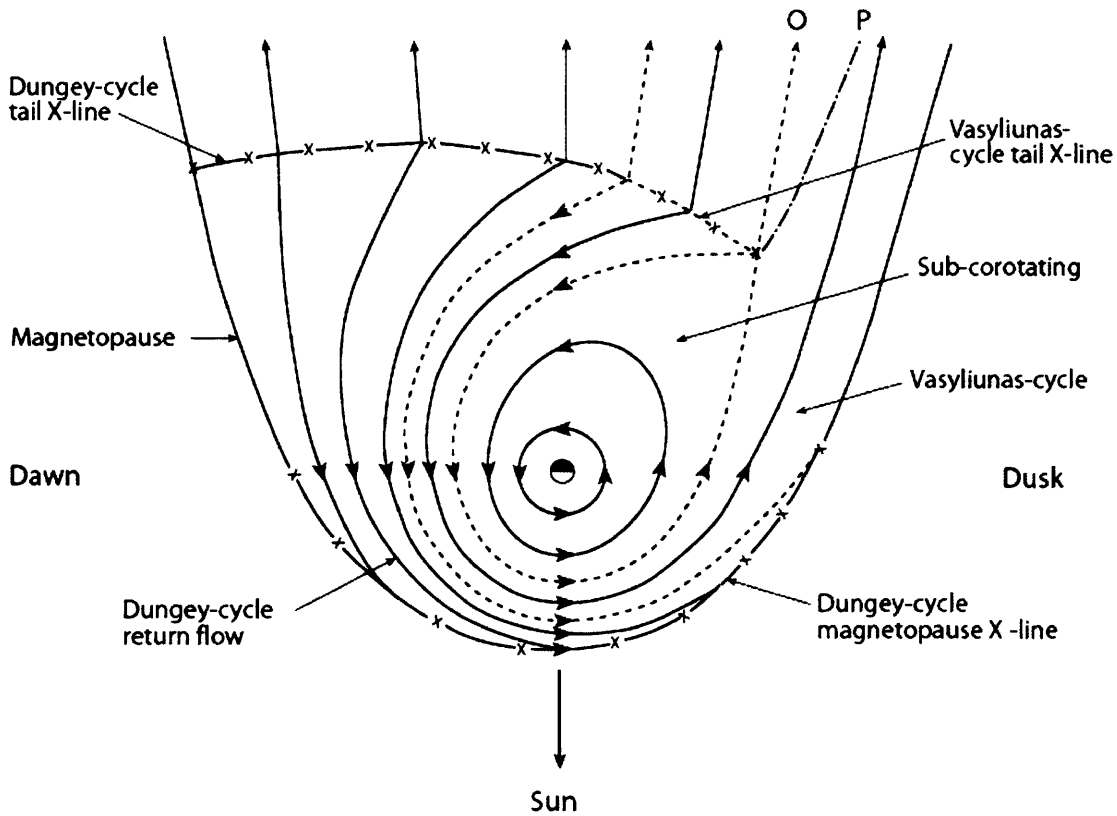


Figure 2.3 Schematic illustrating the plasma flows in Saturn's equatorial magnetosphere. The sunward direction is at the bottom of the plot, dawn to the left, and dusk to the right. The solid arrowed lines represent plasma stream lines, and the dashed lines are boundaries between flow regimes. The solid lines interspersed with Xs show the Dungey-cycle reconnection sites (X-lines), and the dashed line marked with Xs is the Vasyliunas-cycle X-line. The dashed line marked 'O' represents the path of the magnetic O-line of the plasmoid produced in the tail during the Vasyliunas-cycle. The dot-dashed line marked with 'P' represents the outer limit of the plasmoid, which asymptotes to the dusk magnetopause. From Cowley et al. (2004a).

due to ion-neutral collisions in the ionosphere, and the dynamics are strongly dependent on the pick up of plasma produced from the moon and ring sources.

At greater radial distances the flows become sub-corotational due to mass-loading from the inner plasma sources, as explained for Jupiter e.g. by Hill (1979), Pontius (1997) and Cowley et al. (2002). In the ring current region, at radial distances $\sim 6-16 R_S$, Voyager measurements suggest the field and plasma are sub-corotating at $\sim 50-60\%$ rigid corotation (Richardson, 1986; Richardson and Sittler, 1990). The plasma diffuses outward under centrifugal forces, slowing as it attempts to conserve angular momentum, and causing the frozen-in field lines to stretch radially outward too. This stretching effect is more pronounced on the nightside because the dayside magnetosphere is constrained by the solar wind pressure. An azimuthal field component is also introduced, directed westward in the northern hemisphere and eastward in the southern hemisphere, as the plasma and field lines lag behind corotation.

The mass picked up from the internal sources must be lost downtail via a field reconfiguration resulting in release of a plasmoid. One mechanism for this is that the closed field lines become stretched as they pass through dusk towards the nightside until reconnection occurs across the tail current sheet and a plasmoid is pinched-off. This reconnection site, or X-line, is shown in Figure 2.3 by the dashed line marked with Xs. The disconnected plasmoid is lost downtail, while the closed field line is accelerated back toward the dayside via dawn, where it again becomes mass-loaded, slows, and stretches out downtail post-dusk. This cycle of behaviour is known as the Vasyliunas-cycle after it was first suggested for Jupiter by Vasyliunas (1983). A consequence of this is that the middle sub-corotating region is enclosed by a layer of faster ($\sim 70\%$ rigid corotation, e.g. Richardson, 1986; Richardson and Sittler, 1990; Szego et al., 2005; Hartle et al., 2006) mass-depleted flux tubes on the dawnside of the outer magnetosphere, which then slow as they pass through noon and become mass-loaded.

The final contribution to the flow is the solar wind-driven Dungey cycle, as described in section 1.5.1 for the Earth. The planet's field lines are opened into the solar wind at the dayside magnetopause X-line, marked in Figure 2.3 by the solid line with Xs, then are carried slowly anti-sunward over the pole in a single cell convection pattern by the solar wind motion, before sinking towards the tail current sheet. In Saturn's rapidly-rotating

environment, the Dungey-cycle tail reconnection line is displaced towards the dawnside due to the Vasyliunas-cycle outflow on the dusk side, as shown in Figure 2.3. Once tail reconnection has occurred, the newly-closed field lines are accelerated back round toward the dayside via dawn, due to the nature of the planet’s rotation. The disconnected field line is lost down tail. The ionospheric footprints of the open field lines are moving anti-sunward at $\sim 200 \text{ m s}^{-1}$, and twisting at $\sim 30\%$ of Saturn’s angular velocity (Isbell et al., 1984; Cowley et al., 2004b; Stallard et al., 2004). The Dungey-cycle return flows on the dawn side are accelerated to $\sim 80\%$ of corotation speed e.g. Cowley et al. (2004b). Note that both the Vasyliunas- and Dungey-cycle processes are illustrated in Figure 2.3 in the steady-state but may be expected to be intermittent over time and may or may not occur simultaneously.

2.4 Magnetosphere-ionosphere coupling

The corresponding flows in Saturn’s ionosphere are shown in Figure 2.4, taken from Cowley et al. (2004a). This is a view looking down onto the northern ionosphere, with the sunward direction at the bottom, dawn to the left and dusk to the right. The solid arrowed lines again represent plasma streamlines and the dashed lines mark the boundaries between flow regimes. The circled dots and crosses represent upward and downward directed field-aligned currents, respectively. Starting from the outside of the figure which corresponds to $\sim 30^\circ$ co-latitude, this region maps to the inner magnetosphere where the field is corotating with the planet. The next streamlines at higher latitudes map to the region in the magnetosphere where corotation begins to break down. Moving further poleward there is a region of Vasyliunas-cycle flow, which is slow and mass-loaded on the dusk side and faster as it returns on the dawnside. The next dashed line marks the boundary between open and closed field lines with the magnetopause and tail X-lines labelled. On the dawnside of the polar cap (the polar open flux region) there is an additional region of Dungey-cycle return flow i.e. newly-closed field lines.

At the radial distance where corotation breaks down in the magnetosphere the footprints of these magnetic field lines in the ionosphere will also slow down. In the rest frame of the rotating planet there is consequently an ion velocity drift in the westward direction in the ionosphere i.e. opposite to the sense of the planet’s rotation. This velocity drift in the presence of the planet’s field (upward in the northern hemisphere, out of the page in Figure 2.4) results in an equatorward electric field and associated current. Moving to lower latitudes, the relative drift decreases to zero as the plasma approaches rigid corotation, such

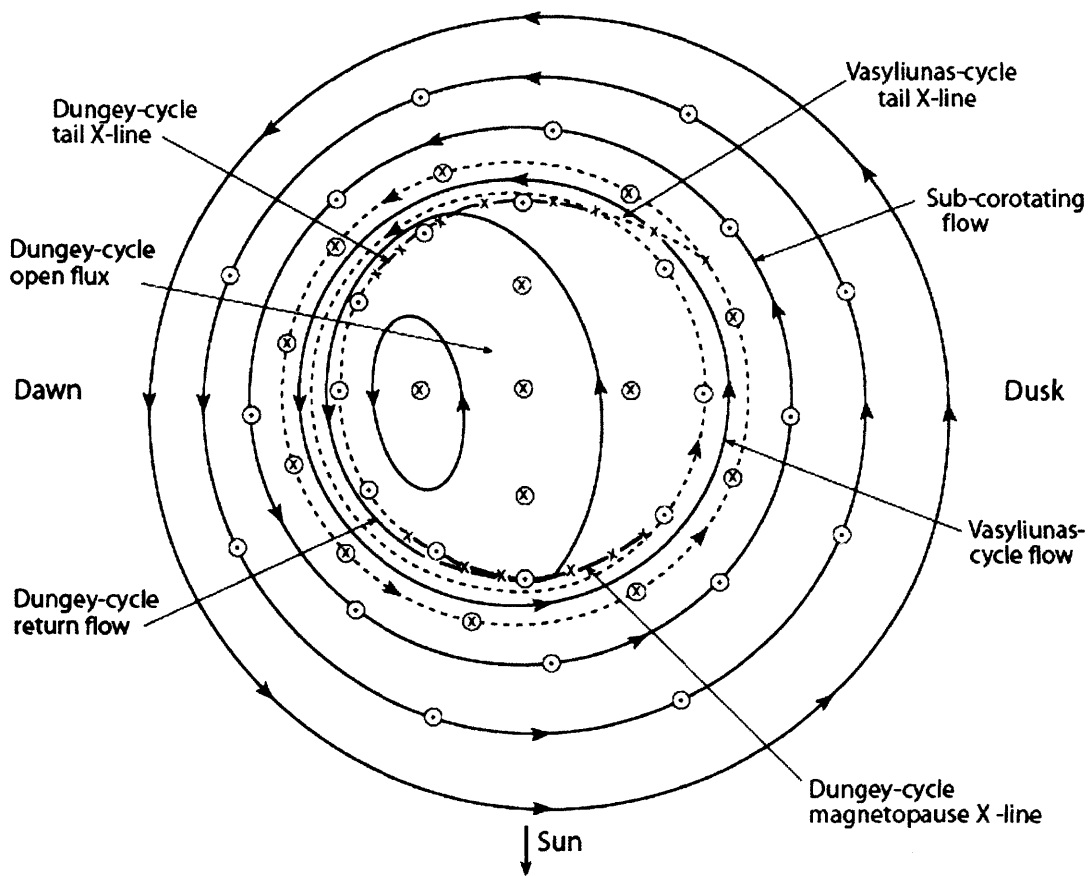


Figure 2.4 Schematic of the flows in Saturn's northern polar ionosphere, viewed looking down on the pole with the sunward direction at the bottom of the plot, dawn to the left, and dusk to the right. The outermost circle corresponds to a co-latitude of $\sim 30^\circ$ from the pole. The solid lines show plasma streamlines and the dashed lines mark the boundaries between flow regimes. The circled dots and crosses represent upward and downward directed field aligned currents, respectively. The Dungey-cycle reconnection lines are marked with the solid lines interspersed with Xs, and the Vasyliunas-cycle X-line is shown by the dashed line marked with Xs. From Cowley et al. (2004a).

that the electric field is reduced at the boundary between the sub-corotating and corotating field lines. Current continuity requires an upward-directed current to flow at this boundary. This ring of upward field-aligned currents is shown as the outermost set of circled dots in Figure 2.4. The reversal in sense of the azimuthal (‘lagging’) field components across the equatorial plane requires the current to flow radially outward in the equatorial plane, acting to spin-up the sub-corotating plasma via the magnetic curvature ($\mathbf{j} \times \mathbf{B}$) force. The currents return along more distant field lines to complete the current circuit. The ring of circled crosses at higher latitude in Figure 2.4 represents this downward region of return current.

At higher latitudes there is another ring of upward FAC at the boundary between the slow-moving open field lines (being dragged anti-sunward by the solar wind) and the faster sub-corotating closed field lines at lower latitudes. The difference in velocity on open and closed field lines is also greater on the dawn side than dusk due to the sense of the planetary rotation hence the current will be stronger on the dawn side, represented by the increased number of circled dots in Figure 2.4. These two regions of upward-directed currents are important for the generation of aurora and will be discussed below.

2.5 Saturn’s aurora

The first indications that auroral emissions occur in Saturn’s polar regions were obtained by the ultraviolet (UV) photometer onboard the Pioneer-11 spacecraft during its flyby in 1979 (Judge et al., 1980), and remotely from observations by the IUE spacecraft (Clarke et al., 1981; McGrath and Clarke, 1992). The first unambiguous detections were made by the two Voyager spacecraft in 1980 and 1981, revealing emissions poleward of $\sim 12^\circ$ co-latitude in both hemispheres that were extended in longitude, but with some localised brightenings (Broadfoot et al., 1981; Sandel and Broadfoot, 1981; Sandel et al., 1982). Subsequent observations have been made of both the northern and southern hemisphere aurorae using the Faint Object Camera, Wide Field Planetary Camera 2, and Space Telescope Imaging Spectrograph (STIS) instruments on the Hubble Space Telescope (HST) (e.g. Gérard et al., 1995, 2004; Trauger et al., 1998; Cowley et al., 2004a; Prangé et al., 2004; Grodent et al., 2005). These have revealed some common features, mainly thin circumpolar auroral arcs and diffuse auroral patches, lying at co-latitudes between $\sim 10^\circ$ and $\sim 20^\circ$, and often enhanced at dawn relative to dusk. However, the HST images have also revealed considerable variability in the location of the observed features, and in the intensity of the emissions, which ranges

from below an instrumental threshold of a few kR to over 120 kR. Examples of Saturn’s variable southern hemisphere aurorae are shown in Figure 2.5, in a set of three composite images acquired by the Hubble Space Telescope during January 2004.

Saturn’s aurorae are commonly observed at UV wavelengths corresponding to Lyman emission lines from atomic hydrogen, and Lyman and Werner emission bands from molecular hydrogen, in Saturn’s upper atmosphere. Saturn’s aurora have also been observed in the infrared (IR) at the H_3^+ emission line (3.953 μm), but this emission is relatively low so images are difficult to obtain (e.g. Stallard et al., 2007; and references therein). There is also emission at visible wavelengths (410 nm, 434 nm, 486 nm, and 656 nm) corresponding to the hydrogen Balmer lines, however this emission is fainter than the reflected sunlight from Saturn’s atmosphere so the aurorae at visible wavelengths are not actually ‘visible’. Saturn’s peak auroral emission is H Lyman- α at a UV wavelength of 121.5 nm, corresponding to photons with ~ 10 eV energies. These emissions are generated by \sim keV electrons precipitating into the atmosphere, where the energy conversion has an efficiency of 15-20% (e.g. Shemansky and Ajello, 1983; Waite et al., 1983; Rego et al., 1994). For an aurora of brightness 10-100 kR, as observed by HST, the energy input required is ~ 1 -10 mW m^{-2} . (1 Rayleigh is equivalent to 10^6 photons crossing an area of 1 cm^2 in all directions per second.) The currents that drive the aurora must be sufficient to satisfy this energy requirement, as will be discussed below.

We now describe in detail how the current systems described in section 2.4 relate to the generation of Saturn’s aurora. An auroral oval can be generated either as a result of the interaction between a planet’s magnetosphere and the solar wind, or internally due to processes associated with the enforcement of planetary rotation on magnetospheric plasma. Aurorae associated with the solar wind interaction are located at and near the boundary between open and closed field lines surrounding the magnetic pole, such that their latitudinal position varies with the amount of open flux in the system, as observed at Earth (e.g. Milan et al., 2003, 2004, 2007). These aurorae consist of ‘discrete’ forms associated with the upward-directed field-aligned currents generated by magnetosphere-ionosphere momentum exchange (see Figure 2.4), carried by precipitating accelerated magnetospheric electrons, together with ‘diffuse’ aurorae produced by charged particle precipitation from regions of hot magnetospheric plasma. Hot plasmas are generated, for example, in regions downstream from reconnection sites associated with the Dungey-cycle or Vasyliunas-cycle. These auroral

... and will generally display the characteristics of the aurora as described by Tokunaga and Cowley (2005).

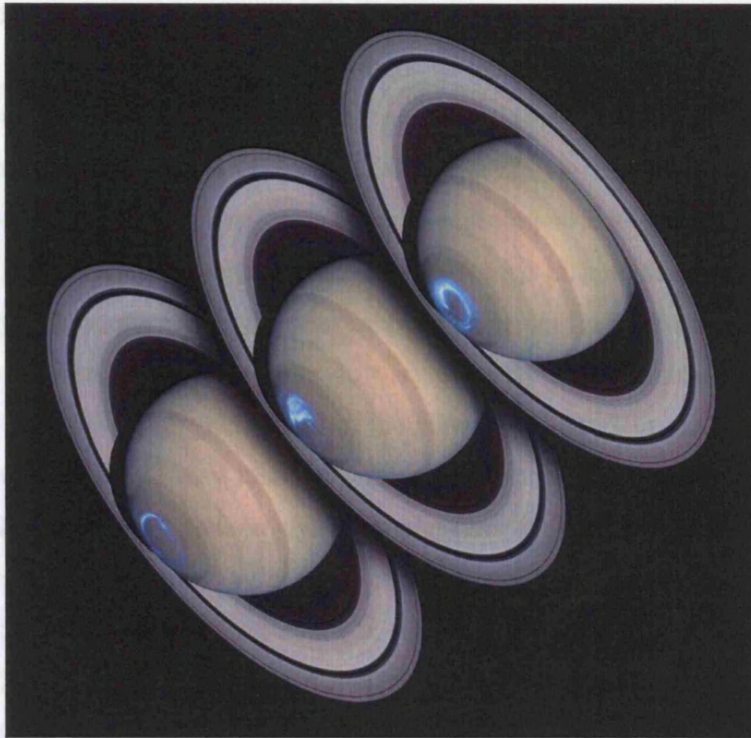


Figure 2.5 Composite of three images of Saturn's southern UV aurora, imaged by the HST, and superposed on a visible image of the planet's disk. These images were acquired during the January 2004 imaging campaign. Image courtesy of Prof. J.T. Clarke (Boston University).

components are strongly modulated by prevailing solar wind conditions, and will generally also present persistent asymmetries in local time (e.g. Jackman and Cowley, 2006).

Aurorae associated with planetary rotation are firstly related to the field-aligned current system generated by angular momentum transfer between the planetary atmosphere and the magnetospheric plasma (Hill, 1979). This is the region of upward field-aligned current at lower latitudes shown in Figure 2.4, which maps to the inner magnetospheric region where near-rigid corotation breaks down, and may produce ‘discrete’ aurorae if the currents are sufficiently strong (e.g. Cowley and Bunce, 2001; Hill, 2001). If these currents flow deeply inside the near-axisymmetric magnetosphere then local time effects are expected to be weak, and they will also be relatively steady over time if internal plasma sources and transport are relatively steady. These properties then describe the principal features exhibited by the jovian main auroral oval, though these aurorae do vary strongly with planetary longitude due to asymmetries in the internal magnetic field of the planet (e.g. Grodent et al., 2003). Transient modulation of these aurorae may result from magnetospheric compressions and expansions due to rapid changes in solar wind dynamic pressure, if these are sufficient to alter the magnetospheric plasma angular velocity profile in the relevant region (Southwood and Kivelson, 2001; Cowley and Bunce 2003a,b; Gong and Hill, 2005; Nichols et al., 2007; Cowley et al., 2007). Diffuse aurorae associated with internal processes may also occur at higher latitudes due to the Vasyliunas-cycle of internal plasma mass loss via down-tail plasmoid ejection. These aurorae will occur in the region directly equatorward of those associated with the Dungey-cycle, and will also generally exhibit local time asymmetries imposed by the flow of the solar wind (Cowley et al., 2004a). The principal distinction from the tail reconnection process associated with the Dungey-cycle is that Vasyliunas-cycle reconnection does not involve any change in the amount of open flux present in the system.

In general, these solar wind and internally generated processes can occur simultaneously, potentially resulting in two auroral regions, one located in the vicinity of the open-closed field line boundary and the other at lower latitudes mapping to the corotation-breakdown region, as depicted in Figure 2.4. However, Cowley and Bunce (2003c) presented an empirical model of corotation-related coupling currents in Saturn’s magnetosphere, based on Voyager spacecraft velocity data, and concluded that the large-scale upward-directed currents, flowing at $\sim 20^\circ$ - 25° co-latitude, are too weak to generate bright (tens of kiloRayleigh) aurorae. However, smaller-scale flow features which are perhaps due to moon

effects may produce weak (~ 1 kR) narrow auroral rings or partial rings at co-latitudes $\sim 20^\circ$. This model was subsequently extended to higher latitudes by Cowley et al. (2004b), showing that the upward current at the open-closed field line boundary is expected to be of sufficient intensity to generate aurorae of a few tens of kR, mapping to $\sim 14^\circ$ co-latitude in the southern hemisphere. Corresponding features in the northern hemisphere are expected to be located $\sim 1.5^\circ$ closer to the pole due to the inter-hemispheric asymmetry in the magnetic field associated with the quadrupole internal field component (Davis and Smith 1990; Cowley and Bunce, 2003c). On the basis of these results, Cowley et al. (2004b) concluded that Saturn’s observed aurorae are more likely to be associated with the open-closed field line boundary and the solar wind interaction, rather than with the corotation-enforcement current system.

Further to these analyses, images of Saturn’s aurora acquired during January 2004 as part of a joint Cassini-HST campaign showed a strong auroral response to the arrival of a solar wind CIR compression at Saturn (Clarke et al., 2005; Grodent et al., 2005; Kurth et al., 2005). Under these circumstances, when the dynamic pressure (principally the density) and the magnetic field strength of the solar wind are strongly enhanced, the auroral emission expanded significantly poleward in the nightside and dawn sector, before forming a bright spiral structure extending from dawn to later local times. Cowley et al. (2005a) proposed that these events are formed by bursts of tail reconnection excited by the sudden magnetospheric compression produced by the arrival of the leading (‘forward’) shock of the CIR compression region. Similar shock-induced auroral events are occasionally observed at Earth involving rapid closure of a significant fraction of the open magnetic flux in the tail (e.g., Boudouridis et al., 2003, 2004; Milan et al., 2004; Meurant et al., 2004).

It is obvious from the above discussion that remote observations of Saturn’s UV aurorae provide an important diagnostic tool for understanding magnetospheric dynamics. Images of the aurora provide a two-dimensional snapshot of Saturn’s global magnetospheric configuration. Much of the work in this thesis is guided by analysis of auroral emissions, not only at UV wavelengths, but also radiowave, as will now be described.

2.6 Saturn Kilometric Radiation

Radio emissions from a planet’s auroral regions are another useful diagnostic of magnetospheric dynamics. Such auroral radio emissions have been detected at the Earth,

Jupiter, Saturn, Uranus and Neptune. These emissions are non-thermal (i.e. not blackbody radiation) O (ordinary) or X (extraordinary) mode circularly-polarized waves emitted from the planet’s polar regions. The average frequency spectra of the radio emissions from the different planets are shown in Figure 2.6. Those of interest here are Saturn Kilometric Radiation (SKR) emissions, which cover a broad frequency range of ~100-1000 kHz, with a spectral peak at ~100-400 kHz, just higher than that of the Earth’s auroral radio emissions (Zarka, 1998). Galopeau et al. (1995) determined the likely source location of SKR in Saturn’s northern and southern ionospheres, using constraints imposed by the wave properties. They found a region in both hemispheres centred on ~09 LT, extending from ~60° latitude to the pole, as illustrated in Figure 2.7. More recent measurements using Cassini’s direction-finding capabilities have confirmed these regions as likely sources e.g. Cecconi et al. (2007). The emission from the northern (southern) hemisphere is mostly right-hand (left-hand) polarised due to the sense of the magnetic field, although low emissions of the opposite polarisation have been detected (e.g. Cecconi et al., 2007). This is consistent with X-mode electromagnetic wave generation.

The most plausible theory of how auroral radio emissions are generated is the cyclotron maser instability (CMI) mechanism (e.g. Wu and Lee, 1979). In this generation mechanism the wave is excited by energy lost from electrons as they are accelerated down magnetic field lines. This theory explains the observations that the radio waves are emitted from auroral regions, where there is strong magnetic field and a population of field-aligned accelerated electrons. Waves generated in this way satisfy the measured condition that the waves have a low frequency cut-off at the local electron cyclotron frequency (Zarka and Kurth, 2005), which then provides a measure of the local magnetic field.

The intensity of the emitted SKR is modulated by the rotation of the planet (Desch and Kaiser, 1981) and so provides a means of measuring Saturn’s rotation period in the absence of any fixed surface features. Saturn’s radio rotation period was deduced from 267 days of Voyager SKR measurements in 1980-1981 to be 10 h 39 m 24 s \pm 7s (Desch and Kaiser, 1981a). Analysis of later Ulysses data found that this period had slowed slightly and was fluctuating by ~1% (Galopeau and Lecacheux, 2000). The slowing (to 10 h 45 m 45 s during Cassini approach) and fluctuation of the SKR period has been confirmed by ongoing Cassini measurements e.g. Gurnett et al. (2005) and Kurth et al. (2007). A likely explanation for the SKR periodicity is that there may be an ‘active’ planetary longitude, perhaps due to a

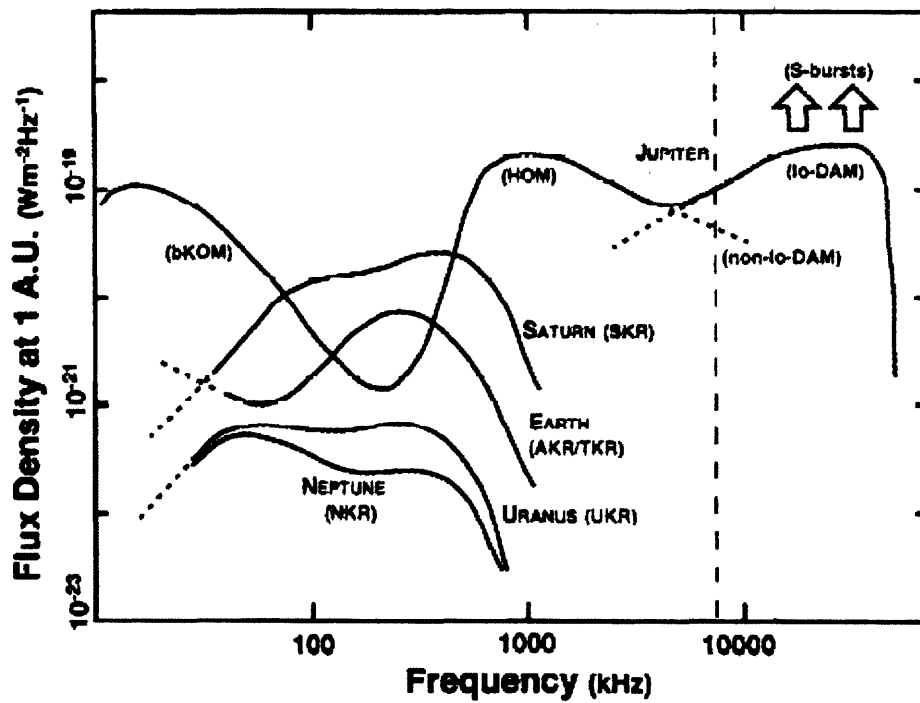


Figure 2.6 Comparative spectra of auroral radio emissions from the Earth, Jupiter, Saturn, Uranus and Neptune. The average emission levels are shown, normalised to a distance of 1 AU from the source. From Zarka (1998).

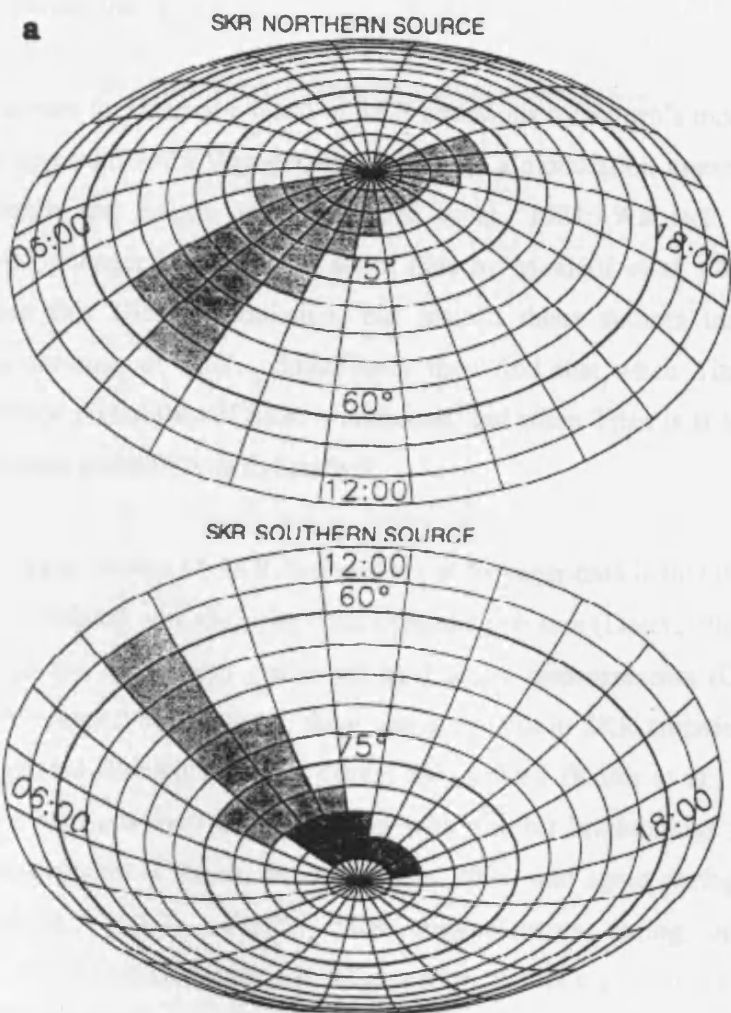


Figure 2.7 SKR source locations in Saturn's northern and southern hemispheres. From Galopeau et al. (1995).

magnetic anomaly, which excites the CMI when it passes through the SKR source location in local time. Explanations for the fluctuations in the period are varied, and include differential rotation across latitudes (Dessler, 1985), slippage of field lines relative to the planet’s interior (Gurnett et al., 2005), and variations in the solar wind velocity which affect Kelvin-Helmholtz instabilities at the magnetopause connected to the SKR source (Galopeau and Lecacheux, 2000; Cecconi and Zarka, 2005).

There is evidence for internal control of SKR emissions by Saturn’s moons. Analysis of the SKR power spectrum from Voyager data indicated a modulation associated with the orbit of Dione (Desch and Kaiser, 1981b; Gurnett et al., 1981; Warwick et al., 1982). Subsequent analysis of longer intervals of Cassini data by Menietti et al. (2007) has been unable to reproduce this Dione modulation, but instead these authors identify Titan’s influence on the occurrence of SKR. Specifically they find that when Titan is at local midnight the occurrence probability of SKR is increased, and when Titan is at local noon and afternoon the occurrence probability is diminished.

Another persistent feature of SKR first noticed in Voyager data is that the intensity of the emitted SKR is correlated with the solar wind dynamic pressure (Desch, 1982; Desch and Rucker, 1983). This has again been confirmed by Cassini measurements (Gurnett et al., 2005). During the Voyager 2 Saturn flyby, there was a dropout in SKR emission for about 2 days while Saturn passed through Jupiter’s distant magnetotail (Kurth et al., 1983). SKR intensifications were also observed in conjunction with auroral brightenings following the arrival of a CIR compression at Saturn during January 2004, and again during Saturn orbit insertion (Kurth et al., 2005). Further SKR enhancements during magnetospheric compressions have been associated with tail reconnection events e.g. Bunce et al. (2005b), Jackman et al. (2005), Mitchell et al. (2005), Jackman et al. (2007). These observations lend weight to theories of solar wind driving of SKR, and a survey of the effects of solar wind compressions on SKR will be examined in detail in Chapter 7.

Chapter 3

Instrumentation

3.1 Introduction

Understanding Saturn's magnetospheric and auroral dynamics requires data to guide and augment the physical theories of the driving processes. The data used in this thesis can be categorised into two types: in situ and remote sensing data. In situ data is essential to understand local processes by making precise measurements at the location of a spacecraft, while remote sensing is a means of studying global processes from a distance by detecting emissions at various wavelengths. The Cassini spacecraft provides in situ data from Saturn's magnetosphere using a variety of field and plasma instruments. The studies presented in Chapters 4 and 7 of this thesis use in situ magnetic field measurements from the Cassini magnetometer. Chapter 7 also uses remote sensing data in the form of Cassini Radio and Plasma Wave Spectrometer detections of SKR (radiowave emissions). The studies described in Chapters 4 and 5 use another type of remote sensing data: images of Saturn's ultraviolet aurora, obtained by the Hubble Space Telescope. The following sections describe these instruments and the data they provide.

3.2 The Cassini orbiter and its mission

The Cassini-Huygens spacecraft was launched from Cape Canaveral, Florida in 1997 and completed flybys of Venus, the Earth and Jupiter before arriving at Saturn in July 2004. The Cassini mission is a joint project by the American (NASA), European (ESA), and Italian (ASI) space agencies to explore the Saturn system, including its moons, rings, atmosphere, composition and magnetosphere. Cassini-Huygens is the largest interplanetary spacecraft ever built, measuring 6.7 m high and 4 m wide (see Figure 3.1). In December 2004 the Huygens probe was released to descend through the atmosphere of Saturn's largest moon Titan while the Cassini orbiter continued its tour of Saturn. Cassini's orbital path is continuously evolving, including equatorial orbits into the distant tail and close polar orbits to allow all regions of the magnetosphere to be studied. The spacecraft carries 12 science instruments to gather information on Saturn's environment, some of which are labelled in Figure 3.2. Those that provided data used in this thesis are described below.



Figure 3.1 The Huygens probe (gold dome) being mounted onto the Cassini spacecraft prior to spacecraft testing and launch. Courtesy NASA/JPL-Caltech.

3.2.1 The Cassini-Huygens spacecraft

The Cassini-Huygens spacecraft contains several instruments, including a magnetometer (MAG) mounted halfway along the 11 m long boom, partially visible in Figure 3.2, and a vector field-of-view magnetometer, which is also capable of acting as a scalar magnetometer, mounted at the far end of the boom. The long boom is used to distance the magnetometer from the spacecraft and any self-field or field perturbations. The magnetometer is mounted on a boom that is 11 m long and is used to distance the magnetometer from the spacecraft and any self-field or field perturbations. The magnetometer is mounted on a boom that is 11 m long and is used to distance the magnetometer from the spacecraft and any self-field or field perturbations.

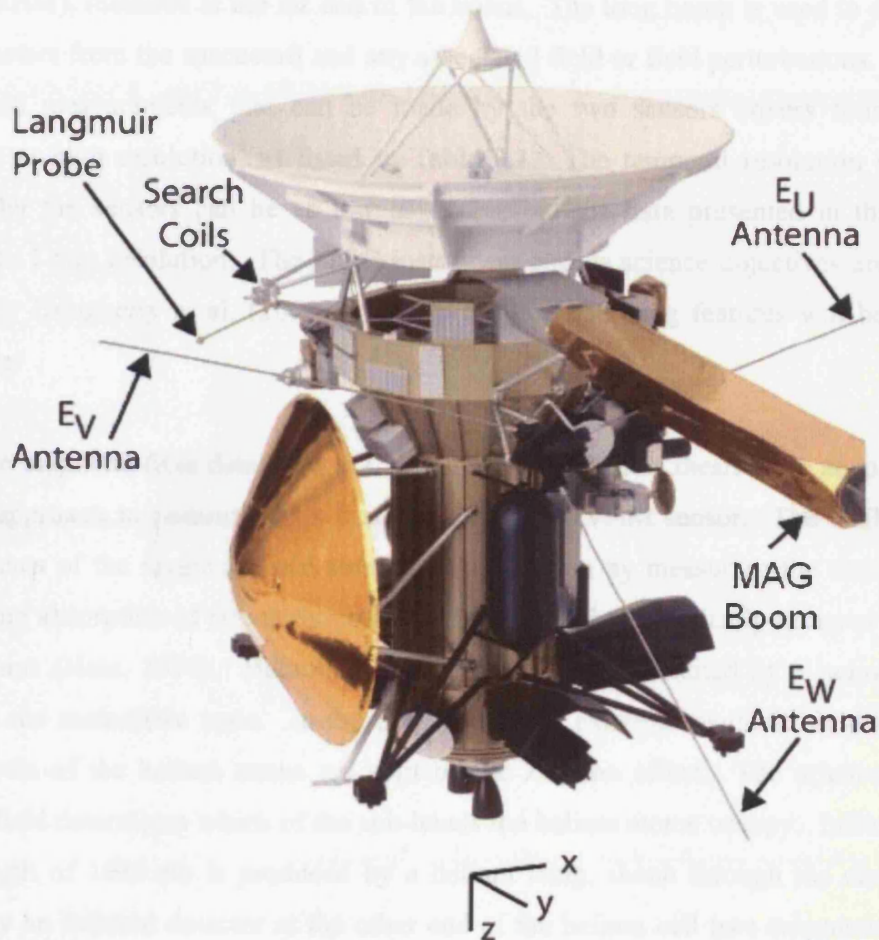


Figure 3.2 Schematic of the Cassini-Huygens spacecraft showing the position of the magnetometer (MAG) boom and the RPWS sensors, including the three electric antennas (E_U , E_V , E_W). Adapted from Gurnett et al. (2004).

3.2.1 *The Cassini magnetometer*

The Cassini magnetometer (MAG) instrument consists of two components: a fluxgate magnetometer (FGM) mounted halfway along the 11 m magnetometer boom partially-visible in Figure 3.2, and a vector helium magnetometer, which is also capable of acting in a scalar mode (V/SHM), mounted at the far end of the boom. The long boom is used to distance the magnetometers from the spacecraft and any associated field or field perturbations. The range of the field measurements that can be made by the two sensors covers four orders of magnitude at high resolution, as listed in Table 3.1. The temporal resolution of the data collected by the sensors can be as low as 1/32 s, but the data presented in this thesis is averaged to 1 min resolution. The MAG instrument and its science objectives are described in detail by Dougherty et al. (2004) and only the key operating features will be described briefly here.

The magnetic field data used in Chapters 4 and 7 of this thesis were acquired during Cassini's approach to Saturn and its first orbit using the VHM sensor. The VHM provides measurements of the magnetic field strength and direction by measuring the external field's effect on the absorption of circularly-polarized infrared light by optically-pumped metastable helium atoms (Ness, 1970). Helium in a glass sensor cell is excited by a radio frequency wave into the metastable state. In the presence of an external magnetic field the excited energy levels of the helium atoms are split by the Zeeman effect. The orientation of the magnetic field determines which of the sub-levels the helium atoms occupy. Infrared light at a wavelength of 1083 nm is produced by a helium lamp, shone through the chamber, and detected by an infrared detector at the other end of the helium cell (see schematic in Figure 3.3). The absorption of the light by the atoms depends on the energy levels they occupy, i.e. the absorption depends on the field. Another field of known strength is applied to the cell with a varying orientation; this is called the sweep field. The sweeping of the field over the chamber causes the He atoms to change between the Zeeman sub-levels, depending on the net applied field (i.e. the combination of the external and sweep fields). The resultant varying intensity pattern of the detected infrared light is analysed by a phase coherent detector. The phase coherent detector isolates the component of the varying intensity signal caused by the external field and drives a set of triaxial coils to generate a feedback field in the cell, which exactly cancels the external field. The external field components can then be found because the currents used to generate the feedback field by the calibrated triaxial coils are known. The

Table 3.1 Dynamic range and resolution of the Cassini magnetometer sensors. From Dougherty et al. (2004).

Sensor	Dynamic range	Resolution
FGM	± 40 nT	4.9 pT
	± 400 nT	48.8 pT
	$\pm 10\,000$ nT	1.2 nT
	$\pm 44\,000$ nT	5.4 nT
VHM	± 32 nT	3.9 pT
	± 256 nT	31.2 pT
SHM	256-16384 nT	36 pT

H_S = SWEEP FIELD

H_A = AMBIENT FIELD

H_R = RESULTANT

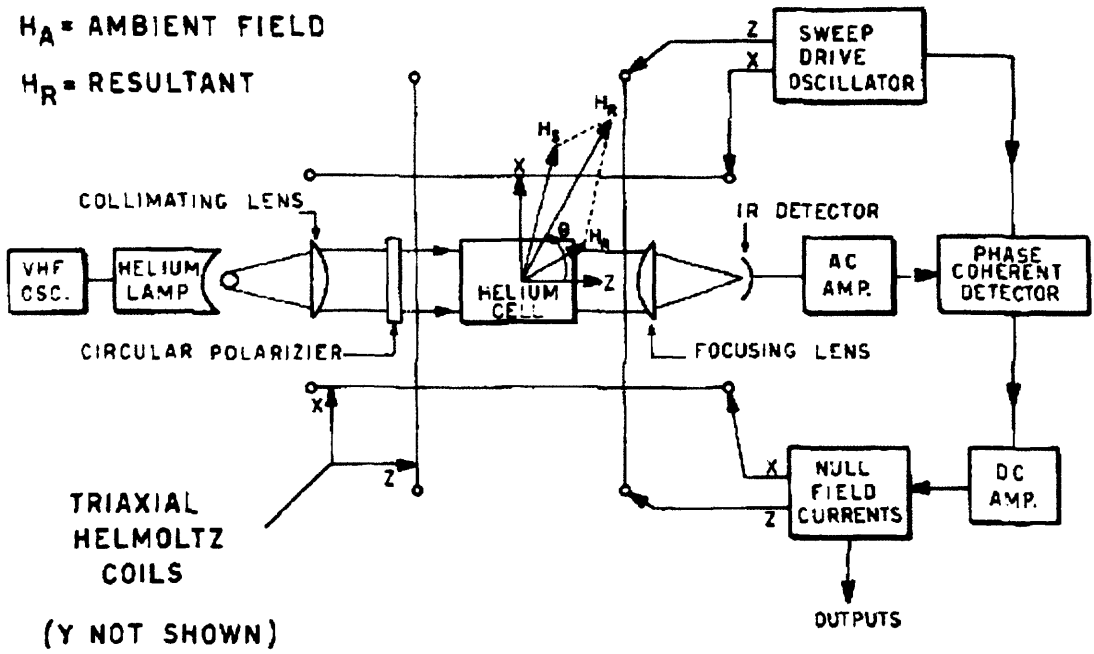


Figure 3.3 Simplified block diagram of a vector helium magnetometer. From Ness (1970).

absorption of the light by the helium atoms is a function of the angle between the field and the optical axis of the cell, so sweeping the applied field through all angles allows the three orthogonal components of the external field to be detected. A full description of the workings of a VHM and other types of magnetometers is given by Ness (1970).

In this thesis only measurements of the magnetic field in the solar wind are used, not measurements from inside the planet's magnetosphere. The field data are therefore presented using the RTN coordinate system, which is a right-handed spherical polar system referenced to the Sun's spin axis, with B_R directed radially outward from the Sun, B_T azimuthal in the direction of solar rotation, and B_N normal to the other two components, that is, positive northwards from the equatorial plane.

3.2.2 *The Cassini Radio and Plasma Wave Science Investigation*

The Cassini Radio and Plasma Wave Science (RPWS) investigation (Gurnett et al. 2004) was designed to study radio emissions, plasma waves, thermal plasma, and dust in the vicinity of Saturn. The instrumentation consists of three nearly orthogonal electric field antennas, three orthogonal magnetic antennas, and a Langmuir probe. The Langmuir probe is a positively-charged spherical sensor in which a current is generated by electrons in the surrounding plasma. The properties of this current and its voltage relation are used to derive the electron density and temperature of the surrounding plasma. The RPWS magnetic antennas are used to detect the magnetic component of electromagnetic waves in the frequency range 1 Hz to 12 kHz. The electric field antennas detect electric fields over a much larger frequency range of 1 Hz to 16 MHz. This range includes the 100-400 kHz frequency band at which Saturn Kilometric Radiation (SKR) emission peaks (see Section 2.5). Having three antennas allows the RPWS to perform both direction finding and polarization measurements. Figure 3.2 shows the positions of the three electric antennas, labelled E_U , E_V , and E_W , on the Cassini spacecraft. Each of these antennas is 10 m long and 2.86 cm in diameter. The E_U and E_V antennas can be used together as a dipole antenna aligned along the x-axis: E_X . A simple block diagram of the RPWS instrument is shown in Figure 3.4 with the electric antennas at the top left.

The signals from the RPWS antennas are processed using various receivers, which are shown in the middle block of Figure 3.4. The high frequency receiver (HFR) provides auto-

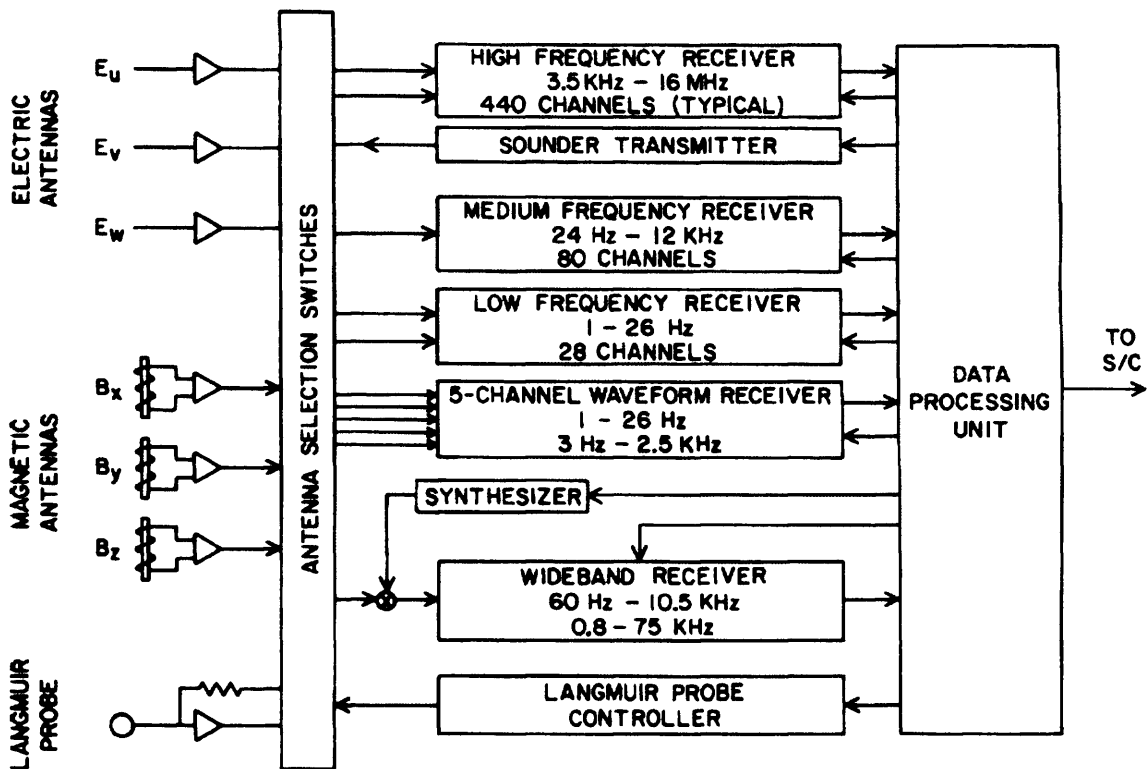


Figure 3.4 Simplified block diagram of the RPWS instrument. From Gurnett et al. (2004).

and cross-correlation intensity measurements from two antennas over the frequency range 3.5 kHz to 16 MHz. The two antennas used are any of the E_X , E_U or E_V , together with the E_W . The medium frequency receiver (MFR) provides intensity measurements over the frequency range 24 Hz to 12 kHz for a single antenna. This receiver usually toggles between the electric dipole E_X and magnetic B_X field sensors. The low frequency receiver (LFR) also usually operates between the E_X and B_X antennas, over a frequency range 1 Hz to 26 Hz. The waveform receiver (WFR) collects waveform measurements from up to 5 inputs simultaneously, e.g. 2 electric and 3 magnetic antennas, over one of two frequency ranges: 1 to 26 Hz, or 3 Hz to 2.5 kHz. The WFR operates for short intervals only whereas the wideband receiver provides near-continuous wideband waveform measurements over either 60 Hz to 10.5 kHz, or 800 Hz to 75 kHz. The receivers perform spectral analysis to provide the intensity in certain frequency bands and at certain resolution, depending on the mode. The data presented in Chapter 7 of this thesis is electric field spectra from the LFR, MFR and HFR, in logarithmically equal frequency bands and at 1 min temporal resolution. The electric field data is also integrated over two different frequency bands (100-300 kHz and 4-1000 kHz) to give the emitted power in each of these bands as a function of time. This data will be discussed further in Chapter 7.

3.3 The Hubble Space Telescope

The Hubble Space Telescope (HST) is a 2.4 m reflecting telescope orbiting the Earth at an altitude of ~600 km. The HST is a coordinated programme between ESA and NASA, designed to provide a long-lasting observing platform beyond the blurring effects of the Earth's atmosphere. HST was deployed in 1990 and has proved extremely successful in contributing to many areas of astronomy. Here, we are interested in the images of Saturn's UV aurora acquired by HST, using the imaging spectrograph described below.

3.3.1 Space Telescope Imaging Spectrograph

A spectrograph is an optical instrument used in separating and recording the spectral components of light or other radiation. The Space Telescope Imaging Spectrograph (STIS) was installed on the HST in 1997. A thorough description of STIS and its capabilities is given by Woodgate et al. (1998), and this section summarises only the features relevant to the data used in this thesis. A simplified schematic showing STIS's optical design is shown in

STIS OPTICAL CONCEPT

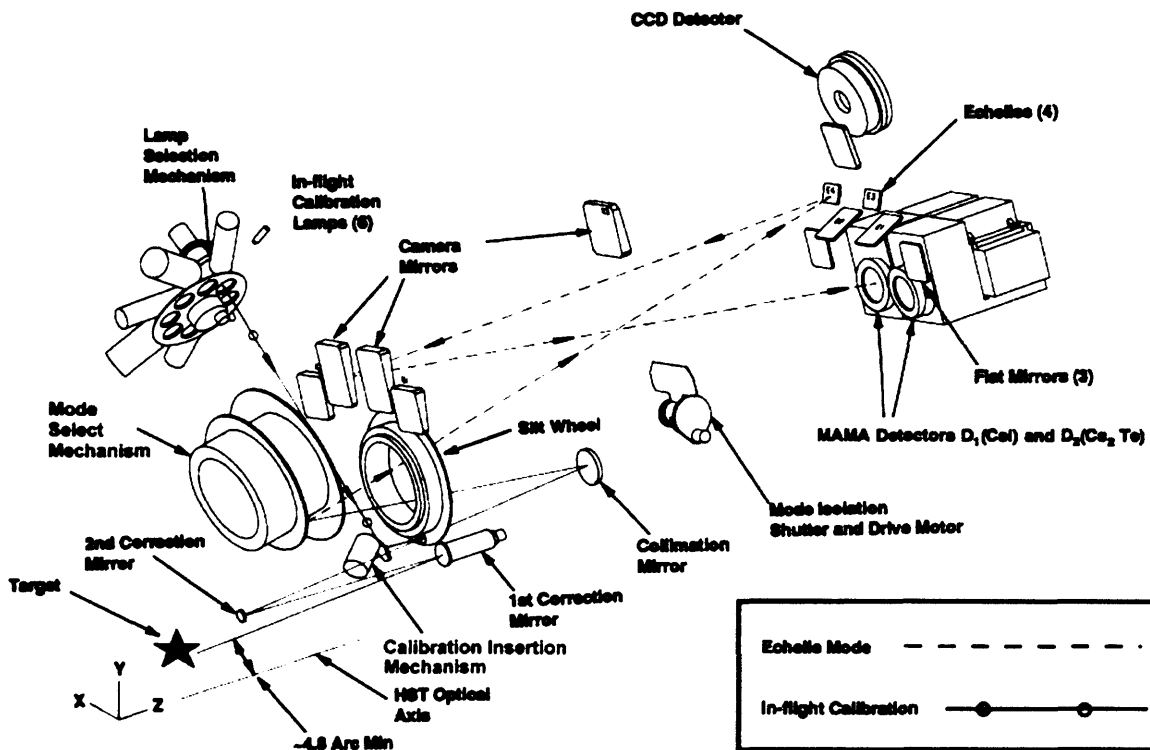


Figure 3.5 Simplified optical layout of STIS. From Woodgate et al. (1998).

Figure 3.5. The light entering the instrument is first corrected for the HST primary mirror aberrations using the two correction mirrors shown in Figure 3.5, then passes through one of the slits in the slit wheel. The choice of slit, which range in size from $50'' \times 50''$ to $0.1'' \times 0''.025$ ($1'' = 1$ arcsecond = $1/3600$ deg), is used to set the field of view. The beam is then collimated by the collimator mirror and reflected back to the Mode Select Mechanism, which determines the rest of the beam path according to the imaging mode and detector required. The Mode Select Mechanism contains the gratings which disperse the light into its spectral components for spectroscopy modes, as well as apertures for the camera modes, which are used to image Saturn's aurora. In the camera mode the beam is directed to a mirror near the detectors then on to the appropriate camera mirror. At the end of the beam path are STIS's three detectors: one Charge Coupled Device (CCD) and two Multianode Microchannel Arrays (MAMA), which between them cover a wavelength range of 115-1000 nm (ultraviolet and visible bands). Saturn's auroral emissions peak in the UV at 121 nm (the hydrogen Lyman- α line), within the 115-170 nm wavelength range of the FUV MAMA detector (D_1 in Figure 3.5). This detector is a solar blind (i.e. not sensitive to visible wavelengths) photon-counting detector. Photons entering the detector are incident on the CsI photocathode, producing electrons. The electrons are accelerated into a curved microchannel plate producing a cloud of secondary electrons. The charge is detected by an anode array then amplified and decoded to give the position and time of arrival of the charge pulse. The detector records this data to build up a 2-dimensional image across the telescope field of view.

Some auroral images are obtained using an SrF₂ filter, held in the slit wheel shown in Figure 3.5. This filter rejects wavelengths below 125 nm, including the strong H Lyman- α line, so it is used when the HST is in sunlight to remove any potential geocoronal contamination. The MAMA has an array size of 1024 x 1024 pixels, where the pixel size is 0.0243". The point spread function (PSF), which defines the spread due to diffraction of an ideal point source when observed by the telescope optics, is 0.08" full width at half maximum. The limitations imposed by the PSF on determining the position and width of Saturn's aurora will be discussed in Chapter 5.

Chapter 4

Open flux estimates in Saturn's magnetosphere during the January 2004 Cassini-HST campaign, and implications for magnetospheric dynamics

4.1 Introduction

In January 2004 an unprecedented sequence of UV images of Saturn's southern aurora was obtained by the HST over a three week interval (Clarke et al., 2005; Grodent et al., 2005), in coordination with observations of the interplanetary medium upstream from Saturn by the Cassini spacecraft en route to orbit insertion at the planet (Crary et al., 2005; Bunce et al., 2006). These images record a substantial variability in the auroral emissions over the interval, in line with the discussion of solar wind-controlled aurorae given in Chapter 2, responding strongly to recurrent corotating interaction region (CIR) compressions in the heliosphere. Cowley et al. (2005a) proposed that the auroral responses (brightening and expansion of emission) are formed by bursts of tail reconnection excited by the sudden magnetospheric compression produced by the arrival of the leading ('forward') shock of the CIR compression region. The exact physics leading to the onset or enhancement of tail reconnection under these circumstances has not yet been determined in detail. We note, however, that compression of the magnetosphere will both reduce the thickness of the plasma sheet while simultaneously increasing the cross-tail current it has to carry (through the increased field strength in the tail lobes). Both effects require an increase in the plasma sheet current density, which may lead to instability. Formally, compression of the magnetosphere is related to the combined action of the dynamic, thermal, and magnetic pressures of the solar wind plasma. However, for a highly super-magnetosonic flow such as the solar wind, the dynamic pressure is by far the dominant component, such that we suppose the above auroral effects relate principally to this parameter. While the dynamic pressure is then a key parameter in Saturn's magnetospheric dynamics, we also point out that due to the frozen-in nature of the flow, the magnetic field strength forms a rough but useful proxy, as is demonstrated in the Cassini data presented below.

Based on the discussion of auroral generation mechanisms in Chapter 2, it seems reasonable to suppose that the poleward boundary of Saturn’s UV aurorae observed by the HST lies close to the boundary between open and closed field lines, and expands and contracts with episodes of magnetopause and tail reconnection. This assumption will be taken as the working hypothesis in this chapter. In this case, then, we can use the HST images obtained in January 2004 to estimate the variations in open flux present in Saturn’s magnetosphere over that interval. The overall change in open flux that occurs during an interval is given by the difference in the amount of open flux that is created at the magnetopause, and that which is destroyed by reconnection in the tail. In a recent paper, Jackman et al. (2004) have proposed a formula for the magnetopause reconnection rate at Saturn in terms of the upstream interplanetary field and plasma parameters, based on empirical data obtained at Earth. If we then employ this formula to estimate the open flux produced during an interval, we can also infer from the overall open flux change the amount of open flux that has been closed during the interval, and hence the averaged tail reconnection rate. In this chapter open flux estimates derived from HST images are combined with concurrent estimates of open flux production determined from Cassini measurements of upstream interplanetary parameters, to discuss magnetopause and tail reconnection rates and overall magnetospheric dynamics at Saturn during the January 2004 Cassini-HST campaign. We also discuss our conclusions in relation to the nature of the auroral forms which were observed. The next section begins by providing a brief overview of the Cassini-HST campaign data, together with a discussion showing how the open flux estimates were obtained from the images.

4.2 Cassini Observations, HST Images, and Open Flux Estimates

4.2.1 Overview of the January 2004 HST-Cassini Campaign Data

The structure of the interplanetary medium in the vicinity of Saturn’s orbit during Cassini’s approach to the planet, encompassing the interval of interest here, has been discussed by Jackman et al. (2004). Using interplanetary magnetic field (IMF) data obtained by Cassini over a 6.5-month interval encompassing eight solar rotations at the spacecraft, they showed that the structure of the heliosphere was consistent with a tilted solar dipole field, as expected for the declining phase of the solar cycle. Specifically, the IMF consisted of two sectors per solar rotation, with heliospheric current sheet (HCS) crossings embedded within few-day

high-field regions associated with corotating interaction region (CIR) compressions, separated by several-day low-field regions associated with solar wind rarefactions. This structuring is evident in the IMF and solar wind data obtained by Cassini during the January 2004 HST imaging campaign, presented here in Figure 4.1 for the interval days 1-31 of 2004 (Crary et al., 2005; Bunce et al., 2006). The first three panels of the figure show the IMF components in RTN coordinates, while the fourth panel shows the total field strength. The next three panels display the solar wind velocity (v_{SW}), density (n), and dynamic pressure (P_{SW}), respectively, where the dynamic pressure is calculated from

$$P_{SW} = 1.92 \times 10^{-6} \times n (\text{cm}^{-3}) v_{SW} (\text{km s}^{-1})^2 \text{ nPa} , \quad (4.1)$$

assuming that the solar wind is composed of protons and alpha particles in the ratio 19:1. The final panel shows the magnetopause reconnection voltage (open flux production rate) estimated using the algorithm of Jackman et al. (2004), which will be discussed in section 4.3.2 below.

Although plasma data is not available at the beginning of the interval shown in Figure 4.1, it is evident from the field magnitude data that the interval began with a ‘major’ CIR-related compression region during days 1-6, with field magnitudes typically $\sim 1\text{-}2$ nT. Following this, a rarefaction region of very weak fields, ~ 0.1 nT or less, was observed, associated with slowly falling solar wind speeds and densities $\sim 0.01 \text{ cm}^{-3}$ or less. This interval was ended by the arrival of a ‘minor’ CIR compression on day 15, within which a HCS crossing was embedded, as indicated by the B_T polarity reversal from negative to positive. Within the compression the field strength increased to $\sim 0.2\text{-}0.5$ nT, while the solar wind speed increased to $\sim 530 \text{ km s}^{-1}$ and the density to $\sim 0.1 \text{ cm}^{-3}$. Following this compression, a rarefaction region of intermediate characteristics was then observed during days 19-25, with IMF strengths typically ~ 0.3 nT, and solar wind densities in the range $\sim 0.01\text{-}0.04 \text{ cm}^{-3}$. A third compression then began at the spacecraft on day 25, corresponding to the re-appearance of the ‘major’ compression observed at the beginning of the interval after one solar rotation. A traversal of the HCS from B_T positive to negative occurred on day 26. This compression lasted until almost the end of the interval considered here, characterised by IMF strengths $\sim 1\text{-}2$ nT, increased solar wind speeds up to 630 km s^{-1} , and densities $\sim 0.03\text{-}0.1 \text{ cm}^{-3}$. Here we note that it is evident from the restricted interval when both plasma and field magnitude data are available, that the time-dependent behaviour of the

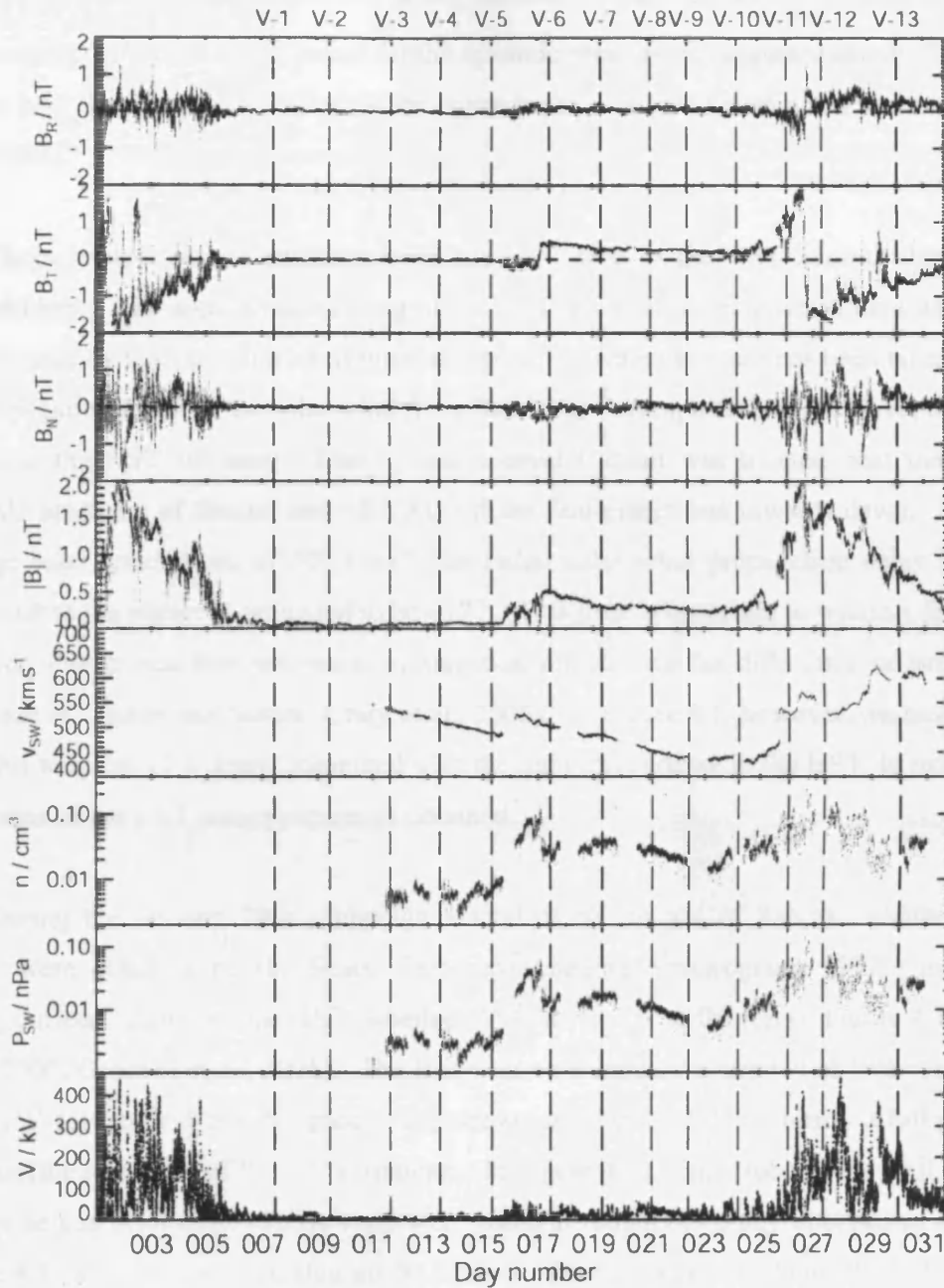


Figure 4.1. Upstream interplanetary conditions for the interval 1-31 January 2004 as measured by the Cassini spacecraft. The first four panels present the IMF components in RTN co-ordinates and the field magnitude. The next three panels show the solar wind velocity, density, and dynamic pressure. The final panel shows the dayside reconnection voltage estimated using the Jackman et al. (2004) empirical algorithm (with $L_0 = 10 R_S$) based on observations at Earth, as described in the text. The vertical long-dashed lines indicate the start times of the 13 visits during which the HST imaged Saturn's UV aurorae. These times have been shifted by an estimated 17 h solar wind propagation delay from Cassini to the planet, plus 68 min that the image photons took to reach HST from Saturn.

field magnitude forms a rough proxy for the dynamic pressure as suggested above. Therefore we can infer the nature and timings of structures in the solar wind even when plasma data are unavailable.

These interplanetary conditions form the back-drop to the HST auroral observations analysed here. The approximate timing of the HST observations relative to the Cassini data are indicated by the vertical dashed lines in Figure 4.1, where account has been taken both of the propagation delay of the solar wind from Cassini to Saturn, and the light travel time from Saturn to the HST (68 min). During this interval Cassini was located near the ecliptic ~ 0.2 AU upstream of Saturn, and ~ 0.5 AU off the Sun-planet line towards dawn. Using an average solar wind speed of 500 km s^{-1} , the radial solar wind propagation delay from the spacecraft to the planet is estimated to be ~ 17 h. This time is uncertain to within a few hours, however, due to possible non-radial propagation effects and the difference in heliocentric longitude of Cassini and Saturn (Crary et al., 2005). In Figure 4.1, however, we have simply used this nominal 17 h delay, combined with the light travel delay to the HST, to indicate the start times of the HST image sequences obtained.

During the January 2004 campaign a total of 68 images of Saturn’s southern polar aurora were obtained by the Space Telescope Imaging Spectrograph (STIS) instrument during thirteen ‘visits’ by the HST, labelled ‘V-1’ to ‘V-13’ at the top of Figure 4.1 (Clarke et al., 2005; Grodent et al., 2005). The first visit on 8 January consisted of five consecutive orbits (‘V-1.1’ to ‘V-1.5’), designed to capture auroral variations over nearly a full planetary rotation (the start time of ‘V-1.1’ is indicated in Figure 4.1). Each subsequent visit obtained images on one orbit only. These visits were made at roughly two-day intervals as shown in Figure 4.1, with the last occurring on 30 January. During each orbit four UV (115-174 nm) images were obtained, the first using a SrF_2 filter to remove the Lyman- α line and potential geocoronal contamination (exposure time 640–740 s), followed by two unfiltered ‘Clear’ images with 270 s exposure times, and then a final filtered image. Here we have combined together the data from the two consecutive ‘Clear’ images on each orbit in order to increase the signal-to-noise ratio, and have then projected them onto a planetary latitude-local time grid in the manner discussed by Gérard et al. (2004) and Grodent et al. (2005). The images view essentially the whole of the southern polar region, which was tilted significantly towards the Earth (and Sun) during the interval. A selection of the projected images is presented in Figure 4.2, illustrating the range of auroral behaviour observed. The data are

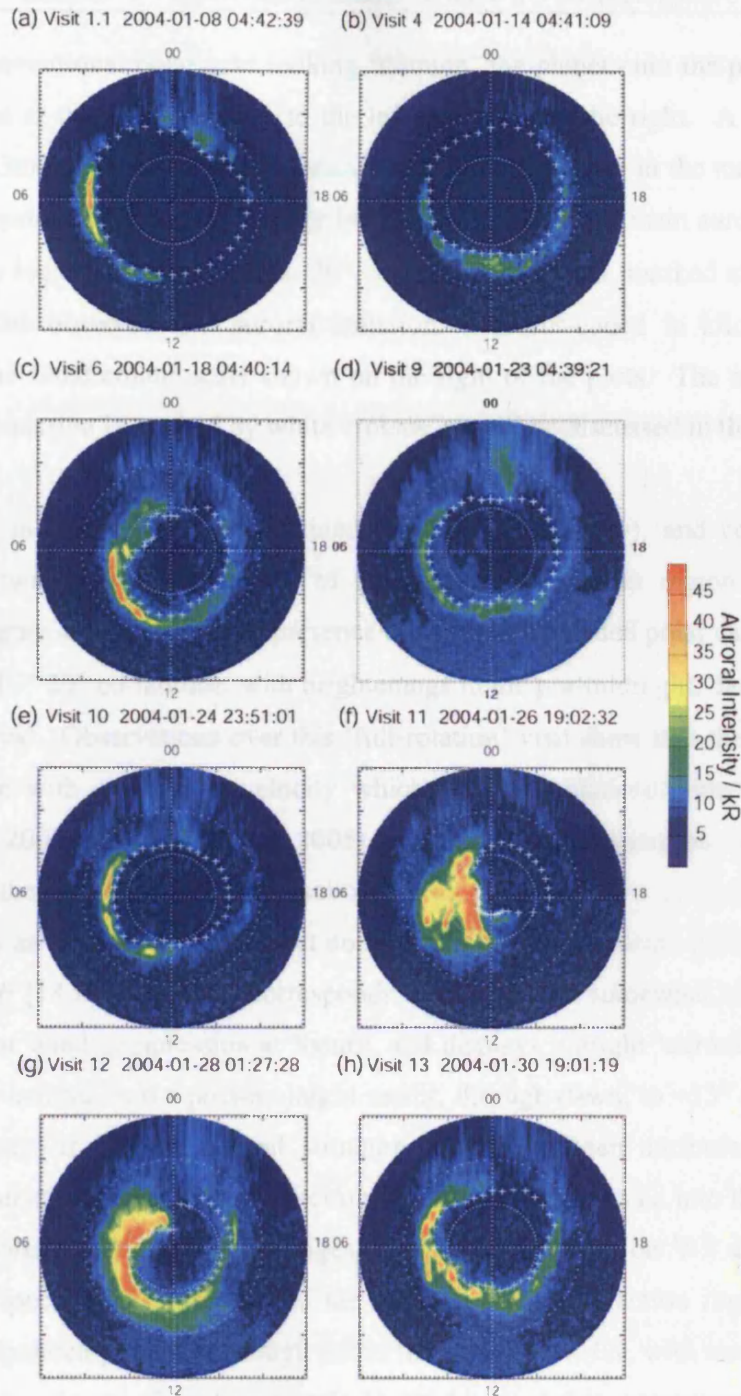


Figure 4.2. Selection of UV images of Saturn's southern aurora taken during January 2004, with the visit number, date, and start time of each image shown at the top of each plot. The images are projected onto a polar grid, from the pole to 30° co-latitude, viewed as though looking 'through' the planet onto the southern pole. Noon is at the bottom of each plot, and dawn to the left, as indicated. The UV auroral intensity is plotted according to the colour scale shown on the right-hand side of the figure. The white crosses mark the poleward edge of the observed auroral features as discussed in the text. The intensities shown are the average of the two unfiltered images obtained over each HST orbit.

shown on a conventional polar grid looking ‘through’ the planet onto the pole at the centre, with local noon at the bottom, dawn to the left, and dusk to the right. A sensitivity study performed by Grodent et al. (2005) has shown that the uncertainty in the mapping procedure is $\sim 1^\circ$ at the dayside but increases, mainly in latitude, to $\sim 2^\circ$ in the main auroral region on the nightside. The region from the pole to 30° co-latitude is shown, marked at intervals of 10° co-latitude. The observed UV auroral emission is colour-coded in kilo-Rayleighs (kR) according to the fixed colour scale shown on the right of the plots. The inferred poleward border of this emission is marked by white crosses, as will be discussed in the next section.

Image (a) in Figure 4.2 was obtained on V-1.1 (8 January), and corresponds to an interval about two days after the end of the major compression region observed at the beginning of Figure 4.1. It shows the presence of a highly expanded polar cap bounded by the auroral oval at 15° - 20° co-latitude, with brightenings in the pre-midnight, dawn, and pre-noon sectors of the oval. Observations over this ‘full-rotation’ visit show that these features rotate around the pole with an angular velocity which is sub-corotational relative to the planet (Clarke et al., 2005; Grodent et al., 2005). Image (b) obtained on V-4 (14 January) corresponds to the first (low-field) rarefaction region, and displays a dimmer oval at 12° - 18° co-latitude with an auroral brightening at noon, encircling a contracted polar cap. Image (c) obtained on V-6 (18 January) then corresponds to the interval somewhat after the arrival of the ‘minor’ solar wind compression at Saturn, and displays a bright ‘auroral spiral’, running from $\sim 5^\circ$ - 8° co-latitude in the post-midnight sector, through dawn, to $\sim 13^\circ$ co-latitude in the post-noon sector. It is such auroral structures that have been attributed by Cowley et al. (2005a) to bursts of nightside reconnection which inject hot plasma into the sub-corotating outer magnetosphere. The next two images, (d) and (e) obtained on V-9 and V-10 (23 and 24 January), respectively, correspond to the ‘intermediate’ rarefaction region, and show a somewhat re-expanded polar cap, though not to the extent of V-1.1, with auroral brightenings at dawn and noon. Image (f) obtained on V-11 (26 January) then corresponds to the onset of the ‘major’ compression region, and shows a highly brightened oval surrounding a contracted polar cap, with the dawn-side almost completely ‘filled-in’ with bright auroral forms, from $\sim 3^\circ$ to $\sim 15^\circ$ co-latitude. About 30 h later, image (g) obtained on V-12 (28 January) shows that the aurorae are still bright, and have rotated into a spiral shape similar to that observed on V-6. The final image (h) obtained during V-13 (30 January), corresponds to near the end of the ‘major’ compression region, just over 4 days after its onset. Bright aurorae are still

observed, particularly on the dawnside, and the polar cap boundary has expanded somewhat to larger co-latitudes, e.g. 12° - 15° co-latitude in the pre-dawn region.

4.2.2 Determination of the Auroral Boundary and Open Flux Estimates

The selection of images in Figure 4.2 clearly demonstrates that the size of Saturn’s auroral oval changes markedly during the Cassini-HST campaign, in response to changes in the interplanetary medium shown in Figure 4.1. If the central dark polar cap region bounded by the aurora is taken to represent the open magnetic flux region mapping to the tail lobes of the magnetosphere, on the basis of the discussion in Chapter 2 and the introduction above, we can then use the images to estimate the open flux present during each HST visit, and examine how it changes with time. In this section we discuss the basis on which the open flux estimates have been made.

The latitudinal positions of the inferred boundary between open and closed field lines, marked by the white crosses in Figure 4.2, have been determined by eye by looking for a sharp increase in the emission intensity between the polar region and the auroral zone. No specific ‘cut-off’ intensity has been used to determine the ‘edge’, since the intensity varies markedly around the boundary and between images. An example is given in Figure 4.3, where we show the intensity profiles versus co-latitude for 00, 06, 12, and 18 MLT for V-13, together with the inferred positions of the boundary, marked by vertical dashed lines. These are chosen to the nearest 1° , consistent with the resolution determined by the method of image projection over most of the image. For each image these positions have been determined every 10° in longitude from 0° to 350° . In regions of low intensity ‘noisy’ data, the boundary positions at adjacent longitudes have also been taken into account, so as to produce a boundary which is reasonably ‘smooth’, rather than following the detailed variations of the ‘noise’, which is due mainly to fluctuations in the background emission of reflected solar photons. In addition, in some local time sectors, e.g. 12-18 MLT in Figure 4.2a (corresponding to V-1.1), there are no auroral features distinguishable from the background emission. In these situations the location of the boundary is estimated by eye, using simple extrapolation between the end points where the aurorae are visible, to continue a reasonable oval shape. These procedures have been applied to each of the 17 combined ‘clear’ images obtained during the HST-Cassini campaign, with results that can be judged from the examples provided in Figure 4.2.

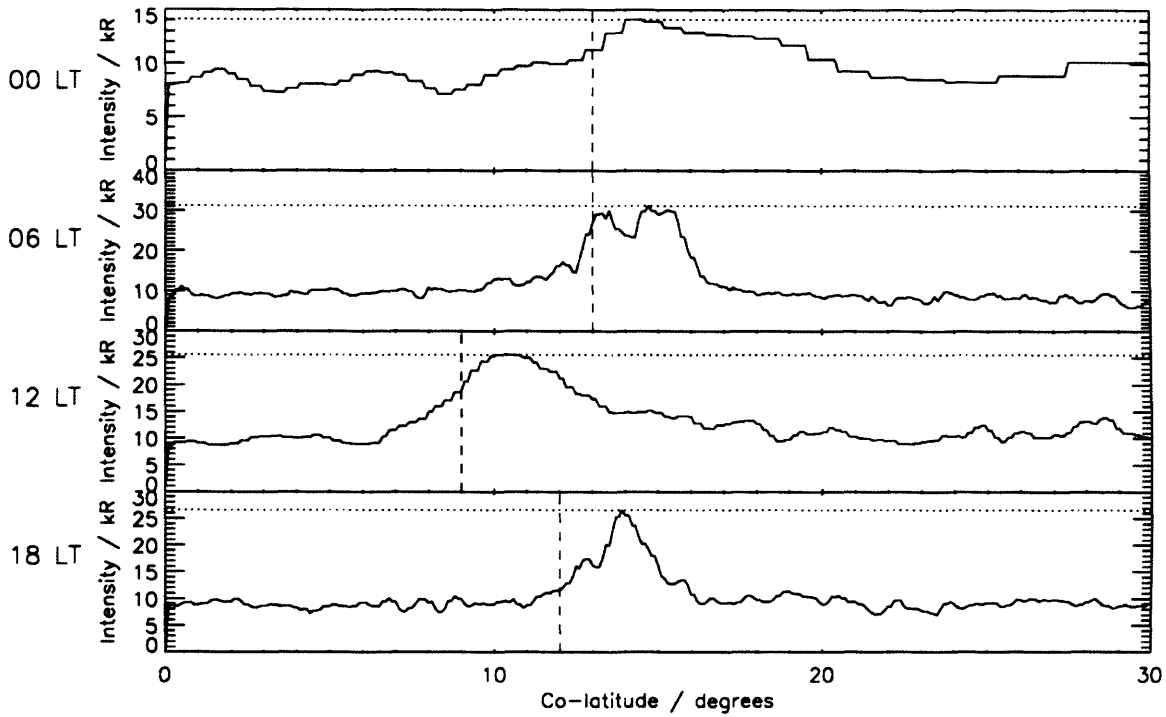


Figure 4.3. The intensity profile (kR) for co-latitudes 0° – 30° along meridians at 0, 06, 12, and 18 MLT for visit V-13 (see Figure 4.2). The vertical dashed lines mark the sharp increase in auroral intensity (to the nearest 1° of co-latitude), that we have taken to indicate the poleward edge of the auroral features at each local time.

Having estimated the position of the poleward boundary of the aurora as described above, we can then determine the amount of magnetic flux contained within it, taking this to be an estimate of the amount of open flux in the system according to the previous discussion. We note here, however, that it is possible that UV aurorae may also occur on open flux tubes near the dayside boundary, specifically associated with localised field-aligned currents flowing in the vicinity of the dayside cusp mapping to the magnetopause reconnection sites (Bunce et al., 2005a; Gérard et al., 2005). Analysis by Gérard et al. (2005), for example, suggests that lobe reconnection occurring under southward IMF conditions may be the origin of a bright UV feature observed poleward of the main oval near noon in the image obtained during V-8 (not shown), corresponding to the ‘intermediate’ rarefaction region. If this is the case, the noon auroral ‘bulge’ in this image then maps to open field lines just inside the boundary, such that our procedure underestimates the amount of open flux present. Here, however, we have not attempted to take account of such features, which in the present state of understanding would require individual interpretations to be made from image to image. Instead we have maintained a consistent method, as above, within the whole sequence of images. While some uncertainty is thereby introduced, we point out that the areas of the polar cap involved, and the fluxes they contain, are small compared with the overall values. The flux within the noon ‘bulge’ in V-8, for example, corresponds to only ~10% of the total open flux calculated by our procedure. Positional uncertainties introduced by the method of projection also generate a maximum error of $\pm 10\%$ in the open flux values calculated. Uncertainties at this level will not greatly affect the conclusions reached here.

To obtain the amount of open flux contained within the auroral boundary we need to employ a model of Saturn’s internal magnetic field. That employed here is the Saturn-Pioneer-Voyager (SPV) model of Davis and Smith (1990), determined from the near-planet Pioneer-11, and Voyager-1 and -2 magnetic data. This model is symmetric about the spin axis of the planet, and consists of aligned dipole, quadrupole, and octupole components. The field can be described by a flux function $F(r, \theta)$, related to the field components by $\mathbf{B} = (1/r \sin \theta) \nabla F \times \hat{\boldsymbol{\phi}}$, such that F is constant on a field line. Here we employ spherical polar co-ordinates, with r the distance from the centre of the planet, θ the co-latitude angle measured from the north pole, and φ the azimuthal angle. For the above field the flux function is (e.g. Cowley and Bunce, 2003c)

$$F(r, \theta) = R_S^2 \sin^2 \theta \left[g_1^0 \left(\frac{R_S}{r} \right) + \frac{3}{2} g_2^0 \cos \theta \left(\frac{R_S}{r} \right)^2 + \frac{1}{2} g_3^0 (5 \cos^2 \theta - 1) \left(\frac{R_S}{r} \right)^3 \right], \quad (4.2)$$

where for the SPV model we have $g_1^0 = 21160$, $g_2^0 = 1560$, and $g_3^0 = 2320$ nT for a conventional Saturn radius of $R_S = 60330$ km. Note that the arbitrary constant in the flux function has been chosen such that $F = 0$ at the poles. It is then readily shown that the amount of magnetic flux threading any surface bounded by a ring of radius $r \sin \theta$ at co-latitude θ is $\Phi = 2\pi F(r, \theta)$. Consequently, if we divide up the area inside the auroral boundary into 36 longitudinal sectors, each $\Delta\varphi = \pi/18$ radians (i.e. 10°) wide, centred on the longitudes of the white crosses in Figure 4.2, then the amount of magnetic flux contained is

$$\Phi = \Delta\varphi \sum_{n=1}^{36} F(R(\theta_n), \theta_n), \quad (4.3)$$

where θ_n is the co-latitude of the boundary in longitude sector n , and $R(\theta_n)$ is the radius of the surface containing the auroral emissions at that co-latitude, onto which the HST data have been projected in Figure 4.2. This surface is assumed to be an ellipsoid of revolution about the spin axis, with an equatorial radius R_e and a polar radius R_p , i.e.

$$R(\theta) = \frac{R_e}{(1 + \varepsilon \cos^2 \theta)^{1/2}} \quad \text{where} \quad \varepsilon = \left(\frac{R_e}{R_p} \right)^2 - 1. \quad (4.4)$$

The surface containing the peak auroral emissions lies 1000 km above the 1 bar reference spheroid of the planet for the unfiltered images, such that $R_e = 61268$ km $\approx 1.02 R_S$, $R_p = 55364$ km $\approx 0.92 R_S$, and $\varepsilon \approx 0.22$ (Trauger et al., 1998; Grodent et al., 2005).

4.3 Magnetospheric Dynamics During the January 2004 Cassini-HST Campaign

Using the algorithm defined by equations (4.2) to (4.4), we can compute the amount of flux contained within the auroral boundary, representing our estimate of the open flux in Saturn’s magnetosphere, for each of the HST images. In this section we now present our results for the

interval, and discuss how the changing amount of open flux relates to concurrent interplanetary conditions.

4.3.1. Variation of the Open Flux

In Figure 4.4 the open flux estimates obtained for each of the combined ‘Clear’ images are shown in the bottom panel by the crosses joined by solid lines, plotted versus time. The times shown are the start times of the intervals in which the observed aurora actually occurred at Saturn, i.e. the HST time minus 68 min. The stars and dashed lines in this panel show the corresponding values of the power in UV auroral emissions from H₂ and H, extrapolated from the STIS bandpass over the range covering the H₂ Lyman and Werner bands using a synthetic emission spectrum (Clarke et al., 2005; Grodent et al., 2005). The uncertainties in these values are estimated to be about $\pm 15\%$. The relationship to the interplanetary data is indicated in the top two panels, where we show the solar wind dynamic pressure and IMF magnitude, respectively. These data have been shifted forward in time by the estimated 17-h propagation delay to match the image times, such that the relative timing of the HST and Cassini data remains identical to Figure 4.1 (which focused on Cassini data and hence employed Cassini measurement times). The two vertical dashed lines in the plot show the (shifted) times of the forward shocks which initiated the minor (S1) and major (S2) CIR-related compressions, indicated by the sudden increases in field strength. The shifted times of arrival at Saturn occurred on days 16 and 26 respectively. The tail-end of the previous ‘major’ compression region starting on day 1, prior to the HST imaging interval, can also be seen at the beginning of the plot.

The sequence of images begins with the most expanded auroral oval observed during the interval, this being the image from V-1.1 shown in Figure 4.2a. The open flux contained within the oval in this case is estimated to be 49 GWb. Over the five orbits of V-1, corresponding to an interval of ~ 7 h on day 8, Grodent et al. (2005) show that the auroral morphology changed significantly, associated with sub-corotation of major auroral features at $\sim 65\%$ of the planetary rotation rate. The overall auroral power also varied significantly, between ~ 5 and ~ 10 GW, as can be seen in Figure 4.4. Nevertheless, the open flux deduced from the five independent images varies by only $\sim 5\%$, between ~ 47 and ~ 49 GWb, indicating that our method is reasonably robust, and does not lead to major scatter in the open flux values. This near-constant flux result is also consistent with modest reconnection rates

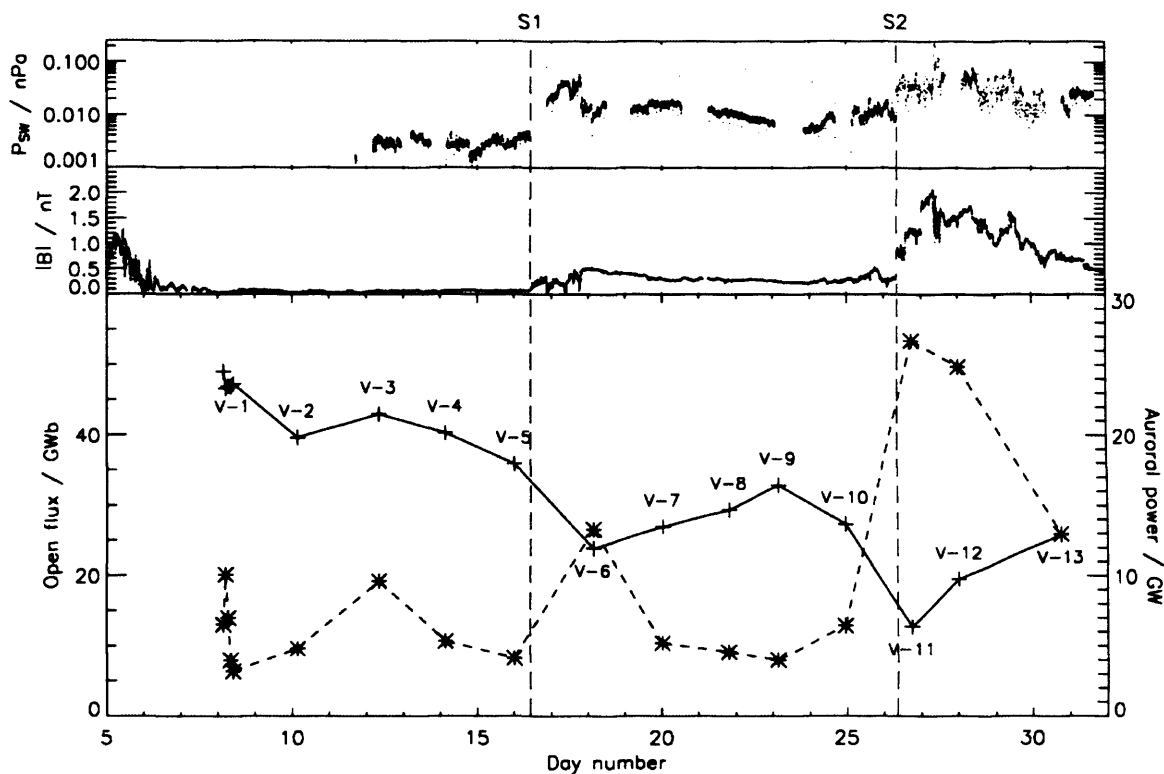


Figure 4.4. The open flux content of the southern polar cap estimated from the HST images is plotted versus time in the bottom panel, shown by the crosses marked at each HST visit (V-1 to V-13) and joined by the solid line. The times marked are the actual times the aurora occurred at Saturn, i.e. the HST time minus 68 min. Also shown by the stars and dashed line are the values of the power in UV auroral emissions from H_2 and H at each visit (using the right-hand scale), extrapolated from the STIS bandpass over a wavelength range covering the H_2 Lyman and Werner bands using a synthetic emission spectrum. The top and middle panels show the solar wind dynamic pressure and interplanetary magnetic field strength, respectively, measured by the Cassini spacecraft for 1-31 January 2004 and shifted forward by the 17 h propagation delay to match the times the aurora occurred. The vertical dashed lines mark the estimated arrival times of two solar wind shocks marking the start of CIR-related compressions.

occurring during the interval, as might be expected from the rarefaction region conditions then prevailing. However, to produce a clearly observable effect over this short interval, say a change in open flux of more than ~ 5 GWb in either direction, the average net reconnection rate would have to exceed ~ 200 kV.

Two days later, however, on day 10, the open flux estimated from the V-2 image is clearly smaller at ~ 40 GWb, the value then remaining relatively steady for V-3 and V-4 (Figure 4.2b), varying by only ~ 3 GWb. Following this on day 16, the V-5 image indicates that the open flux content had decreased further to 36 GWb. All these images were obtained during the initial low-field solar wind rarefaction interval, during which magnetopause reconnection rates are predicted to be very low (Jackman et al., 2004, Bunce et al., 2006). These results indicate the occurrence of an interval of variable net open flux closure within Saturn’s magnetosphere associated with tail reconnection, as will be quantified in the following section. Visit V-5 occurred a few hours before the arrival at the planet of the forward shock (S1) of the minor compression region. The effects of this are seen prominently in the next measurement on V-6 (Figure 4.2c), which occurred ~ 1.5 days after the projected arrival of the compression. From the V-6 image we deduce an open flux of ~ 24 GWb, suggesting that ~ 12 GWb of flux was closed in the 2 days between V-5 and V-6. There is also a significant increase in the auroral power recorded at V-6, rising from a value of a few GW to ~ 13 GW. Cowley et al. (2005a) have suggested that such events are associated with compression-induced intervals of major open flux closure in Saturn’s magnetic tail.

Visits V-7 to V-10 (Figures 4.2d and 4.2e) then occurred during the solar wind rarefaction region of intermediate field strength on days 20-24. The first three of these images indicate a steady increase in the size of the auroral oval, with the open flux rising to ~ 33 GWb at V-9. This indicates the occurrence of an interval of net accumulation of open flux in the tail due to magnetopause reconnection. On V-10 (Figure 4.2e), however, the open flux content reduced again to ~ 27 GWb, indicating the excitation of tail reconnection. The auroral power correspondingly showed a small increase from 4-5 GW during V-7 to V-9, up to ~ 6.5 GW during V-10. The major solar wind compression initiated by shock S2 then arrived at Saturn during day 26, associated with substantial effects ~ 9 h later in the image obtained on V-11 (Figure 4.2f). This displays the smallest polar cap observed in this sequence, containing only ~ 13 GWb of open flux, together with the highest auroral power observed of ~ 27 GW. The net flux closure between V-10 and V-11 is estimated to be

~15 GWb. During the final two visits, V-12 and V-13 (Figures 4.2g and 4.2h), the open flux then increased again while the auroral power declined, this indicating an interval of net open flux production in the presence of enhanced compression-region interplanetary field strengths. The final open flux estimate obtained on V-13 was ~26 GWb, with an auroral power of ~13 GW. We note that as a whole, the interval shown in Figure 4.4 is associated with falling values of the open flux, the initial value being almost twice as large as the final. Given the recurrent nature of interplanetary conditions over each ~25 day solar rotation during this period (Jackman et al., 2004), however, we may expect that the condition of Saturn’s magnetosphere should also be approximately cyclical over a complete solar rotation. Therefore we anticipate that had observations been made in the interval following V-13, the open flux content would have increased back towards values seen during V-1 (i.e. to ~45–50 GWb), the latter being observed ~2 days after the end of the preceding major solar wind compression which occurred one solar rotation earlier.

To summarise these observations, significant decreases in the open flux were observed following major compressions of the magnetosphere by the solar wind between V-5 and V-6, and V-10 and V-11, by ~12 and ~15 GWb respectively. These intervals are inferred to be associated with rapid net closure of open flux in the magnetospheric tail produced by solar wind compressions of Saturn’s magnetosphere, in agreement with the previous discussions of Jackman et al. (2004) and Cowley et al. (2005a). After these decreases, the open flux then increased again over several days due to net open flux production in the relatively high-field strength intervals that followed. Decreases in open flux were also observed during the first low-field solar wind rarefaction region interval, with an overall reduction of ~13 GWb between V-1 and V-5, and at the end of the intermediate rarefaction region, where a reduction of ~6 GWb occurred between V-9 and V-10. These observations are suggestive of the occurrence of intermittent intervals of more modest net tail reconnection, as discussed by Grodent et al. (2005) and Bunce et al. (2006). We also observe in Figure 4.4 a general anti-correlation between the amount of open flux contained in the polar cap (i.e. the size of the auroral oval) and the auroral power, in agreement with the results presented previously by Clarke et al. (2005). This suggests a relationship between auroral luminosity and intervals of tail reconnection and open flux closure, similar to that observed at Earth (e.g., Milan et al., 2006).

4.3.2 Magnetopause and Tail Reconnection Rate Estimates

The variations in open flux shown in Figure 4.4 provide a measure of the difference between the rates at which open flux is produced at Saturn’s magnetopause and destroyed in the tail. This is an application of Faraday’s Law, which can be expressed (e.g. Siscoe and Huang, 1985; Cowley and Lockwood, 1992) as

$$\frac{d\Phi}{dt} = V_{MP} - V_{tail} . \quad (4.5)$$

Following Eq. (4.5), in the absence of tail reconnection the amount of open flux contained in the polar cap Φ increases at a rate equal to V_{MP} . Similarly, in the absence of magnetopause reconnection the open flux is destroyed and the polar cap contracts at a rate equal to V_{tail} . If we can make a quantitative estimate of the rate of open flux production at the magnetopause from the upstream solar wind conditions we can compare this to the open flux estimates made above and hence also estimate average tail reconnection rates. This then enables discussion of the overall open flux throughput in the system during the interval of HST observations.

Given the current level of understanding of the reconnection process it is not possible to calculate the reconnection rate ab initio. Instead, studies at the Earth have developed empirical formulae based on simple theoretical ideas, which are fitted to available data. These formulae have been applied to Saturn’s magnetosphere by Jackman et al. (2004) after taking into account the opposite polarity of Saturn’s magnetic field and the different scale size of the magnetosphere. Specifically, Jackman et al. (2004) suggest that the rate of open flux production at Saturn’s magnetopause, equal to the voltage along the magnetopause reconnection region, can be estimated from the following empirical relation

$$V_{MP} = v_{SW} B_{\perp} L_0 \cos^4(\theta/2), \quad (4.6)$$

where v_{SW} is the radial solar wind velocity, B_{\perp} is the magnitude of the IMF vector perpendicular to the radial flow, and θ is the ‘clock angle’ of this vector measured from the planet’s north magnetic axis projected onto the T-N plane (in RTN coordinates). The open flux production rate according to this formula is therefore at a maximum when the IMF points north ($\theta = 0^\circ$), and reduces to zero when it points south ($\theta = 180^\circ$), opposite to the case of the

Earth due to the opposite polarity of the planetary field. Parameter L_0 in equation (4.6) is a scale length which is equal, when $\theta=0^\circ$, to the width of the solar wind channel, perpendicular to the B_\perp vector, in which the IMF reconnects with the planetary field. Jackman et al. (2004) estimated its value by scaling the empirically-determined corresponding length at Earth by the respective size of the planetary magnetosphere, specifically by the radius of the subsolar magnetopause. Milan et al. (2006) found L_0 at Earth to lie in the range $5 - 8 R_E$, where R_E is Earth’s radius, compared with a subsolar magnetopause radius of $\sim 10 R_E$. At Saturn, the radius of the subsolar magnetopause is $\sim 20 R_S$ (e.g., Behannon et al., 1983), therefore the value of L_0 is taken to lie in the range $10 - 16 R_S$. Jackman et al. (2004) employed the specific value $L_0 = 10 R_S$, which has been used to derive the magnetopause reconnection voltages (open flux production rates) from equation (4.6) shown in the bottom panel of Figure 4.1. (Note that in intervals where no solar wind velocity data are available, we simply used the velocity value nearest in time to calculate the voltage. During days 1-11, for example, we used a constant value of 550 km s^{-1} , representing a reasonable typical value.) Generally, the voltage values follow the modulation of the IMF strength, though with considerable structure superposed through rapid variations in the clock angle, on time scales down to a few tens of minutes. These voltages vary from very small values, $\sim 10 \text{ kV}$ or less, during the weak field rarefaction region, to peaks of $\sim 400 \text{ kV}$ within the major compressions.

Integration of the magnetopause reconnection voltages over time then allows us to estimate the open flux produced over given intervals, and hence the expected accumulation of open flux in the system if tail reconnection is zero. This is shown in the lower panel of Figure 4.5. Here the crosses joined by black lines show the open flux values obtained from the HST images as in Figure 4.4, while the coloured lines show the expected growth in open flux obtained by integrating the estimated magnetopause reconnection voltages. The latter voltages estimated from the Cassini data are shown for reference in the upper panel (with the same time shift as in Figure 4.4), where the blue and red dots correspond to $L_0 = 10$ and $16 R_S$ respectively. The blue and red lines in the lower panel then show the corresponding cumulative integrals of these voltage values. On the left of the figure these lines have been initialised at the open flux value obtained from averaging the five measurements made on V-1, i.e. 47 GWb , such that they show the open flux that would be present versus time if no tail reconnection occurred after V-1. The difference between these lines and the black line at

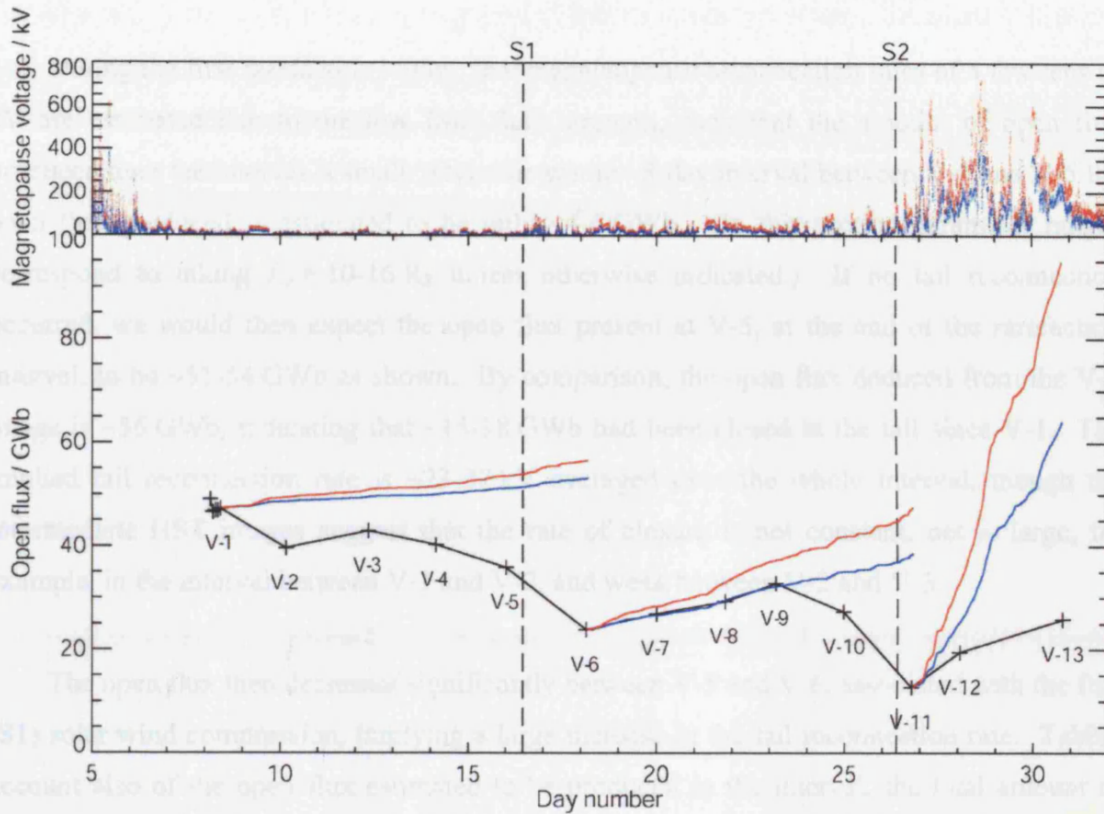


Figure 4.5. The open flux content of the southern polar cap is shown in the lower panel by black crosses joined by the solid black line, as in Figure 4.4. The upper panel presents the magnetopause reconnection voltages estimated from the upstream interplanetary Cassini data using the Jackman et al. (2004) empirical algorithm (see text) with $L_0 = 10 R_S$ (blue) or $16 R_S$ (red). The blue and red lines in the lower panel show the corresponding accumulation of open flux in the system, obtained by integrating the magnetopause voltages over time, assuming no tail reconnection occurs. As in Figure 4.4, the vertical dashed lines mark the estimated arrival times of two solar wind shocks marking the start of CIR-related compressions.

a given time then provides an estimate of the open flux that has been closed in the tail since V-1. The coloured lines are then re-initialised following the auroral contraction events, and major flux closures, observed on V-6 and V-11.

During the first rarefaction region, low magnetopause reconnection rates of a few tens of kV are estimated due to the low IMF field strength, such that the amount of open flux produced over the interval is small. Over the whole ~8-day interval between V-1 and V-5 the open flux produced is estimated to be only ~4-6 GWb. (In this section parameter ranges correspond to taking $L_0 = 10-16 R_S$ unless otherwise indicated.) If no tail reconnection occurred, we would then expect the open flux present at V-5, at the end of the rarefaction interval, to be ~51-54 GWb as shown. By comparison, the open flux deduced from the V-5 image is ~36 GWb, indicating that ~15-18 GWb had been closed in the tail since V-1. The implied tail reconnection rate is ~23-27 kV averaged over the whole interval, though the intermediate HST images suggest that the rate of closure is not constant, but is large, for example, in the interval between V-1 and V-2, and weak between V-2 and V-3.

The open flux then decreases significantly between V-5 and V-6, associated with the first (S1) solar wind compression, implying a large increase in the tail reconnection rate. Taking account also of the open flux estimated to be produced in the interval, the total amount of open flux which is closed between these visits is estimated to be ~14-15 GWb, corresponding to an averaged tail reconnection rate of ~75-81 kV. The instantaneous rates could, of course, be significantly higher. After the compression, the re-initialised coloured lines in Figure 4.5 show that open flux should accumulate more rapidly than before due to the stronger fields present in the intermediate field-strength rarefaction region that follows, where voltage values peak at ~100 kV as seen in the upper panel. The observed increase in open flux inferred from the HST images between V-6 and V-9 closely follows the predicted value for $L_0 = 10 R_S$ (blue line), consistent with essentially zero tail reconnection during the interval, while the values for $L_0 = 16 R_S$ (red line) indicate an overall flux closure of ~5 GWb during this interval associated with a weak averaged tail reconnection rate of ~10 kV. The open flux inferred from the V-10 image, however, falls well below both coloured lines, indicating averaged tail reconnection rates towards the end of the rarefaction region interval, between V-9 and V-10, of ~54-65 kV.

Again taking account of the estimated open flux production, the total open flux inferred to be closed between V-10 and V-11, associated with the second (S2) compression, is then $\sim 18\text{-}20$ GWb, resulting in an estimated averaged tail reconnection rate of $\sim 117\text{-}130$ kV over the interval. After this, the open flux production rates are very large, associated with the strong fields and large magnetopause voltages in the compression region, such that the coloured lines in the lower panel of Figure 4.5 increase much more steeply than before. From a re-initialised value of 13 GWb at V-11, the open fluxes reach values of 64 and 95 GWb (for the blue and red lines respectively) by the end of the image sequence on 30 January. The open flux values inferred from the HST images at V-12 and V-13 are significantly lower than this, however, at 20 and 26 GWb respectively, indicating that as well as the very high magnetopause reconnection rates, averaging $\sim 141\text{-}226$ kV over the interval, there is also a comparable (but slightly lower) reconnection rate in the tail. These observations indicate a system which is strongly driven by the reconnection-mediated solar wind interaction during this 4-day interval.

Our results on reconnection rates during the interval of HST observations are summarised and systematised in Figure 4.6. The top panel again shows the (time-shifted) magnetopause reconnection rates estimated from the Cassini data in the same format as in Figure 4.5, such that the blue and red dots correspond to $L_0 = 10$ and $16 R_S$ in equation (4.6), respectively. The blue and red columns in the second panel then show these values averaged over the intervals between each HST visit, as indicated by the visit numbers shown. The third panel displays the solar wind dynamic pressure in the same format as in Figure 4.4. The bottom panel then shows the corresponding values of the tail reconnection rate averaged between each visit, inferred from the change in open flux observed in the HST images, combined with the open flux production estimate shown above.

It can be seen that during the low-field, low-pressure rarefaction region between V-1 and V-5, the magnetopause reconnection rates are very low, averaging $\sim 6\text{-}10$ kV. The corresponding tail reconnection rates are very variable, between essentially zero and ~ 60 kV, but average to $\sim 23\text{-}27$ kV as indicated above, such that overall the open flux in the system slowly declines. (We note that the small negative tail voltage values inferred during the interval between V-2 and V-3 are of course unphysical, and provide a measure of the uncertainties involved.)

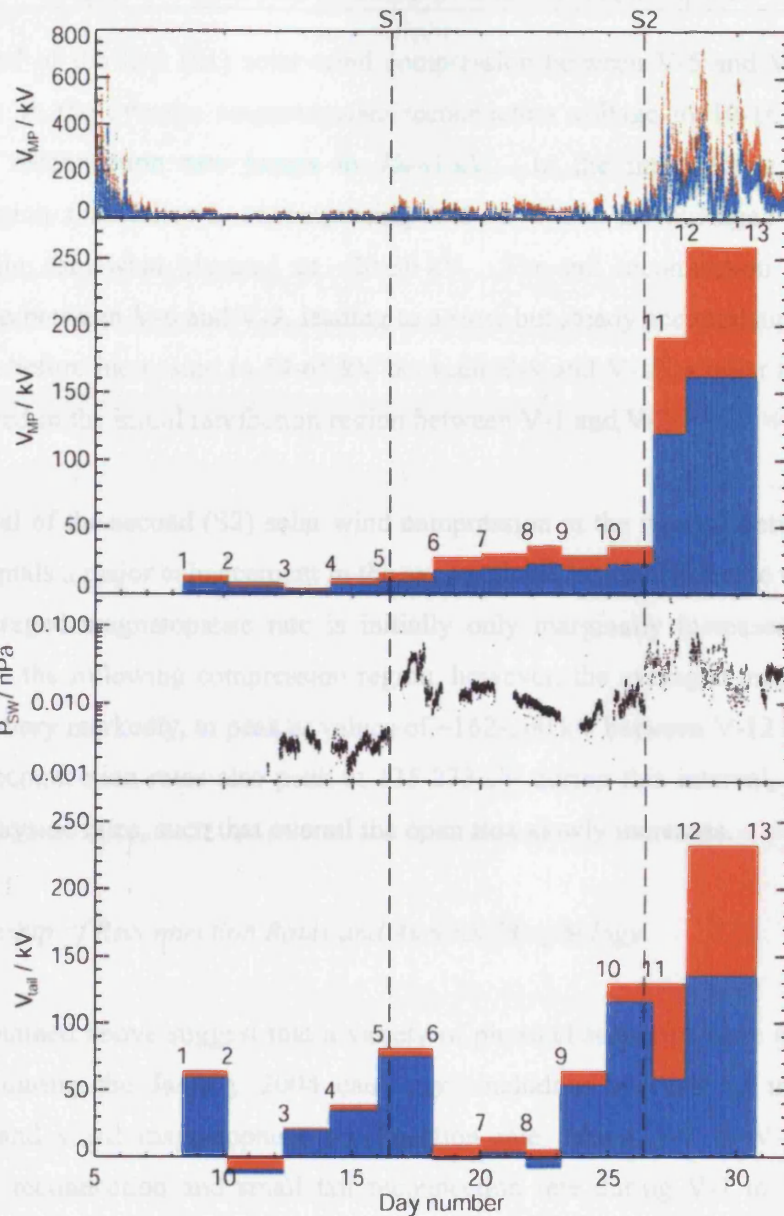


Figure 4.6. Averaged magnetopause and tail reconnection voltages for the intervals between the HST images. The top panel displays the estimated magnetopause reconnection voltages at 1 min resolution according to the Jackman et al. (2004) algorithm with $L_0 = 10 R_S$ (blue) or $16 R_S$ (red), as in Figure 4.5. The red and blue columns in the second panel show these voltages averaged over the intervals between successive HST images, the times of which are marked by the visit numbers 1 to 13. The third panel displays the solar wind dynamic pressure derived from Cassini measurements over the interval. The red and blue columns in the bottom panel show the corresponding averaged tail reconnection voltages, derived by combining the averaged magnetopause reconnection voltages in the second panel with the net change in open flux over the intervals determined from the HST images.

The arrival of the first (S1) solar wind compression between V-5 and V-6 results in a small increase in the average magnetopause reconnection voltage to 10-16 kV, while the averaged tail reconnection rate jumps to 75-81 kV. In the intermediate field strength rarefaction region that follows, encompassing V-6 to V-10, the averaged magnetopause voltages remain somewhat elevated at ~20-30 kV. The tail reconnection rates are then essentially zero between V-6 and V-9, leading to a slow but steady accumulation of open flux in the system, before increasing to 54-65 kV between V-9 and V-10, similar to the peak tail voltages inferred in the initial rarefaction region between V-1 and V-2.

The arrival of the second (S2) solar wind compression in the interval between V-10 and V-11 again signals a major enhancement in the averaged tail reconnection rate to 117-130 kV, while the averaged magnetopause rate is initially only marginally increased. Due to the strong fields in the following compression region, however, the averaged magnetopause rate then increases very markedly, to peak at values of ~162-260 kV between V-12 and V-13. The inferred tail reconnection rates also peak at 135-233 kV during this interval, though remain less than the dayside rates, such that overall the open flux slowly increases.

4.3.3 Relationship of Reconnection Rates and Auroral Morphology

The results obtained above suggest that a variety of physical scenarios were observed in the HST images during the January 2004 campaign, including intervals of intermittent tail reconnection and small magnetopause reconnection rate during V-1 to V-5, intermittent magnetopause reconnection and small tail reconnection rate during V-7 to V-9, large tail reconnection during V-6 and V-11, and large tail and magnetopause reconnection combined in V-12, V-13, and possibly V-10. It is now of interest to re-examine the auroral distributions themselves in the light of these results. Cowley et al. (2004a, 2005a) have described how the auroral emissions expected at Saturn are produced from two sources of precipitation, which give rise to 'discrete' and 'diffuse' aurora respectively. Discrete aurorae are associated with regions of upward-directed field-aligned current located at and near the open-closed field line boundary, which are sufficiently intense to require the downward acceleration of magnetospheric electrons into the atmosphere. Diffuse aurorae, located equatorward of the boundary on closed field lines, are formed by the precipitation into the atmosphere of hot magnetospheric plasma produced principally by tail dynamics, which is trapped on closed flux tubes, and which generally sub-corotates around the outer magnetosphere from its

nightside source. Cowley et al. (2004a) initially discussed steady-state conditions, while Cowley et al. (2005a) considered the features expected in various non-steady reconnection scenarios. A selection of their results pertinent to our discussion is presented in Figure 4.7. These show sketches of the plasma flow (short-dashed arrowed lines), field-aligned currents (circled dots and crosses representing upward and downward flow respectively), and regions of diffuse precipitation (stippled regions) in Saturn’s polar ionosphere, viewed looking down onto the pole with the sunward direction at the bottom and dawn to the left, as in Figure 4.2. The solid line in these diagrams also marks the boundary between open and closed field lines, with active reconnection sites being represented by long-dashed lines terminated by the X symbols.

Figure 4.7a shows the conditions expected for an on-going few-hour burst of tail reconnection in the absence of magnetopause reconnection. A ‘bulge’ of diffuse emission intrudes into the polar cap on newly-closed flux tubes on the nightside, and extends into a growing dawn-side spiral ‘tail’ on closed field lines in the downstream flow. An intense bipolar pair of field-aligned currents also flows within the bulge, forming a system similar to the substorm current wedge at Earth. The current is directed upward on the dawn side of the bulge, giving enhanced ‘discrete’ precipitation in this sector, and extends into enhanced upward currents and discrete aurorae in the dawn boundary region, excited by the enhanced Dungey-cycle flow of closed flux returning to the dayside via dawn. If such reconnection occurs over many hours, comparable to the ~ 20 h sub-corotation time around the planet in the outer magnetosphere, then the aurora will form a spiral pattern extending from the nightside bulge via dawn to noon and beyond. Following Cowley et al. (2005a), we suggest that such a pattern corresponds to that observed during V-6 shown in Figure 4.2c, where in section 3.2 above we inferred the occurrence of strong compression-induced tail reconnection (~ 80 kV averaged over two days) in the absence of strong magnetopause reconnection (~ 10 kV similarly averaged). V-11 (Figure 4.2f) is then suggested to correspond to a more extreme version of such a bulge (also compression-induced) imaged early in its formation.

If, on the other hand, the tail reconnection is intermittent on a time scale which is short compared with the sub-corotation time, the process will result instead in the creation of diffuse auroral ‘patches’ which sub-corotate around the outer magnetosphere, mapping to the region just equatorward of the open-closed field line boundary, as shown in Figure 4.7b. In this case the polar cap is shown to have regained its equilibrium (near-circular) shape, and the

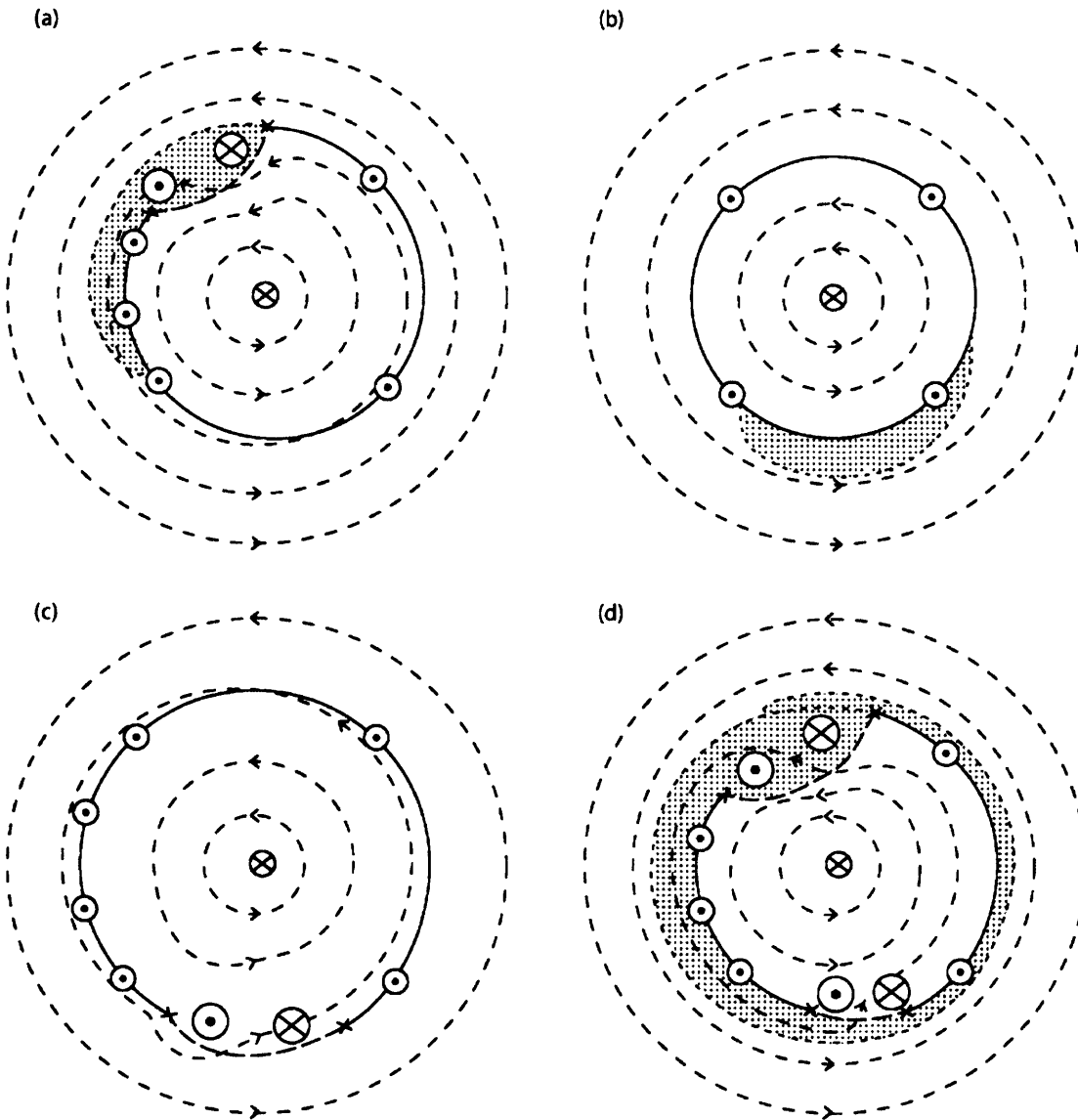


Figure 4.7. Sketches of the plasma flow, field-aligned currents, and diffuse precipitation regimes in Saturn's polar ionosphere. Noon is at the bottom of each diagram, dawn to the left, and dusk to the right (as for the HST UV auroral images shown in Figure 4.2). The outermost circle corresponds to a co-latitude $\sim 30^\circ$ from the pole. The arrowed short-dashed lines show plasma streamlines, while the long-dashed lines marked by X's represent active reconnection lines associated with the Dungey-cycle. The solid line marks the boundary between open and closed field lines. Circled dots and crosses represent upward and downward field-aligned currents, respectively. Their relative intensity is roughly denoted by the size of the symbol. Stippling indicates regions of hot plasma precipitation along closed field lines. The figures represent conditions for (a) an on-going few-hour burst of tail reconnection, (b) a sub-corotating auroral patch formed by a few-hour burst of tail reconnection, (c) an on-going burst of dayside reconnection, and (d) an extended interval of concurrent tail and dayside reconnection.

Dungey-cycle flows have ceased, such that there is no longer a dawn enhancement of the boundary currents and discrete aurorae. Following Grodent et al. (2005), we suggest that this scenario relates to conditions during the first rarefaction region where we have inferred the presence of intermittent tail reconnection (two-day averaged between ~ 0 and ~ 60 kV) in the absence of significant magnetopause reconnection (typically averaging less than 10 kV). The image obtained during V-1.1 shown in Figure 4.2a, for example, may represent an auroral patch observed shortly (a few hours) after its formation, while that obtained during V-4 (Figure 4.2b) shows a patch that has rotated over several hours into the noon sector. In general, patches may be observed at any local time in this case.

Conditions expected for an interval of dayside reconnection in the absence of tail reconnection are shown in Figure 4.7c. In this case the process does not result in an enhancement of diffuse emissions on closed field lines, but still produces a response in the field-aligned currents and discrete aurorae. Specifically, there will now be an intense bipolar current system at noon associated with the reconnection region, as recently discussed by Bunce et al. (2005a), with enhanced upward field-aligned currents again extending around the dawn boundary region from noon. These currents will lead to a related enhancement of discrete aurorae at dawn compared with dusk, now most prominently expressed in the dayside region. According to the above results these conditions apply to the intermediate rarefaction region observed during V-7 to V-9, at least intermittently when the IMF pointed northwards. Magnetopause reconnection rates during the interval average to ~ 20 - 30 kV, with typically less than ~ 10 kV of tail reconnection. The aurorae in these cases generally show an enhancement at dawn compared with dusk, such as that shown for V-9 shown in Figure 4.2d, with a variable morphology in the vicinity of noon which may relate to IMF-dependent cusp emission (Gérard et al., 2005).

Finally, Figure 4.7d illustrates conditions when significant magnetopause and tail reconnection are both in progress over many hours. In this case bipolar field-aligned currents are present in both magnetopause and tail reconnection regions, extending into enhanced upward boundary currents and discrete aurora at dawn. A diffuse auroral spiral also winds from the nightside hours around the boundary via dawn to noon and possibly beyond. The form of the spiral is expected to depend somewhat on the relative rates of magnetopause and tail reconnection prevailing. If the magnetopause reconnection rate is higher than that in the tail (over several hours), then the spiral will be truncated in the noon sector as outer

magnetosphere flux tubes are opened at the magnetopause and transferred to the tail. If, on the other hand, the tail reconnection rate is greater than the magnetopause rate, as illustrated in Figure 4.7d, then a reduced spiral will continue past noon into the dusk sector. However, since magnetopause reconnection is often rather intermittent on hour time scales due to fluctuations in the IMF direction, the latter may represent the more general case, with a narrowed and variable spiral remaining in the post-noon sector. We suggest that this scenario applies to the aurorae observed in V-12 and V-13 shown in Figures 4.2g and 4.2h, where our results indicate the presence of both strong reconnection at the magnetopause and in the tail with comparable averaged rates of $\sim 100\text{-}200$ kV, where the spiral appears to become dimmer, narrower, and/or more intermittent in the post-noon sector. We suggest that the scenario also applies to V-10 shown in Figure 4.2e, where we have also inferred the presence of comparable tail (~ 50 kV) and magnetopause (~ 30 kV) reconnection rates averaged over the preceding interval, though the rates are significantly less than for V-12 and V-13. In this case bright auroral emissions at dawn are truncated in a bright possibly cusp-related auroral spot in the pre-noon sector.

Overall, it seems reasonable to conclude from these results that the observed auroral morphologies are at least qualitatively consistent with expectations based on the inferred magnetopause and tail reconnection rates, according to the picture presented by Cowley et al. (2005a).

4.4 Summary

In this chapter we have considered the data obtained during the Cassini-HST Saturn campaign in January 2004. Data from the Cassini spacecraft obtained in the interplanetary medium upstream of Saturn show that two CIR-related solar wind compressions were observed during the interval, on days 16 and 26, characterised by high field strengths and velocities, surrounded by several-day low-field rarefaction regions (Jackman et al., 2004; Crary et al., 2005; Bunce et al., 2006). Such structured solar wind conditions are typical of the declining phase of the solar cycle so although the data described here is limited in duration, it should be representative of significant periods of each solar cycle. HST images of Saturn’s southern UV aurora obtained during the interval show strong variations in morphology related to these upstream conditions (Clarke et al., 2005; Grodent et al., 2005). Using the poleward edge of the aurora as a proxy for the open-closed field line boundary, the open flux content in

the polar cap has been estimated for each set of images and has been found to vary markedly between 13 and 49 GWb; this variation indicates significant magnetosphere-solar wind interactions during the interval. The magnetopause reconnection voltage (open flux production rate) was also calculated from the upstream conditions using the algorithm proposed by Jackman et al. (2004), and integrated over time to estimate the amount of open flux created at the magnetopause in the (~2 day) intervals between the HST images. Comparison with the open flux values inferred from the HST images themselves then also allows us to estimate the tail reconnection voltage (the rate of open flux closure), averaged over the interval between the images. The observed auroral morphologies have also been related to the reconnection rates derived, and discussed in relation to the theoretical picture presented by Cowley et al. (2005a).

The results are summarised as follows. During an extended rarefaction interval of very low interplanetary field strength and consequent very low magnetopause reconnection rate (typically < 10 kV), we infer the presence of intermittent bursts of flux closure in the tail, averaging up to ~60 kV over ~2 days, which produces irregular sub-corotating auroral patches that can be observed at any local time. In a rarefaction region of intermediate field strength where the magnetopause reconnection voltages were larger, on average 20-30 kV, but the tail reconnection rates were small over an extended interval (< 10 kV), the auroral forms were typically enhanced at dawn and have variable morphologies at noon, taken to be related to the excitation of Dungey-cycle flow and cusp precipitation, respectively. A burst of tail reconnection (averaging ~50 kV) also occurred at the end of the latter rarefaction interval, further increasing the brightness of the dawn emission. CIR-related solar wind compressions induce strong tail reconnection and net open flux closure, characterised by 2-day averaged reconnection voltages of ~70-140 kV. These intervals are associated with bright auroral features in the pre-dawn sector that develop into spiral forms over time. In the extended high-field strength interval that followed the onset of one of the solar wind compressions, both tail and magnetopause reconnection voltages were inferred to be enhanced to averaged values of ~150-250 kV. The aurorae observed during the interval are spiral forms with intense emissions in the pre-dawn to noon sector, and lesser emissions post-noon. These observations are in reasonable qualitative agreement with expectations based on the theoretical picture presented by Cowley et al. (2005a).

Overall our results suggest that reconnection in Saturn's tail can be initiated in two distinct ways. First, it can be initiated during relatively quiet solar wind intervals, possibly by moderate solar wind events which are not CIR compression-related (e.g., Lyons et al., 1997) or by some internal instability triggered when the open flux exceeds a certain threshold. For example, the tail flux increased steadily between V-6 and V-9 without evidence of significant tail reconnection, before tail reconnection began between V-9 and V-10. It seems possible that such events are similar to substorms at Earth. Evidence for 'substorm'-like activity in Saturn's tail has recently been presented by Mitchell et al. (2005), using data from the MIMI instrument on Cassini. Second, larger flux closures can be triggered by the sudden major magnetospheric compressions associated with interplanetary shocks. These events are also known at Earth but are relatively rare compared with ordinary substorms. Their significance at Saturn is enhanced by the generally long time-scales required for the growth of open flux in the tail, several days rather than an hour or two, such that the time-scale for 'substorms' becomes comparable with the interval between CIR-related shock compressions. In either case, bright aurorae would tend to be associated with intervals of reduced open flux, hence the observed anti-correlation between these parameters.

Although our study is limited by the availability of data, it leads to a series of general conclusions that can be addressed using Cassini data. Perhaps the most interesting is the conclusion that tail dynamics can occur intermittently during quiet interplanetary conditions, as well as being initiated by interplanetary compression events. These conclusions should be directly testable using Cassini in situ and remote sensing data. Fuller understanding of auroral morphologies and their relation to interplanetary conditions and Saturn's magnetospheric dynamics, however, will require further joint Cassini-HST studies in the future.

Chapter 5

A statistical analysis of the location and width of Saturn's southern aurora

5.1 Introduction

As discussed in Chapter 2 an auroral oval can be generated either as a result of the interaction between a planet's magnetosphere and the solar wind, or internally due to processes associated with the enforcement of planetary rotation on magnetospheric plasma. The purpose of this chapter is to contribute to an understanding of Saturn's aurorae by providing statistics on the position and width of the observed auroral features. This study incorporates all the available images from HST/STIS, obtained during the interval from 1997 to 2004. During this interval the tilt of Saturn's spin axis relative to Earth was such that only the southern hemisphere aurorae could be observed. In the next section we first describe the images and how they were selected for inclusion in the study. Section 5.2.2 then describes the process of determining the location and width of the auroral oval, and the statistical methods employed. The statistics are presented and interpreted in Section 5.3, and the chapter concludes with a discussion of the results in Section 5.4.

5.2 Observations

5.2.1 Data description and selection

The data set employed in this study consists of the full set of HST images of Saturn's southern aurorae that were obtained between 11 October 1997 and 30 January 2004, during the active lifetime of the STIS instrument. The images were obtained using the FUV photon-counting detector MAMA (Multi-Anode Microchannel Array) in either unfiltered ('clear') mode or filtered mode. In the clear mode the detector has a bandpass between 115 and 180 nm, while the filtered mode uses a SrF₂ filter which rejects wavelengths below ~125 nm, including the strong H Lyman- α emission line and potential geocoronal contamination. The MAMA array has a pixel size of 0.0243 arcsec and a point spread function (PSF) of 0.08 arcsec full width at half maximum.

From the total of 83 images obtained over the above interval, often 2 or 4 images were obtained consecutively on the same HST orbit, revealing essentially the same auroral features. To include all of these images without selection would bias the statistical results. Observations were also occasionally made on consecutive orbits spaced by ~ 90 min, also displaying similar features. More recent observations presented by Gérard et al. (2006) obtained using the HST Advanced Camera for Surveys instrument and not included in this study, have shown that images separated by ~ 5 h (or more) generally reveal significantly different morphologies. Therefore in this study we use only those images spaced by 5 h, i.e. by approximately half a Saturn rotation, or more. Comparison of consecutive filtered and clear images from January 2004 has also shown that the auroral features present in both are not noticeably displaced with respect to each other. It therefore seems reasonable to include both filtered and clear images in our analysis of the aurora’s location, though to maintain consistency, if both filtered and clear images are available, the clear image has been used preferentially. Where two clear images were obtained consecutively on the same orbit, i.e. in the January 2004 set, the two images have been summed to increase the signal to noise ratio. In the cases where two clear images were obtained on consecutive orbits spaced by ~ 90 min, the first of the two images has been used in this study. Details of the 22 images and summed images selected for use in this study according to the above criteria are listed in Table 5.1.

For each image, the STIS field of view was projected onto a planetary latitude-longitude grid using a limb-fitting method described by Grodent et al. (2003, 2005). A selection of six projected images is shown in Figure 5.1, revealing the increasingly complete view of the southern auroral region accessible from 1997 to 2004, as well as the variable morphology and intensity of the observed aurora. The geometry of these plots is such that the observer is looking ‘through’ the planet from the northern into the southern ionosphere, with the sunward direction at the bottom of each image, dawn to the left, and dusk to the right. Longitude in these figures is defined anti-clockwise from midnight, such that dawn corresponds to 90° , noon to 180° , and dusk to 270° . Note that the term ‘longitude’ used throughout this study is equivalent to a local time measurement, and is not a coordinate fixed to the rotating planet. Wherever local times (LT) are also quoted they are written in the format hr:min. The region from the pole to 30° co-latitude is shown in the figure, marked at intervals of 10° co-latitude. Auroral intensities in kR are colour-coded according to the scale shown on the right hand side of the figure.

Table 5.1. Properties of the 22 HST images used in this study

No.	Date dd/mm/yy	Start time / UT	Exposure time / s	Filter	Sub-Earth latitude / deg	Max. brightness / kR
1	11/10/97	0415	774	Clear	-10.3	50
2	11/10/97	1042	754	Clear	-10.3	29
3	20/11/97	1347	1000	Clear	-8.9	45
4	05/12/97	0530	600	Clear	-8.7	28
5	07/12/00	1130	480	SrF ₂	-23.3	108
6	08/12/00	1000	480	SrF ₂	-23.3	52
7	28/01/01	0847	330	SrF ₂	-23.1	40
8	29/01/01	1029	300	SrF ₂	-23.1	56
9	08/01/04	0442	540	Clear	-25.7	49
10	08/01/04	1104	540	Clear	-25.7	31
11	10/01/04	0441	540	Clear	-25.7	31
12	12/01/04	0928	540	Clear	-25.7	47
13	14/01/04	0441	540	Clear	-25.8	29
14	16/01/04	0128	540	Clear	-25.8	27
15	18/01/04	0440	540	Clear	-25.8	82
16	20/01/04	0128	540	Clear	-25.8	43
17	21/01/04	2040	540	Clear	-25.9	29
18	23/01/04	0439	540	Clear	-25.9	30
19	24/01/04	2351	540	Clear	-25.9	47
20	26/01/04	1902	540	Clear	-25.9	83
21	28/01/04	0127	540	Clear	-26.0	122
22	30/01/04	1901	540	Clear	-26.0	64

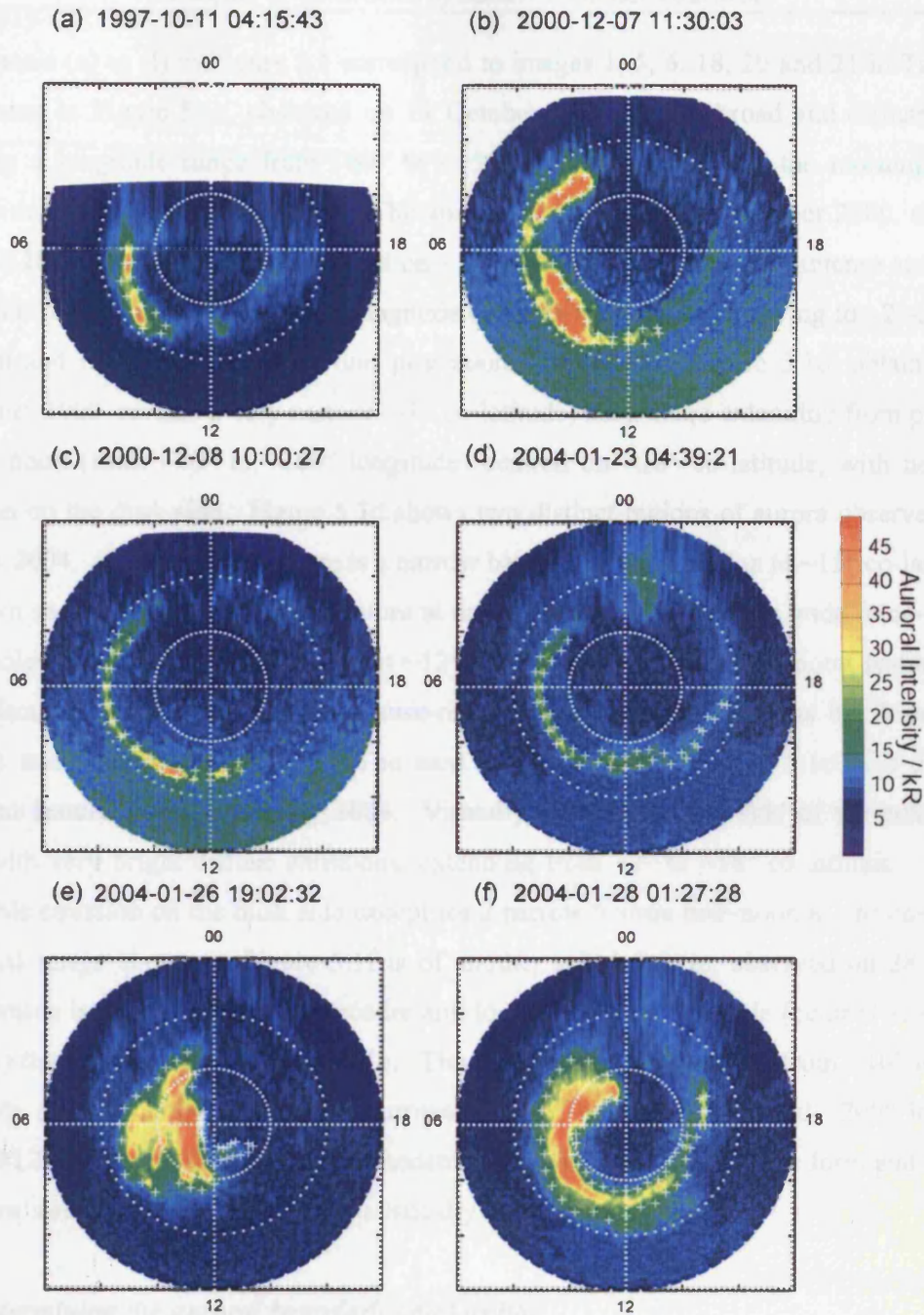


Figure 5.1. Selection of six UV images of Saturn’s southern aurora obtained during the interval 11 October 1997 to 30 January 2004, with the date and start time of each image shown at the top of each plot. Panels (a) to (f) correspond to images numbered 1, 5, 6, 18, 20, and 21 in Table 5.1. The images are projected onto a polar grid from the pole to 30° co-latitude, viewed as though looking ‘through’ the planet onto the southern pole. Noon is at the bottom of each plot, and dawn to the left, as indicated. The UV auroral intensity is plotted according to the colour scale shown on the right-hand side of the figure. The white crosses mark the poleward and equatorward boundaries of the auroral emissions determined as discussed in the text.

Panels (a) to (f) in Figure 5.1 correspond to images 1, 5, 6, 18, 20 and 21 in Table 5.1. The aurora in Figure 5.1a, observed on 11 October 1997, is of a broad and diffuse nature, covering a longitude range from $\sim 80^\circ$ to $\sim 150^\circ$ (05:20-10:00 LT) in the morning sector, centred on $\sim 16^\circ$ to $\sim 17^\circ$ co-latitude. The aurorae observed on 7 December 2000, shown in Figure 5.1b, are again broad and centred on $\sim 17^\circ$ co-latitude, but are more intense and extend in a spiral form from $\sim 30^\circ$ to $\sim 280^\circ$ longitude ($\sim 02:00$ -18:40 LT), narrowing to $\sim 2^\circ$ - 3° width at dawn and noon and becoming dim post-noon. In contrast, Figure 5.1c, obtained on 8 December 2000, reveals a very narrow ($\sim 1^\circ$ co-latitude) auroral arc extending from pre-dawn to post-noon (from $\sim 40^\circ$ to $\sim 200^\circ$ longitude) centred on $\sim 18^\circ$ co-latitude, with negligible emission on the dusk side. Figure 5.1d shows two distinct regions of aurora observed on 23 January 2004. In this example there is a narrow band of bright emission at $\sim 15^\circ$ co-latitude in the dawn sector, but also a diffuse feature at noon that is several degrees wide in co-latitude, lying poleward of the dawn emission at $\sim 12^\circ$ to $\sim 15^\circ$ co-latitude. Such noon features have been discussed in terms of magnetopause-related dayside cusp emissions by Bunce et al. (2005a) and Gérard et al. (2005). The next image shown in Figure 5.1e is a uniquely-observed feature from 26 January 2004. Virtually the entire dawn side of the polar cap is filled with very bright diffuse emissions, extending from $\sim 2^\circ$ to $\sim 18^\circ$ co-latitude. There is negligible emission on the dusk side except for a narrow feature post-noon at $\sim 6^\circ$ co-latitude. The final image shown in Figure 5.1f is of another spiral feature, observed on 28 January 2004, which is generally brighter, broader and located closer to the pole (centred at $\sim 12^\circ$ co-latitude) than that shown in Figure 5.1b. The intense emission extends from $\sim 10^\circ$ to $\sim 300^\circ$ longitude ($\sim 00:40$ -20:00 LT) and is narrower ($\sim 1^\circ$ - 3° co-latitude) beyond $\sim 200^\circ$ longitude ($\sim 13:20$ LT). Overall, these images demonstrate the wide variability in the form and location of Saturn’s aurorae, to be quantified statistically in the sections below.

2.2 Determining the auroral boundaries and widths

The white crosses on each image in Figure 5.1 mark the poleward and equatorward boundaries of the auroral emission, determined using the method now to be described. The latitudinal positions of the auroral boundaries were initially located by eye, looking for peaks in the emission intensity along a given meridian. For simple one-peak profiles the boundaries were then marked by eye at the half-peak power points above the background emission. Two such examples are shown in Figure 5.2 over the co-latitudinal range 0° - 30° , where the red and blue vertical dashed lines mark the poleward and equatorward boundaries, respectively, so

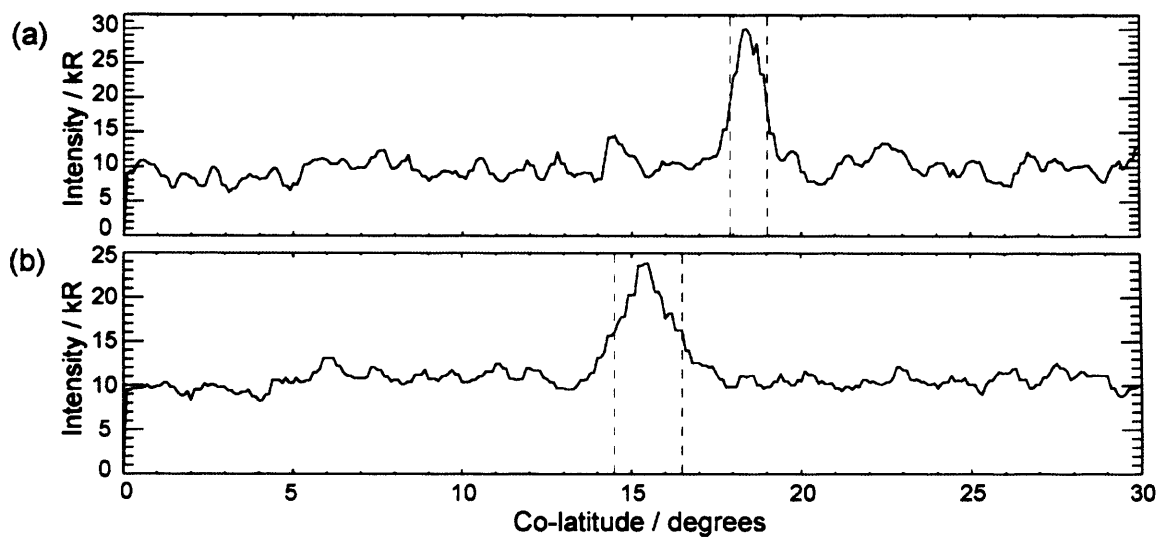


Figure 5.2. Two auroral emission intensity profiles (kR) for co-latitudes 0° – 30° , where the red and blue vertical dashed lines mark the poleward and equatorward boundaries, respectively, of the auroral features, determined as discussed in the text. Panel (a) shows a narrow feature observed at 90° longitude (i.e. dawn) on 8 December 2000 (see Figure 5.1c). Panel (b) shows a more typical broader feature observed at 140° longitude (i.e. pre-noon) on 23 January 2004 (see Figure 5.1d).

determined. Figure 5.2a is an example of a narrow auroral feature at 90° longitude observed on 8 December 2000 (Figure 5.1c). Figure 5.2b shows a broader emission profile observed at 140° longitude on 23 January 2004 (Figure 5.1d). For more complicated profiles, e.g. those that have multiple peaks, the boundary was similarly determined by marking the half-power point in the sharp change in emission intensity on either side of the intensity peaks. Using this method, both the poleward and equatorward boundaries of the emission were recorded at 0.1° latitudinal accuracy at every ten degrees longitude (40 min LT) in each image. The width of the emission was then obtained simply from the difference between the poleward and equatorward positions, with a correction for broadening of features by the PSF to be discussed below. Clearly, the boundaries can only be marked where there is a discernable peak in emission above the background level, such that both poleward and equatorward boundaries can be determined. The number of such ‘good’ data points at each longitude is plotted in Figure 5.3, where longitude is defined as above. The axis at the top of the plot shows the equivalent local time for reference. The distribution peaks broadly at values of 17-19, out of a possible maximum of 22, between 90° (dawn) and 180° (noon), before falling gradually in the post-noon hours to 9 at 270° longitude (dusk). The number of ‘good’ points falls to low numbers (<7) for the longitude range 290°-40° (via midnight). The asymmetry about noon results from the fact that bright auroral features are more commonly observed on the dawn side and at noon than in the afternoon sector. Observations on the nightside are limited in the 1997 data set (see Figure 5.1a), and features visible around midnight become stretched by the projection method, such that there are few ‘good’ data points in the midnight sector. In Figure 5.3 the vertical dashed lines at 50° and 280° longitude mark the limits of the range of longitudes over which we have chosen to perform the statistical analysis, based on there being at least a minimum number of 9 ‘good’ data points. This range extends from the post-midnight sector to just past dusk, via dawn and noon (03:20-18:40 LT).

Before discussing the distributions of auroral boundary positions and widths the limitations imposed by broadening of the auroral features by the instrument PSF of 0.08 arcsec full width at half maximum must be considered. At the distance of Saturn, this corresponds to a distance transverse to the line-of-sight of ~500 km. At the sub-Earth point on the planet this is equivalent to a latitudinal spread of $\Delta\theta_{PSF} \sim 0.5^\circ$. Away from the sub-Earth point the equivalent latitude range increases due to the inclination of the planetary surface to the line-of-sight, but this increase is negligible in the dawn and dusk extremities of the oval. On the noon meridian, however, the projected latitude range corresponding to the

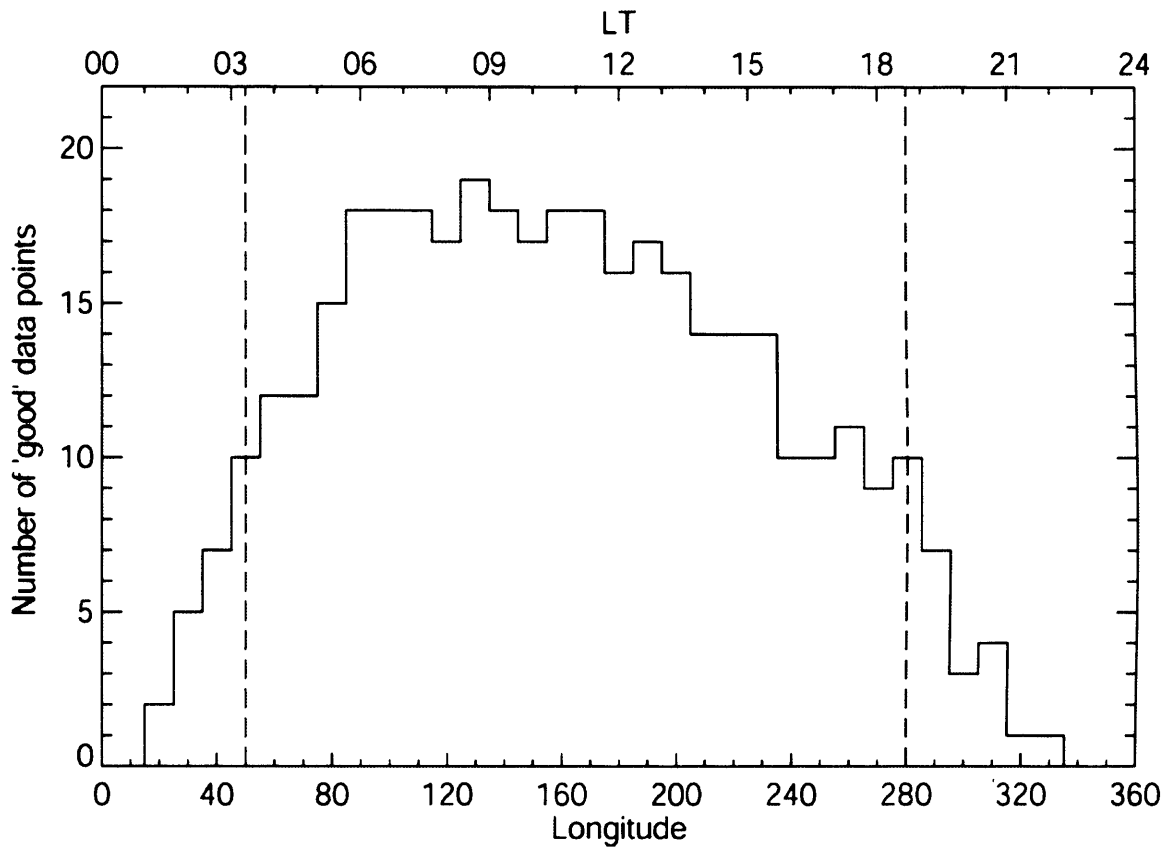


Figure 5.3. Longitude distribution of 'good' auroral boundary data points, i.e. those where there is a discernable peak above the background emission such that both the poleward and equatorward positions can be determined, out of the possible maximum of 22. The vertical dashed lines mark the limits of the range of longitudes (i.e. local times) that are used in this study, based on there being at least a minimum number of 9 data points.

PSF increases to $\Delta\theta'_{PSF} \approx \Delta\theta_{PSF} / \cos\lambda$, where λ is the auroral latitude relative to the sub-Earth point, which is typically $\sim 50^\circ$ for the data examined here (i.e. the auroral latitude relative to the planet’s equator is $\sim 75^\circ$, as will be shown below, while the sub-Earth latitude is $\sim 25^\circ$ as in Table 5.1). Hence at noon we typically have $\Delta\theta'_{PSF} \approx \Delta\theta_{PSF} / \cos 50^\circ \approx 0.78^\circ$. The latitudinal spread associated with the PSF therefore increases from $\sim 0.5^\circ$ at dawn and dusk to $\sim 0.78^\circ$ near noon.

Two consequences follow from this. The first is that when forming histograms of the latitudinal distribution of the auroral boundary positions we should use a bin size that is comparable with or larger than the spread associated with the PSF. Therefore, we have chosen to use a bin size of 1° latitude, a value which is also reasonable considering the positional uncertainties associated with the projection method (Grodent et al., 2005). The second consequence is that the observed auroral widths, determined as described above, will be somewhat increased compared with the actual values. It can readily be shown that if the auroral distribution is approximated as a Gaussian whose true latitudinal width is $\Delta\theta$ (full width at half maximum), then if this is convolved with a PSF which is also taken to be a Gaussian of width $\Delta\theta'_{PSF}$ (full width at half maximum), then the resulting distribution will be another Gaussian whose observed full width at half maximum will be $\Delta\theta' = \sqrt{\Delta\theta^2 + \Delta\theta'^2_{PSF}}$. Consequently we can make a simple correction for the effect of the PSF on the latitudinal widths by calculating $\Delta\theta = \sqrt{\Delta\theta'^2 - \Delta\theta'^2_{PSF}}$. As indicated above, $\Delta\theta'_{PSF}$ varies modestly around the portion of the auroral oval considered in this study from $\sim 0.5^\circ$ near dawn and dusk to $\sim 0.78^\circ$ near noon (for the majority of the observation intervals). Since these represent small corrections for the great majority of the data, we have chosen simply to use a fixed mean value of $\Delta\theta'_{PSF} \sim 0.64^\circ$. We emphasise that the correction to $\Delta\theta'$ is small unless it is very close to $\Delta\theta'_{PSF}$. Consider for example the emission profiles shown in Figure 5.2. The first (Figure 5.2a) is a relatively narrow feature with $\Delta\theta' = 1.1^\circ$. Using the above algorithm the ‘corrected’ width is reduced to $\Delta\theta \sim 0.9^\circ$, which represents only a modest change of $\sim 20\%$. The second example in Figure 5.2b is a more typical profile with $\Delta\theta' = 2.0^\circ$. In this case the ‘corrected’ value is $\Delta\theta \sim 1.9^\circ$, representing a difference of only $\sim 5\%$.

5.3 Distributions of auroral boundary positions and widths

Figure 5.4 shows the co-latitudinal distributions of the poleward (red) and equatorward (blue) auroral boundaries for the longitude range 50° - 280° (03:20-18:40 LT) in the form of histograms, where the ‘probability’ plotted on the ordinate is the occurrence in each co-latitude bin as a fraction of the total number of ‘good’ data points at that longitude. The red and blue vertical dashed lines mark the median co-latitudinal positions of the poleward and equatorward auroral boundaries respectively. Considering first the poleward boundary position, the median values of the latitudinal distributions remain relatively constant over longitude, at 14° - 15° co-latitude for most of the dawn sector, moving poleward to 12° - 13° around noon (160° - 230° longitude), then gradually shifting equatorward to 15° - 16° at dusk. We also see, however, that the poleward boundary position is very variable, covering a large range of 2° - 20° co-latitude when all longitudes are considered. The distribution is widest on the dawn side of the oval, covering this full range of 2° - 20° co-latitude for virtually all dawn sector longitudes (50° - 130°). The distribution narrows to 3° - 19° at 140° longitude (09:20 LT) and has a local minimum of 7° - 16° at noon, i.e. the location of the poleward boundary is twice as variable at dawn than at noon. This variation is also quantified by the standard deviation of the values, which decreases from a maximum of 5.5° at 70° longitude (04:40 LT) to 2.6° at noon. Post-noon the distribution of poleward boundary positions gradually broadens again to 4° - 19° co-latitude (standard deviation 3.7°) at 220° longitude (14:40 LT), then narrows again to a minimum of 12° - 18° (standard deviation 1.6°) at 270° longitude (dusk). The boundary positions with smallest co-latitude, i.e. the points at 2° at dawn and 4° post-noon, correspond to those observed on 26 January 2004 when the dawn side of the polar cap was virtually filled with bright emission (Figure 5.1e). The most expanded poleward boundary locations (20° in the dawn sector and 19° post-noon) occur in the presence of diffuse auroral blobs and narrow arcs in the dawn sector and post-noon (similar to the features shown in Figures 5.1a, 5.1c and 5.1d).

Now considering the equatorward boundary, we first see that the median values are again relatively constant over longitude. On the dawn side (50° - 160° longitude) the median equatorward boundary position is steady at $\sim 16^{\circ}$ - 17° . Around noon (170° - 200° longitude) the median position moves slightly poleward to 15° - 16° co-latitude, then varies between 15° - 18° co-latitude in the remaining range of longitudes towards dusk. Turning now to the latitudinal distributions it can be seen that the boundary location is again very variable, with an overall

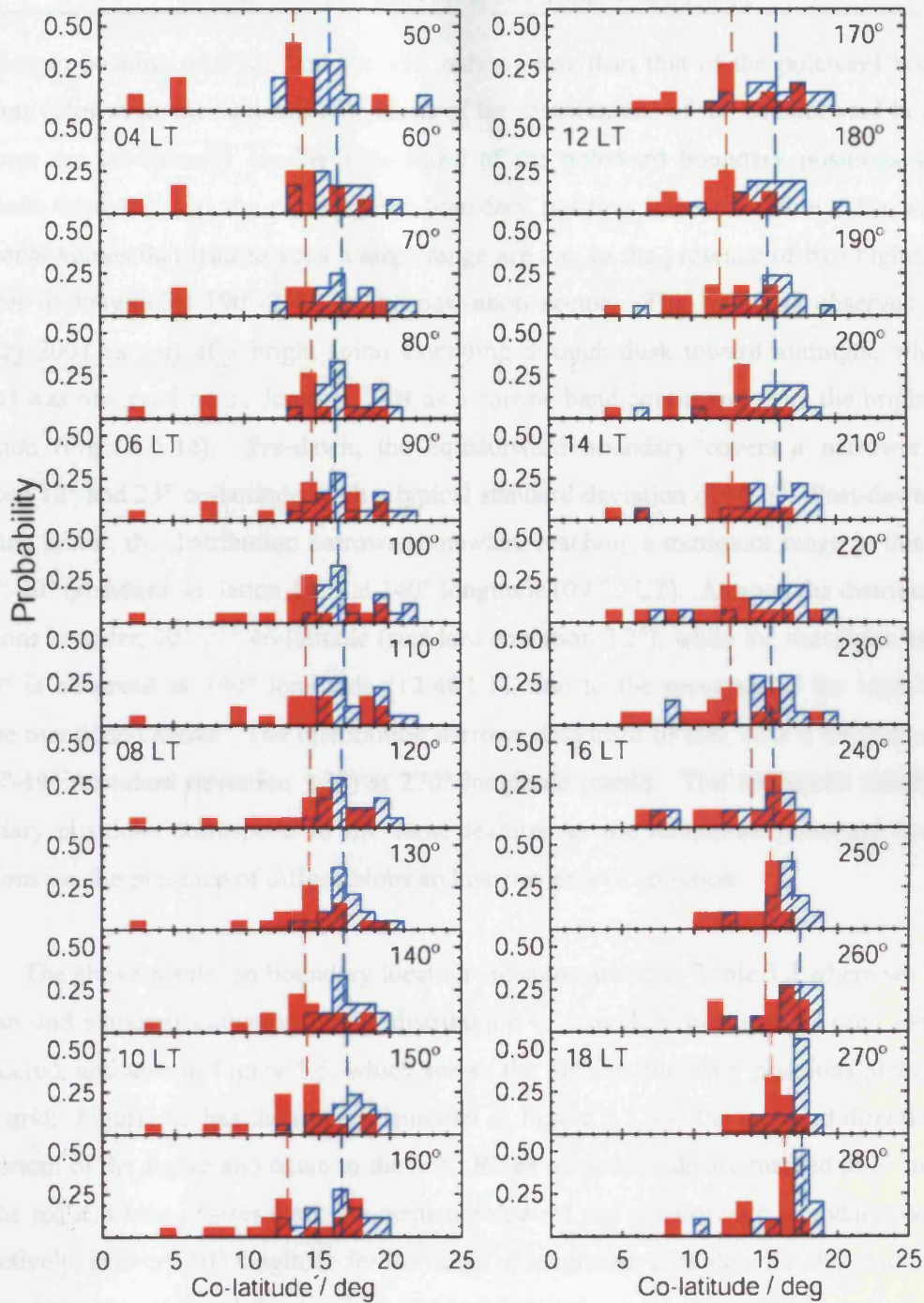


Figure 5.4. Histogram showing the distribution of poleward (red) and equatorward (blue) auroral boundaries over the co-latitude range 0°-25°. Data is shown for the longitude range 50°-280° in 10° steps, where 0° is midnight, 90° dawn, 180° noon, and 270° dusk. The probability plotted on the ordinate is the occurrence in each co-latitude bin as a fraction of the total number of 'good' data points at that longitude. The vertical dashed red and blue lines mark the median co-latitude position for the poleward and equatorward boundaries, respectively, at each longitude.

variation in position of 6°-23° co-latitude, only 1° less than that of the poleward boundary position. However, the standard deviations of the distributions of the equatorward boundary positions are consistently smaller than those of the poleward boundary positions at each longitude implying that the equatorward boundary position is less variable. The smallest positional values that lead to such a large range are due to the presence of two high-latitude features at longitudes 190°-240° in the post-noon sector. The first was observed on 29 January 2001 as part of a bright spiral extending through dusk toward midnight, while the second was observed on 26 January 2004 as a narrow band continuing from the bright dawn emission (Figure 5.1e). Pre-dawn, the equatorward boundary covers a narrower range between 12° and 23° co-latitude, with a typical standard deviation of ~2.5°. Post-dawn in the morning sector, the distribution narrows somewhat, reaching a minimum range in this sector of 14°-20° (standard deviation 1.6°) at 140° longitude (09:20 LT). At noon the distribution of positions is wider, 10°-21° co-latitude (standard deviation 2.2°), while the maximum range of 6°-20° is observed at 190° longitude (12:40 LT), due to the presence of the high-latitude feature mentioned above. The distribution narrows duskward of this, with a minimum range of 14°-19° (standard deviation 1.3°) at 270° longitude (dusk). The maximum equatorward boundary positions correspond to the same features as the maximum poleward boundary positions i.e. the presence of diffuse blobs and narrow arcs of emission.

The above results on boundary location are summarised in Table 5.2 where we list the median and standard deviation of the distribution of boundary positions at each longitude considered, and also in Figure 5.5, which shows the median boundary positions plotted on a polar grid. Figure 5.5 has the same orientation as Figure 5.1, i.e. the sunward direction is at the bottom of the figure and dawn to the left. Rings of co-latitude are marked at 5° intervals and the red and blue crosses mark the median poleward and equatorward boundary positions, respectively, at every 10° longitude for the range of longitudes considered in this study. It can be seen from this plot and the details in Table 5.2 that the average dawn side auroral oval is centred on ~15°-16° co-latitude and has a width of ~1°-2° at dawn. The average oval lies further poleward at noon, centred on ~14° co-latitude, and has a larger width of ~3°-4°. This widening is due to the occurrence of the ‘cusp-related’ auroral features, as shown in Figure 5.1d. Beyond 240° longitude the equatorward and poleward boundary positions are both displaced ~1° equatorward relative to their positions at dawn, while overall the features are of similar width (~1°-2° at dusk). Over all longitudes considered in this study, the median

Table 5.2. Median value and standard deviation of the auroral boundary position and width at each longitude considered

Longitude / deg (LT / hr:min)	Poleward boundary position / deg		Equatorward boundary position / deg		Auroral oval width / deg	
	Median	Standard deviation	Median	Standard deviation	Median	Standard deviation
50 (03:20)	13.5	5.0	16.0	2.8	3.2	3.2
60 (04:00)	14.1	5.0	16.5	2.1	3.1	3.5
70 (04:40)	14.3	5.5	16.8	2.5	2.1	3.7
80 (05:20)	14.7	4.8	16.3	2.0	1.6	3.6
90 (06:00)	14.7	4.4	16.3	2.1	1.4	3.5
100 (06:40)	14.7	4.3	16.5	2.1	1.6	3.4
110 (07:20)	14.2	4.2	16.9	2.0	1.7	3.6
120 (08:00)	14.5	4.0	16.7	1.6	1.8	3.9
130 (08:40)	14.4	3.7	16.8	1.6	1.6	3.1
140 (09:20)	14.1	3.7	16.8	1.6	2.0	3.1
150 (10:00)	14.2	3.8	17.0	2.0	2.5	2.4
160 (10:40)	12.8	3.7	16.6	2.3	2.1	2.3
170 (11:20)	12.9	3.4	16.0	2.4	2.5	1.6
180 (12:00)	12.5	2.6	15.9	2.2	3.4	2.0
190 (12:40)	12.0	3.0	15.3	2.8	2.7	2.0
200 (13:20)	13.0	3.0	15.8	2.9	2.9	1.4
210 (14:00)	12.8	3.2	16.1	3.0	2.6	2.1
220 (14:40)	12.5	3.7	16.3	3.4	2.4	1.9
230 (15:20)	12.6	3.7	15.4	3.2	2.4	1.2
240 (16:00)	14.0	3.4	15.5	3.3	1.4	0.6
250 (16:40)	15.3	2.0	16.8	1.8	1.5	1.3
260 (17:20)	15.0	2.2	17.4	1.7	1.5	1.2
270 (18:00)	15.4	1.6	17.0	1.3	1.0	0.8
280 (18:40)	16.3	2.6	17.5	2.3	1.7	1.1
Overall	13.9	3.8	16.3	2.4	1.9	2.7

median poleward and equatorward auroral boundary positions, plotted on a polar grid with the sunward direction at the bottom of the figure, dawn to the left, and dusk to the right, as in Figure 5.1. Rings of co-latitude are marked at 5° intervals, and lines of longitude at 10° intervals.

To display the width of the auroral oval in more detail, the width of the oval is plotted as a function of local time (LT) in Figure 5.5. The width of the oval is plotted as a function of local time (LT) in Figure 5.5. The width of the oval is plotted as a function of local time (LT) in Figure 5.5.

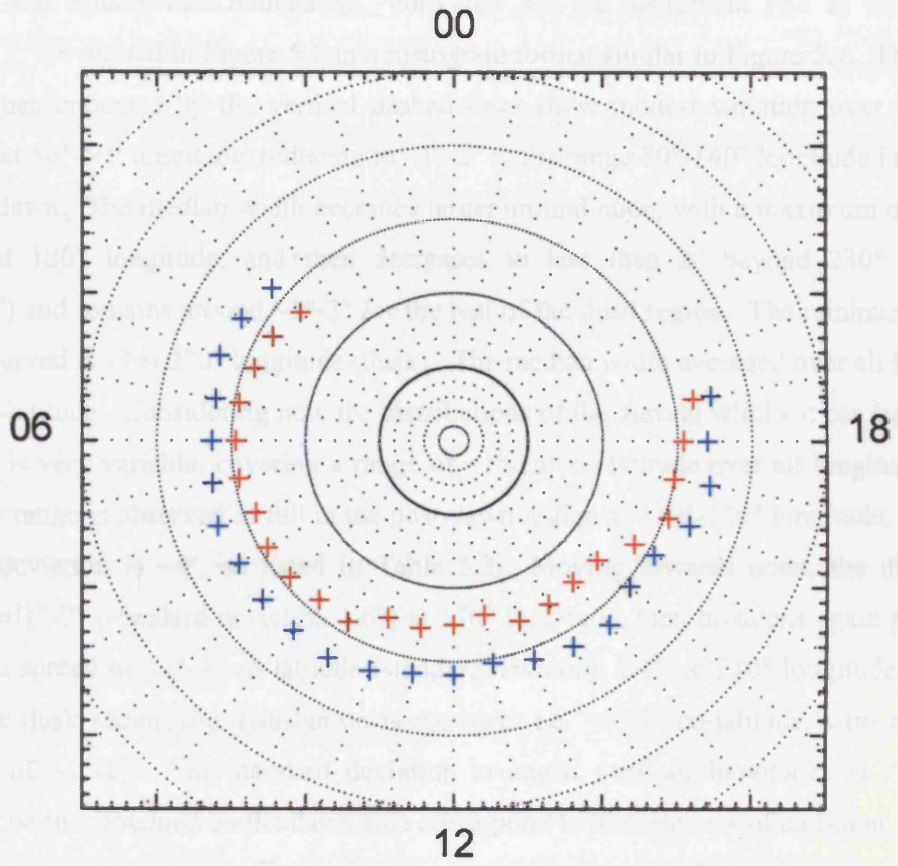


Figure 5.5. The median poleward (red) and equatorward (blue) auroral boundary positions, plotted on a polar grid with the sunward direction at the bottom of the figure, dawn to the left, and dusk to the right, as in Figure 5.1. Rings of co-latitude are marked at 5° intervals, and lines of longitude at 10° intervals.

poleward and equatorward locations are 13.9° and 16.3° co-latitude, with standard deviations of 3.8° and 2.4° , respectively.

To discuss the width of the auroral oval in more detail, the widths calculated from the poleward and equatorward boundaries, ‘corrected’ for the instrument PSF as described in Section 2.2, are plotted in Figure 5.6 in a histogram format similar to Figure 5.4. The median width values indicated by the vertical dashed lines show modest variation over longitude, from $\sim 3^\circ$ at 50° - 60° longitude, reducing to $\sim 1^\circ$ - 2° in the range 80° - 140° longitude i.e. at dawn and post-dawn. The median width becomes larger around noon, with a maximum of 3.4° co-latitude at 180° longitude, and then decreases to less than 2° beyond 230° longitude ($15:20$ LT) and remains around $\sim 1^\circ$ - 2° for the rest of the dusk region. The minimum median width observed is 1° at 270° longitude (dusk). The median width averaged over all longitudes is 1.9° co-latitude. Considering now the distributions of the auroral widths it can be seen that the width is very variable, covering a range of $<1^\circ$ - 16° co-latitude over all longitudes. This maximum range is observed in full in the post-dawn region at 110° - 120° longitude, where the standard deviation is $\sim 4^\circ$, as listed in Table 5.2. Moving towards noon, the distribution narrows to 1° - 7° (standard deviation 1.6°) at 170° longitude, then broadens again post-noon, reaching a spread of $<1^\circ$ - 9° co-latitude (standard deviation 2.1°) at 210° longitude. Beyond this in the dusk sector, the distribution is narrower i.e. $<1^\circ$ - 5° co-latitude, with a standard deviation of $\sim 1^\circ$ - 2° . The standard deviation averaged over all longitudes is 2.7° . The narrowest widths obtained on the dawn side correspond to discrete arcs of emission, similar to the one shown in Figure 5.1b. The very wide auroral features (13° - 16° wide) measured on the dawn side are observed in the image on 26 January 2004 shown in Figure 5.1d. No features this wide are observed on the dusk side, with a maximum width in this sector of $\sim 9^\circ$ at 210° longitude ($14:00$ LT), due to a broad diffuse feature observed on 8 January 2004.

5.4 Summary and discussion

We have analysed a sample of 22 HST images of Saturn’s southern auroral oval, observed during 1997-2004, to statistically determine the average location and width of the aurora, and their variability. Our results indicate that the median auroral oval in the pre-dawn to post-dusk region of Saturn’s southern hemisphere, via noon, is centred on $\sim 15^\circ$ co-latitude, with some modest variation over local time. The oval moves $\sim 1^\circ$ - 2° poleward around noon and is centred $\sim 1^\circ$ further equatorward at dusk relative to dawn. The median poleward boundary

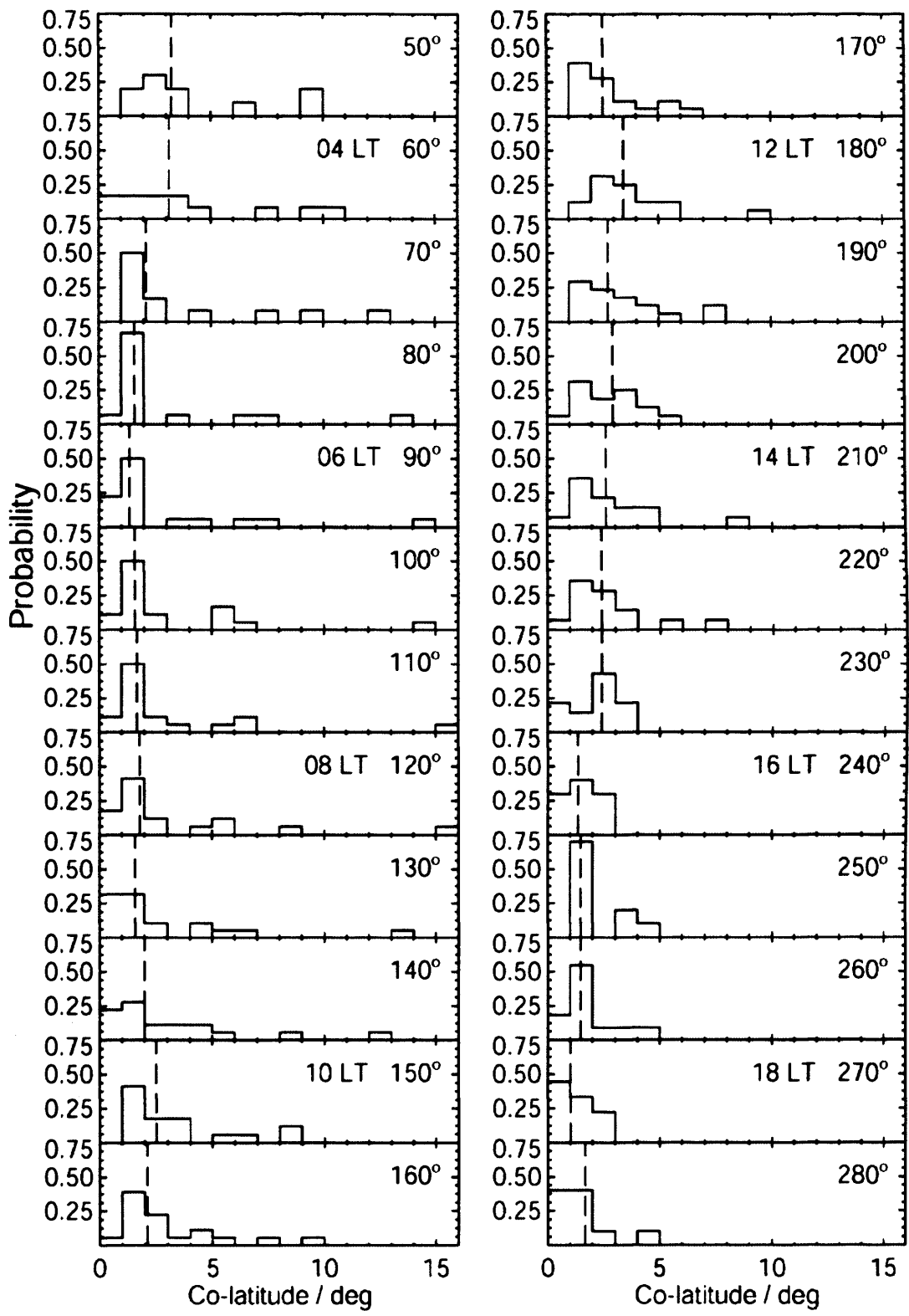


Figure 5.6. Histograms showing the distribution of auroral oval latitudinal widths, plotted in a format similar to Figure 5.4. The vertical dashed lines mark the median width at each longitude.

position is $\sim 14^\circ$ co-latitude over the range of longitudes considered, and the corresponding median equatorward boundary position is $\sim 16^\circ$ co-latitude. Values in the northern hemisphere are expected to be $\sim 1.5^\circ$ closer to the pole than these due to the interhemispheric asymmetry in the quadrupole term of the planet’s internal magnetic field. The median width of the auroral oval is $\sim 2^\circ$ co-latitude, varying over local time from its narrowest of $\sim 1^\circ$ – 2° at dawn and dusk where discrete arcs of emission are observed (e.g. Figure 5.1c), to the widest value of $\sim 3.5^\circ$ at noon, due to the presence of cusp-related diffuse emissions (e.g. Figure 5.1d).

This study has also confirmed and quantified the variability in the location and width of Saturn’s auroral oval. The poleward boundary of the aurora can be found between 2° and 20° co-latitude, with a standard deviation in position of $\sim 4^\circ$ co-latitude. The most poleward of these boundary locations correspond to a very bright diffuse feature observed on 26 January 2004 (Figure 5.1e), which is also the broadest feature observed (16° co-latitude wide), while the boundaries furthest from the pole occur when diffuse blobs of emission or narrow arcs are present (e.g. Figures 5.1a and 5.1c). The equatorward boundary is correspondingly located between 6° and 23° co-latitude, with a standard deviation of $\sim 2.5^\circ$.

We now consider how these results compare with expectations based on the two principal auroral scenarios outlined in Chapter 2, i.e. that the aurorae are formed near the open-closed field line boundary with contributions potentially from both Dungey- and Vasyliunas-cycle dynamics, or that they may be associated with the upward-directed field-aligned current system related to corotation breakdown deeper within the magnetosphere. To aid this discussion, Figure 5.7 compares the co-latitudinal distribution of auroral boundaries derived here (lower panel) with magnetospheric plasma angular velocity data derived from Voyager observations by Richardson (1986) and Richardson and Sittler (1990) (upper panel), which have been normalised to the planet’s angular velocity Ω_S , and mapped into Saturn’s southern ionosphere along model magnetic field lines. We note that related angular velocity data from the Cassini orbiter mission have yet to be published. These plasma data were obtained from the near-equatorial inbound passes of both Voyager-1 (green dots) and Voyager-2 (orange dots), both of which took place at post-noon local times between ~ 13 and ~ 15 LT. The Voyager-2 data span the radial range between the magnetopause at $\sim 19 R_S$ and $\sim 4 R_S$ in the inner magnetosphere, while the Voyager-1 data omit values obtained just inside the magnetopause at $\sim 23 R_S$ due to uncertainty in the identity of the ion species observed in

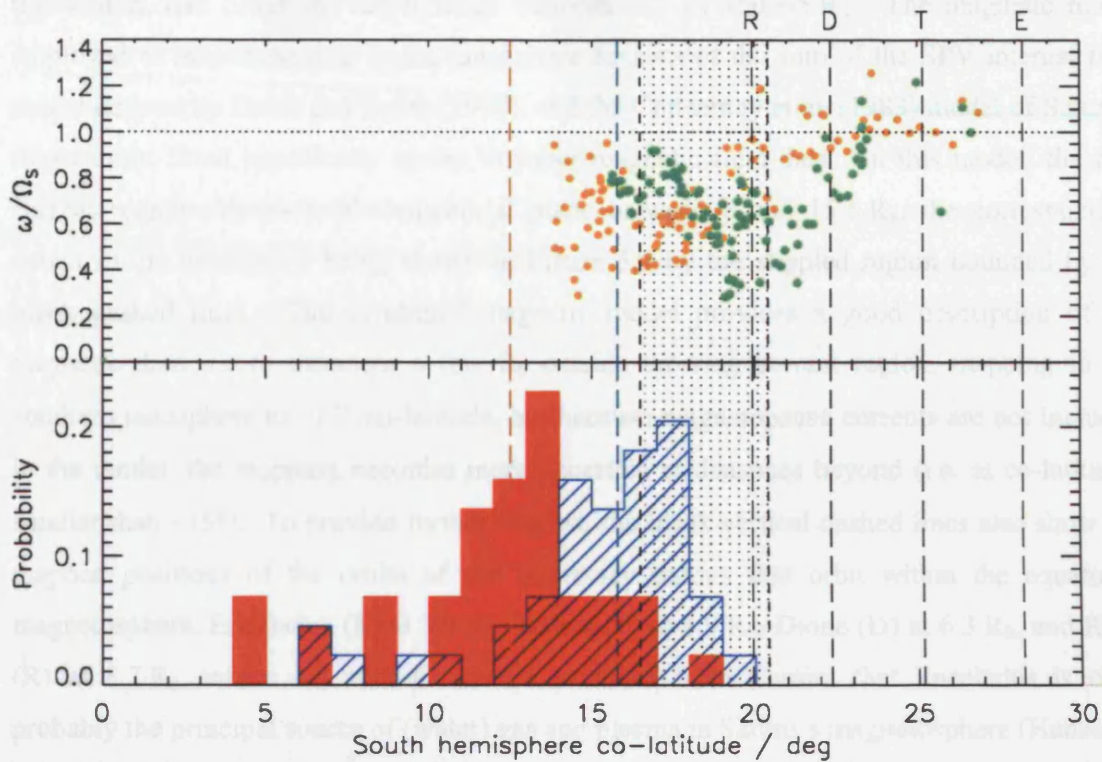


Figure 5.7. Comparison of auroral boundary locations in the post-noon sector (lower panel), with Voyager plasma angular velocity data mapped magnetically into the southern ionosphere (upper panel). The format of the auroral data follows that of Figure 5.4, but here the data from longitudes 200°, 210°, and 220° (13:20-14:40 LT) have been added together to match the local time range of the Voyager data. The data in the upper panel were obtained from the inbound passes of Voyager-1 (green dots) and Voyager-2 (orange dots), both spanning the local time range ~13 to ~15 LT. The angular velocities have been normalised to the planetary angular velocity Ω_S , with rigid corotation, $(\omega/\Omega_S)=1$, being indicated by the horizontal dotted line. The values have been mapped into the southern ionosphere using a magnetic model consisting of the SPV internal field model and the Connerney et al. (1983) Voyager ring current model. The mapped range of the ring current is shown stippled, lying between 8 and 15.5 R_S in the equatorial plane, while the vertical black dashed lines show the mapped orbits of the icy moons Rhea (R), Dione (D), Tethys (T), and Enceladus (E).

this region, and cover the radial range between $\sim 17 R_S$ and $\sim 5 R_S$. The magnetic model employed to map these data to the ionosphere consists of the sum of the SPV internal field model derived by Davis and Smith (1990), and the Connerney et al. (1983) model of Saturn’s ring current fitted specifically to the Voyager magnetic field data. In this model, the ring current region extends in the equatorial plane between 8 and $15.5 R_S$, the corresponding extent in the ionosphere being shown in Figure 5.7 by the stippled region bounded by the black dashed lines. The combined magnetic model provides a good description of the magnetic data out to distances a few R_S outside the ring current region, mapping in the southern ionosphere to $\sim 15^\circ$ co-latitude, but because magnetopause currents are not included in the model, the mapping becomes more uncertain at distances beyond (i.e. at co-latitudes smaller than $\sim 15^\circ$). To provide further context, the black vertical dashed lines also show the mapped positions of the orbits of the larger icy moons that orbit within the equatorial magnetosphere, Enceladus (E) at $3.9 R_S$, Tethys (T) at $4.9 R_S$, Dione (D) at $6.3 R_S$, and Rhea (R) at $8.7 R_S$, where we note the recent evidence from Cassini that Enceladus is most probably the principal source of (water) gas and plasma in Saturn’s magnetosphere (Hansen et al., 2006; Waite et al., 2006). We also note that mapping ‘to the ionosphere’ here specifically means to the surface 1000 km above the planetary 1 bar reference spheroid, as has also been employed in the mapping of the auroral data.

The histograms of auroral boundary locations shown in the bottom panel of Figure 5.7 follow the same format as Figure 5.4, but combine data for longitudes between 200° and 220° (local times between 13:20 and 14:40 LT) in order to match the local time of the Voyager data. The vertical red and blue dashed lines indicate the median positions of the boundaries as before, showing that the auroral oval at these local times lies typically at (southern) co-latitudes between $\sim 12.5^\circ$ and $\sim 15.8^\circ$ in agreement with Figure 5.5. The median equatorward boundary maps magnetically to the equatorial plane at radial distances of $\sim 16.5 R_S$, just outside the stippled Connerney et al. (1983) ring current region, according to our magnetic model. The median poleward auroral boundary then lies poleward of the data from Voyager-2, the most poleward of which maps to the vicinity of the magnetopause as indicated above, and hence to the region just equatorward of the boundary between open and closed field lines. The region sufficiently poleward of the Voyager data then represents open field lines, unexplored on the near-equatorial inbound spacecraft trajectories. While noting the relative uncertainty in the mapping of the outer Voyager-2 data points mentioned above, the results in Figure 5.7 indicate that it is at least plausible that the main auroral oval at these

local times maps typically into the outermost layer of closed magnetospheric field lines beyond the ring current, and possibly onto open field lines as well, associated for example with emissions from the dayside cusp. This inference is also compatible with the estimates of Ness et al. (1981) based on Voyager magnetotail data, that the open-closed field line boundary at Saturn lies in the range $\sim 11^\circ$ - 15° co-latitude, this coinciding with the central part of the distribution of poleward boundary positions in Figure 5.7.

Looking further at the angular velocity data in the upper panel of Figure 5.7, it can be seen that the magnetospheric plasma significantly sub-corotates within the (stippled) ring current region at ~ 50 - 80% of rigid corotation. The plasma angular velocities only begin to rise toward rigid corotation (the horizontal dotted line) near the inner edge of the ring current and at smaller equatorial radial distances. Specifically, the Voyager-2 data start to rise toward rigid corotation near the orbit of Rhea lying just inside the inner ring current region at $\sim 9 R_S$ in the equatorial plane, mapping to $\sim 20^\circ$ co-latitude in the ionosphere, and appear to be consistently near rigid corotation inside $\sim 6 R_S$ near Dione’s orbit, mapping to $\sim 23^\circ$ co-latitude. The Voyager-1 data indicate significant sub-corotation to even smaller equatorial distances of $\sim 6.5 R_S$, mapping to $\sim 22^\circ$ co-latitude, only rising toward rigid corotation inside $\sim 5.5 R_S$, mapping to $\sim 24^\circ$. If we then consider the consequences for field-aligned current flow associated with variations in the equatorward-directed Pedersen current driven in the ionosphere by plasma sub-corotation, it can firstly be seen that there is much scope for small-scale structures to be present throughout the sub-corotating region associated with small-scale variations in the plasma angular velocity, as discussed previously and modelled by Cowley and Bunce (2003c) and Cowley et al. (2004b). However, the main upward-directed field-aligned current, equivalent to that believed to be associated with the main oval at Jupiter, will flow where the plasma angular velocity increases from significant sub-corotation in the ring current region (and beyond) towards consistent near-rigid corotation at smaller radial distances. The Voyager-1 and -2 data in Figure 5.7 then indicate that this occurs between equatorial radial distances of ~ 9 and $\sim 6 R_S$, mapping to $\sim 20^\circ$ - 24° co-latitude in the ionosphere. These locations lie well equatorward of the typical position of the aurorae indicated by the median boundaries, indeed, they do not overlap the auroral distribution at these local times at all. It therefore seems reasonable to conclude on this basis that Saturn’s auroral oval is most probably located near the open-closed field line boundary, rather than being related to the main corotation-enforcement current system as is believed to be the case at Jupiter, in agreement with the earlier conclusions of Cowley and Bunce (2003c) and

Cowley et al. (2004b). In this case we expect the aurorae at Saturn to be associated with Dungey-cycle and possibly Vasyliunas-cycle dynamics, thus also explaining the persistent dawn-dusk local time asymmetries which are observed, as can be seen in Figure 5.1 (Cowley et al., 2004a, 2005a; Jackman and Cowley, 2006).

The other major feature of our results concerns the considerable variability in the position of the auroral boundaries at Saturn, contrasting sharply with the behaviour of Jupiter’s main oval, which varies in latitude at a given planetary longitude by at most $\sim 2^\circ$ even during intervals of strong solar wind disturbance (Grodent et al., 2003; Nichols et al., 2007). However, if the aurorae at Saturn are located near the open-closed field line boundary, as discussed above, this variability is reasonably explained in terms of variations in the amount of open flux present in the system. An indication of the magnitude of the changes in open flux which may be anticipated to occur in the Dungey-cycle at Saturn can be obtained by considering the corresponding variations at Earth. In a study of a very active interval Milan et al. (2004) found that the open flux in the terrestrial system varied between $\sim 2.5\%$ and $\sim 12\%$ of the total planetary magnetic flux, where the minimum value followed a strong magnetospheric compression by the solar wind and the onset of a large substorm. Subsequent analysis of a larger data set by Milan et al. (2007) has confirmed that the above values fully span the usual range of open flux fractions at Earth. The corresponding range at Saturn cannot be inferred in a simple way from the range in poleward boundary locations found above in our study, because the highest-latitude boundaries in particular are associated with asymmetric auroral distributions occurring during disturbed intervals, as can be seen in Figure 5.1. However, in the study presented in Chapter 4 (and described by Badman et al., 2005) we numerically computed the magnetic flux present in the ‘dark’ region bounded by the auroral oval at Saturn using the data set obtained during the HST-Cassini campaign in January 2004, which spanned nearly a full solar rotation. The results from that study showed that the flux varied between ~ 13 and ~ 49 GWb, corresponding to between $\sim 3\%$ and $\sim 10\%$ of the total flux threading the ionosphere (~ 475 GWb). The smallest values again correspond to disturbed conditions following the impact of a solar wind corotating interaction region compression on the magnetosphere. The close correspondence between these fractional values and those observed at Earth at least lends plausibility to the open flux interpretation of the ‘dark’ polar region at Saturn.

If we accept the conclusion of the above discussion, then the poleward boundary of the auroral emission at Saturn can be used as a proxy for the boundary between open and closed field lines, as assumed in the study described in Chapter 4. On the dayside this boundary consequently maps magnetically to the vicinity of the dayside magnetopause. Very narrow arcs at this boundary, such as that shown in Figure 5.1c, may then correspond simply to a region of upward-directed field-aligned current, as, for example, in the theoretical model of Jackman and Cowley (2006). However, it seems reasonable to suppose that broader features, such as those seen e.g. in Figures 5.1a, 5.1b, and 5.1f, can also be formed by precipitation from regions of hot magnetospheric plasma on closed flux tubes, that may be injected on the nightside and then sub-corotate around the boundary into the dayside magnetosphere. In this case, the width of the auroral features reflects the radial extent of the hot plasma region adjacent to the magnetopause boundary, which can then be estimated from the oval width by conservation of magnetic flux. We consider a segment of the auroral oval of azimuthal extent $\Delta\varphi$, located at a co-latitude θ , and of latitudinal width $\Delta\theta$. The magnetic flux threading this region of the ionosphere is then $\Delta\Phi = B_i R_i^2 \sin\theta \Delta\theta \Delta\varphi$, where B_i is the magnitude of the near-radial magnetic field in the ionosphere, and R_i is the ionospheric radius. Assuming that this maps magnetically into the equatorial plane in a region of width l adjacent to the magnetopause at radius R_{MP} , then we also have $\Delta\Phi \approx B_e l R_{MP} \Delta\varphi$, where B_e is the equatorial field strength, and we have assumed for simplicity that the field lines lie in meridian planes. Equating magnetic fluxes we then find

$$l \approx \frac{B_i}{B_e} \frac{R_i^2}{R_{MP}} \sin\theta \Delta\theta.$$

The radius of the polar ionospheric layer is $R_i \approx 55\,400$ km (~ 1000 km above the 1-bar reference spheroid), while the radial field strength in the southern ionosphere is $B_i \approx 60\,000$ nT according to the SPV model (Davis and Smith, 1990). We also take typical equatorial values of $R_{MP} \approx 22 R_S$ and $B_e \approx 5$ nT. Then for a typical auroral distribution with $\theta \approx 15^\circ$ and $\Delta\theta \approx 2^\circ$ (the median values found in our study), we find a value $l \approx 4 R_S$. This value may be somewhat reduced if the dayside field lines spread meridionally away from noon as they do at Earth (e.g. Fairfield, 1968). Nevertheless, we may conclude that the auroral widths found here imply the existence of hot plasma layers inside the magnetopause

whose width is typically several planetary radii, which occupy some fraction of the region between the magnetopause and the outer edge of the ring current, as in the above discussion. It will be interesting in future work to test this inference using in situ plasma data from the Cassini spacecraft.

Chapter 6

Significance of Dungey-cycle flows in Jupiter's and Saturn's magnetospheres and their identification on closed equatorial field lines

6.1 Introduction

This chapter discusses the relative magnitudes of the flux transport by rotational and Dungey-cycle dynamics in Jupiter's and Saturn's magnetosphere, and suggests how the contribution of the Dungey-cycle may potentially be identified in equatorial flows. The next section discusses the nature of the overall flow system before making estimates of the contributions from the rotational and Dungey-cycle flows in following sections.

6.2 Equatorial flows

Conceptual models of the large-scale magnetospheric field and flow containing both rotational/Vasyliunas-cycle and Dungey-cycle systems have been discussed for Jupiter by Cowley et al. (1996, 2003), and for Saturn by Cowley et al. (2004a). The equatorial flow in the Saturn model discussed by Cowley et al. (2004a) is sketched in Fig. 2.3, and was described in Chapter 2, section 2.3; the flow in the Jupiter model is essentially similar. A central purpose of these models was to show how the two flow systems can co-exist on a continuous basis. It is nevertheless recognised that in reality both Vasyliunas-cycle and Dungey-cycle processes are likely to be time-dependent (e.g. Woch et al. 2004; Cowley et al., 2005a,b), and may also involve nightside flows that are more spatially structured than those depicted here, as speculated upon for the case of Jupiter by Kivelson and Southwood (2005).

In terms of the observed plasma regions in Jupiter's magnetosphere, we suppose that the mass-loaded sub-corotating region corresponds to the jovian 'middle magnetosphere', which is dominated by the presence of an equatorial plasma-current sheet containing outwardly-diffusing cool plasma from the volcanic moon Io. Similarly at Saturn, the sub-corotating ring current region contains outwardly-diffusing plasma from the icy moons and rings. We also suppose that the surrounding region of mass-reduced flux tubes flowing around the boundary

via dawn from the Vasyliunas- and Dungey-cycle reconnection sites in the tail together form the ‘outer magnetosphere’ region on the dayside, characterised by relatively strong southward-pointing fields in the equatorial plane and the lack of a central current sheet, as originally suggested for Jupiter by Cowley et al. (1996). In subsequent discussions of the jovian system Cowley et al. (2003, 2005b) emphasised the Dungey-cycle contributions to this layer, while Kivelson and Southwood (2005) emphasise the Vasyliunas-cycle contribution. Here we will discuss in more detail the relative contributions of these two processes to the formation of the layer, at both Jupiter and Saturn. In the previous chapter we estimated the potential width of this layer at Saturn to be $\sim 4 R_S$ by assuming that it contains hot plasma (accelerated from tail reconnection sites) which precipitates into the ionosphere and generates the observed aurorae. We recognise that the character of the layer will evolve as the plasma is transported from dawn around the dayside, due to reconnection-associated flux erosion at the magnetopause as depicted in Fig. 2.3, as well as to radial transport of plasma from the interior region (Kivelson and Southwood, 2005).

6.3 Rotational and Dungey-cycle flux transport at Jupiter and Saturn

It is evident from the above discussion that the flux transport driven by planetary rotation and by the Dungey-cycle will dominate in differing parts of the magnetosphere. Generally, rotation-driven flows will dominate in the inner regions of closed field lines, while the Dungey-cycle is critical in the formation of open tail lobes, which, at Jupiter, extend anti-sunward of the planet by several AU to roughly the orbit of Saturn (Behannon et al., 1983; Cowley et al., 2003). It is nevertheless important for an overall understanding of the nature of these systems to compare quantitatively the flux transport due to these processes, such that we can assess, for example, the contribution of the Dungey-cycle return flows to the equatorial transport in the outer magnetosphere. These topics are conveniently discussed in terms of the relative voltages associated with the motional electric field $\mathbf{E} = -\mathbf{v} \times \mathbf{B}$ due to these flow systems, where \mathbf{v} is the plasma velocity and \mathbf{B} the magnetic field, since by Faraday’s law a voltage of 1 V corresponds to a flux transport of 1 Wb s^{-1} . In this section we first review recent results concerning the Dungey-cycle voltage at Jupiter and Saturn, and then compare them with estimates of the flow driven by planetary rotation.

6.3.1 Flux transport associated with Dungey-cycle flow

Until recent times only rather crude spot estimates had been made of the magnetopause reconnection rates that initiate the Dungey-cycle at Jupiter and Saturn (e.g. Kennel and Coroniti, 1975). Recently, however, more detailed estimates have been published, based on the growing collection of interplanetary data obtained in the vicinity of the planetary orbits by the Ulysses and Cassini spacecraft (Jackman et al., 2004; Nichols et al., 2006). These studies employed an empirical formula for the magnetopause reconnection voltage in terms of upstream interplanetary parameters, which was validated and adapted from studies at the Earth (e.g. Perrault and Akasofu, 1978; Milan et al., 2004), given by

$$V_{DC} = v_{sw} B_{\perp} L_0 \cos^4(\theta/2) \quad , \quad (6.1)$$

as used in Chapter 4. Here again v_{sw} is the velocity of the solar wind, B_{\perp} is the magnitude of the interplanetary magnetic field (IMF) vector perpendicular to the flow, and θ is the ‘clock angle’ of this vector measured from the planet’s north magnetic axis projected onto a plane perpendicular to the planet-Sun line. Length L_0 is then such that the field-perpendicular width of the solar wind channel which reconnects with the planetary field is given by $L_0 \cos^4(\theta/2)$. This width is a maximum equal to L_0 when $\theta = 0^\circ$ i.e. when the IMF points northward opposite to the equatorial planetary field, and falls to small values beyond $\theta \sim 90^\circ$. From a study of reconnection rates at Earth, Milan et al. (2004) found a value for the scale length $L_0 \sim 5R_E$ i.e. approximately half the sub-solar magnetopause stand-off distance. For Jupiter and Saturn L_0 has therefore been scaled according to the size of the magnetospheres, such that $L_0 \sim 30R_J$ (on average) at Jupiter, while $L_0 \sim 10R_S$ at Saturn.

The interplanetary medium at the orbital distances of Jupiter and Saturn typically exhibits strong variations during each ~25-day solar rotation due to the effect of both corotating interaction regions (CIRs) and coronal mass ejection (CME) events. As a consequence, the reconnection voltages estimated from Eq. (6.1) show corresponding strong temporal variations over such intervals due principally to changes in the strength of the IMF, upon which further modulation is superposed at shorter periods due to the clock angle effect. Lowest field strengths and voltages occur during several-day CIR rarefaction regions during

which the solar wind speed falls with time, while highest field strengths and voltages occur during few-day CIR compression regions when the solar wind speed increases (usually across paired shocks) and during few-day CMEs. These trends were also noted in the study of reconnection rates at Saturn presented in Chapter 4. Considering first the results for Jupiter, Nichols et al. (2006) studied three extended intervals of Ulysses data as the spacecraft flew near Jupiter’s orbital path during 1992, 1998 and 2004, and one further interval of data obtained by Cassini during its fly-by of Jupiter at the end of 2000. These data span a complete solar cycle, though the variations over the cycle were found to be relatively modest. Typical magnetopause reconnection voltages were estimated to be $V_{DC} \sim 150$ kV during rarefaction regions, which occur $\sim 90\%$ of the time, increasing by an order of magnitude to $V_{DC} \sim 1$ MV during CIR compressions and CMEs, which occur $\sim 10\%$ of the time (i.e. in one or two intervals of ~ 2 -3 days total duration during each solar rotation). These and subsequent voltage values are listed in Table 6.1, for purposes of comparison. The open flux produced during the extended rarefaction intervals integrates to ~ 300 GWb over one solar rotation, while that produced in the relatively short-lived compression regions integrates to ~ 200 GWb. The total open flux produced over a solar rotation is then ~ 500 GWb, corresponding to an overall average magnetopause reconnection rate of ~ 250 kV. Since the jovian magnetotail contains ~ 300 -500 GWb of flux per lobe, the averaged tail flux replenishment time is estimated to be ~ 15 -25 days, with a consequent tail length of ~ 4 -6 AU consistent with the above discussion.

Considering now the case for Saturn, Jackman et al. (2004) employed a ~ 6 -month interval of interplanetary data measured by Cassini as it approached Saturn at the start of 2004, corresponding to the declining phase of the solar cycle. Their results (again listed in Table 6.1) indicate typical reconnection voltages of $V_{DC} \sim 25$ kV during rarefaction regions, which occur $\sim 85\%$ of the time, increasing to $V_{DC} \sim 150$ kV during CIR compressions, which occur $\sim 15\%$ of the time (i.e. one or two intervals of ~ 4 days total duration during each solar rotation). The open flux produced during rarefaction regions then integrates to ~ 50 GWb in each solar rotation, while that produced in compression regions also integrates to ~ 50 GWb. The total amount of open flux created is then ~ 100 GWb per solar rotation, corresponding to an averaged magnetopause reconnection rate of ~ 45 kV. Since the kronian magnetotail contains ~ 25 -40 GWb of open flux per lobe, the averaged tail flux replenishment time is estimated to be ~ 6 -10 days, with a consequent tail length of ~ 1.5 -2.5 AU.

Table 6.1. Summary of estimated Dungey-cycle and rotational voltages for Jupiter and Saturn

Voltage estimates	Jupiter / MV	Saturn / MV
Rotational voltage (total)	400	12
Rotational voltage (middle magnetosphere or ring current region)	2.5	0.4-0.6
Rotational voltage (outer magnetosphere)	2-4	0.18
Dungey-cycle voltage (compression region)	1	0.15
Dungey-cycle voltage (rarefaction region)	0.15	0.025
Dungey-cycle voltage (average)	0.25	0.045

It should be noted here that the values determined above using Eq. (6.1) are estimates of the reconnection rate at the magnetopause, while we are particularly interested in the Dungey-cycle contribution to flux transport on closed field lines in the outer magnetosphere following reconnection in the tail, as depicted in Figure 2.3. It is firstly evident that the averaged Dungey-cycle tail reconnection rate, and consequent closed flux transport rate in the outer magnetosphere, must be equal to the averaged magnetopause reconnection rate, estimated above to be ~ 250 kV at Jupiter and ~ 45 kV at Saturn. Beyond this it seems reasonable to assume that the tail reconnection rate approximately follows the variations in the magnetopause reconnection rate during each solar rotation, such that the averaged tail reconnection rate at Jupiter would be ~ 150 kV during rarefaction regions, increasing to ~ 1 MV during CIR compression regions and CMEs. The corresponding values for Saturn are ~ 25 kV for rarefaction regions and ~ 150 kV for compressions, in good agreement with the findings presented in Chapter 4 (and also by Badman et al., 2005) based on analysis of auroral data from the January 2004 Cassini-HST campaign. In addition to this, however, we note that at Earth tail reconnection tends to be impulsive, resulting in substorms and other nightside flow burst phenomena that may be triggered internally or by interplanetary events (e.g. Lyons et al., 1997; Boudouridis et al., 2003, 2004; Milan et al., 2007). The consequence is that while the magnetopause reconnection rate at Earth, averaged over all interplanetary conditions, is ~ 30 kV, the typical tail reconnection rate, when it occurs, is ~ 90 kV, lasting for about one third of the time (Milan et al., 2004, 2007). It should therefore be recognised that the typical tail reconnection rates at Jupiter and Saturn, when they do occur, may be higher than the magnetopause reconnection rates estimated above, but lasting for correspondingly shorter intervals. If a similar factor of three applies at Jupiter as at Earth, for example, the tail reconnection rate might be ~ 3 MV during compression regions, though occurring for a total of only ~ 1 day during each solar rotation. Similarly, the tail reconnection rate at Saturn might be ~ 450 kV, occurring for a total of ~ 1.5 days per solar rotation according to the above discussion.

6.3.2 Flux transport associated with rotational flow and comparison with the Dungey-cycle

We now consider the flux transport driven by the planetary rotation and compare it with that due to the Dungey-cycle flows considered above. The potential V_{ROT} associated with the rotation of magnetic flux Φ at angular velocity ω around an annular region in the equatorial magnetosphere extending from radial distance $r=0$ to $r=R$ is found by integrating the

motional electric field radially across the annulus: $V_{ROT} = \int_0^R E dr = \int_0^R r \omega B(r) dr$. Taking a

factor of $\frac{\omega}{2\pi}$ outside the integral we obtain $V_{ROT} = \frac{\omega}{2\pi} \int_0^R 2\pi r B(r) dr$, where the value of the

integral is equal to the amount of magnetic flux through the area of the annulus: Φ . Therefore the rotational flux transport and voltage associated with the flow is given by

$$V_{ROT} = \frac{\Phi \omega}{2\pi} . \quad (6.2)$$

Generally the plasma will sub-corotate at a fraction k of the planet’s angular velocity Ω_p , such that $\omega = k \Omega_p$, where for sub-corotation $0 < k < 1$. We then have

$$V_{ROT} = \frac{k \Phi \Omega_p}{2\pi} = \frac{k \Phi}{T_p} , \quad (6.3)$$

where $T_p = 2\pi/\Omega_p$ is the planetary rotation period. Previous simple estimates of the rotational voltage have generally considered the whole of the planetary flux over a given hemisphere and have assumed rigid corotation ($k = 1$), as will initially be assumed here. To estimate the amount of flux in one hemisphere we integrate the principal dipole component of the internal planetary field over the hemisphere. For Jupiter we use the VIP-4 jovian magnetic field model derived by Connerney et al. (1998) to estimate the total hemispheric magnetic flux to be ~ 14000 GWb, such that for rigid corotation with a ~ 9.9 h rotation period, the associated flux transport is $V_{ROT} \sim 400$ MV (Table 6.1). Similarly, using the Cassini model of Saturn’s magnetic field (Dougherty et al., 2005), we find that at Saturn the total hemispheric magnetic flux is ~ 480 GWb, so that with a ~ 10.8 h rotation period we obtain $V_{ROT} \sim 12$ MV (Table 6.1). It may be thought that these voltage values represent overestimates since the plasma sub-corotates throughout much of the outer magnetosphere. However, this sub-corotation region maps to within $\sim 20^\circ$ of the magnetic pole at Jupiter and within $\sim 25^\circ$ of the pole at Saturn, corresponding to only $\sim 10\%$ and 20% , respectively, of the total planetary magnetic flux (Cowley et al., 2004b; Cowley et al., 2005b), as will be discussed further below. If the plasma rotates on average at approximately half the planetary angular velocity throughout this region, then the above rotational voltage estimates will be

reduced by only ~5% and 10%, respectively, due to this effect. These considerations therefore produce only minor corrections to the above total rotational voltage values.

It is evident that these rotational voltages very greatly exceed the averaged Dungey-cycle flux transports discussed above. Even the estimated compression region Dungey-cycle voltages at Jupiter and Saturn are only ~1% of these values, or less, which may be taken to imply that the Dungey-cycle flows are quite negligible at these planets, except for the production of the extended magnetotail. By comparison, the rotational voltage at Earth computed on the same basis is $V_{ROT} \sim 90$ kV. The average 30 kV Dungey-cycle reconnection rate in this case is already 30% of the rotational voltage, while the typical rate of tail reconnection, when it occurs, is comparable or larger. We therefore see that the magnetospheres of Jupiter and Saturn are very similar to each other in this respect, but are very different to the magnetosphere of the Earth.

This conclusion on the negligible role of the Dungey-cycle flows at Jupiter and Saturn considerably overstates the case, however, since most of the rotating flux considered above closes in the quasi-dipolar inner regions of the magnetosphere where the fields are strongest. As indicated above, the flux circulating in the outer parts of these magnetospheres is generally a small fraction of the total, and also usually significantly sub-corotates relative to the planet, leading to greatly reduced rotational voltage values for these regions. It may still be the case, therefore, that the Dungey-cycle contributes significantly to the flux transport in the outer regions of these magnetospheres as shown in Fig. 2.3. To investigate this issue we will now make some estimates of the rotational flux transport specifically in the outer regions of Jupiter’s and Saturn’s magnetospheres, considering both the middle magnetosphere or ‘ring current’ regions where strong azimuthal currents are present, and the ‘outer magnetosphere’ layer adjacent to the magnetopause where the Vasyliunas-cycle and the Dungey-cycle return flow takes place, according to Fig. 6.1. We begin with Jupiter and first consider the rotational flow in the middle magnetosphere, which we take to extend across the region from where corotation breaks down at $\sim 20 R_J$ radial distance to the outer edge at $\sim 60 R_J$. Using the Khurana and Kivelson (1993) model of the equatorial magnetic field, the amount of magnetic flux threading this region is estimated to be ~ 160 GWb. The typical plasma angular velocity in this region based on Voyager and Galileo spacecraft data corresponds roughly to $k = 0.6$ (e.g. Kane et al., 1995; Krupp et al., 2001) such that from Eq. (6.3) we obtain an estimate of the rotational voltage in Jupiter’s middle magnetosphere (subscript ‘MM’) of

$V_{ROT\ MM} \sim 2.5$ MV (Table 6.1). This value is also in agreement with the theoretical model calculation by Nichols and Cowley (2005), which yields $V_{ROT\ MM} \sim 3$ MV across the same region. We can also estimate the rotational voltage across Jupiter’s outer magnetosphere layer, which extends from the outer edge of the middle magnetosphere to the magnetopause in the dayside sector of the magnetosphere (see Fig. 2.3). Since this flux does not complete a full rotation of the planet, such that Eq. (6.3) is not evidently appropriate, we instead estimate the voltage by integrating the motional electric field E_{OM} across the outer magnetosphere layer to obtain

$$V_{ROT\ OM} \approx E_{OM} L_{OM} \approx v_{OM} B_{OM} L_{OM}, \quad (6.4)$$

where v_{OM} is the velocity of the plasma, B_{OM} is the outer magnetosphere field strength, and L_{OM} is the width of the layer. Spacecraft observations show that the outer magnetosphere layer is $\sim 15 R_J$ wide adjacent to the dayside magnetopause, with a field strength of ~ 10 nT (e.g. Acuña et al., 1983). The velocity of the plasma in this region is typically $v_{OM} \sim 200 - 400$ km s⁻¹ (i.e. $k \sim 0.25 - 0.5$), possibly depending on the state of expansion of the magnetosphere (e.g. Kane et al., 1995; Krupp et al., 2001). From Eq. (6.4) we then find the voltage associated with the rotational flow in the outer magnetosphere is $V_{ROT\ OM} \sim 2 - 4$ MV (Table 6.1). It is evident from comparing the voltage values in Table 6.1 that rarefaction region Dungey-cycle voltages of $V_{DC} \sim 150$ kV are still small compared with these rotational voltages in both the middle and outer regions of the magnetosphere. However, compression region Dungey-cycle voltages of $V_{DC} \sim 1$ MV, although occurring only $\sim 10\%$ of the time, are directly comparable in magnitude with those of the rotational flow in both the middle and outer magnetosphere. When such voltages occur, possibly further augmented by the impulsive tail behaviour discussed above, the Dungey-cycle flows will contribute significantly to the flow in the outer regions of Jupiter’s magnetosphere.

Similarly for Saturn’s magnetosphere, we first examine the rotational flows in the ring current region, analogous to the middle magnetosphere at Jupiter. Pioneer-11 and Voyager observations show that this extends from an inner edge at $\sim 6-8 R_S$ out to distances of $\sim 16 R_S$ (Connerney et al., 1983; Bunce and Cowley, 2003; Cowley and Bunce, 2003c; Cowley et al., 2004b). Cowley et al. (2004b) used a magnetic field model based on Voyager data to show that the amount of magnetic flux threading the equatorial plane between these radial limits is $\sim 25-40$ GWb. Voyager data show that the typical plasma angular velocity in this region

corresponds to $k \sim 0.6$ (Richardson, 1986; Richardson and Sittler, 1990). From Eq. (6.3) we then find that the voltage associated with the rotational flow in Saturn’s ring current region is $V_{ROT RC} \sim 400 - 600$ kV (Table 6.1). For the outer magnetosphere, the layer between the outer edge of the ring current region and the magnetopause, we again use Eq. (6.4) with a width $L_{OM} \sim 6 R_S$ (e.g. Arridge et al., 2006), a field strength $B_{OM} \sim 5$ nT (e.g. Dougherty et al., 2005), and a flow speed of $v \sim 100$ km s⁻¹ corresponding to $k \sim 0.7$ (Richardson, 1986; Richardson and Sittler, 1990; Szego et al., 2005; Hartle et al., 2006). Equation (6.4) then yields an outer magnetosphere rotational voltage of $V_{ROT OM} \sim 180$ kV (Table 6.1). Comparing these values with those for the Dungey-cycle at Saturn given in Table 6.1 shows that, as at Jupiter, these rotational voltages are much larger than the rarefaction region Dungey-cycle voltages, estimated to be $V_{DC} \sim 25$ kV. However, the compression-region Dungey-cycle voltages of ~ 150 kV are again competitive, especially if augmented by impulsive tail behaviour, such that when these peak voltages are occurring, the Dungey-cycle flow will have a significant influence in the outer magnetosphere.

To take the argument a step further, we can compute the radial width of the layer that the Dungey-cycle ‘return’ flow contributes to the outer magnetosphere region adjacent to the dawn magnetopause, as depicted in Fig. 2.3. Following Eq. (6.4), the voltage across the layer is $V_{DC} \approx E_{OM} L_{DC}$ where E_{OM} is the electric field associated with the flow, and L_{DC} is the layer width perpendicular to the magnetopause. If the plasma flow velocity in the layer is v_{OM} , and the magnetic field strength adjacent to the magnetopause is B_{OM} , as before, this becomes $V_{DC} \approx v_{OM} B_{OM} L_{DC}$, such that

$$L_{DC} \approx \frac{V_{DC}}{v_{OM} B_{OM}} . \tag{6.5}$$

Writing the flow velocity in terms of the planetary angular velocity, we have $v_{OM} = k R_{MP} \Omega_P = \frac{2\pi k R_{MP}}{T_P}$, where R_{MP} is the magnetopause radius. Then Eq. (6.5) becomes

$$L_{DC} \approx \frac{V_{DC} T_P}{2\pi k R_{MP} B_{OM}} . \tag{6.6}$$

For rarefaction region conditions at Jupiter we use $R_{MP} \sim 90 R_J$ (Joy et al., 2002) in the pre-noon hours (e.g. ~ 09 LT), $k \sim 0.25$, $B_{OM} \sim 5$ nT, and $V_{DC} \sim 150$ kV (Table 6.1) to find $L_{DC} \sim 1 R_J$, representing a minor contribution under these conditions. During CIR- or CME-related solar wind compressions of the magnetosphere, when $R_{MP} \sim 60 R_J$, $k \sim 0.5$, $B_{OM} \sim 10$ nT, and $V_{DC} \sim 1$ MV, however, we find $L_{DC} \sim 4 R_J$, possibly augmented further if the tail reconnection is impulsive. This represents a more significant contribution to an outer magnetosphere layer of 10-15 R_J thickness under these conditions. Similarly, under rarefaction region conditions at Saturn we use $R_{MP} \sim 30 R_S$ in the pre-noon hours (Arridge et al., 2006), $k \sim 0.7$ (Richardson, 1986; Richardson and Sittler, 1990; Szego et al., 2005; Hartle et al., 2006), and $B_{OM} \sim 4$ nT (Dougherty et al., 2005), to obtain a layer width $L_{DC} \sim 0.5 R_S$ when $V_{DC} \sim 25$ kV. Under compression region Dungey-cycle conditions when $V_{DC} \sim 150$ kV we use $R_{MP} \sim 20 R_S$, $k \sim 0.7$, and $B_{OM} \sim 10$ nT to obtain $L_{DC} \sim 2 R_S$, which again may be augmented if tail reconnection is impulsive. As at Jupiter, the layer width under rarefaction region conditions at Saturn is small and essentially negligible, but under compression region conditions it becomes a significant contributor to the outer magnetosphere. We note that similar hot plasma layer widths adjacent to Saturn’s magnetopause have been estimated on the basis of auroral distributions, as described in Chapter 5 (and by Badman et al., 2006).

6.4 Identification of Dungey-cycle flows in the equatorial magnetosphere

The above discussion indicates that under conditions of peak Dungey-cycle tail reconnection rates associated with interplanetary CIR compressions or CMEs, equatorial ‘return’ flow layers of non-negligible width should exist adjacent to at least the pre-noon magnetopauses at Jupiter and Saturn. The layer may become thinned in the post-noon hours, however, if significant reconnection-related flux tube erosion is present at the dayside magnetopause, as indicated in the steady-state picture shown in Fig. 2.3. It is then of interest to consider how such layers may be identified, relative to outer magnetosphere flow layers associated with rotational dynamics and the Vasyliunas-cycle. Although not mentioned in the works cited above in which this model has previously been discussed (Cowley et al., 2003; 2004a,b), a key difference exists between these layers which could in principle allow their experimental identification. This concerns the differing sources of the hot plasma within these layers, which should result in a strongly different hot ion composition. Since the sub-corotational

middle magnetosphere region and Vasyliunas-cycle flows are driven specifically by internal sources combined with planetary rotation, the ion component of these plasmas will be determined by the nature of the internal sources gases. At Jupiter, therefore, this internal plasma will be dominated by sulphur and oxygen ions originating from Io (e.g. Bagenal, 1994; Radioti et al., 2005), while at Saturn it will be dominated by oxygen and hydrogen originating from the icy moons (e.g. Young et al., 2005). The hot plasma in the Dungey-cycle ‘return’ region, however, results from the heating of tail lobe plasma downstream from the tail reconnection site, and will accordingly consist principally of light ions, hydrogen and helium, originating either from the planet’s ionosphere via the polar wind (potentially containing singly-charged helium), or from the solar wind (containing doubly-charged helium).

We can also estimate the temperature of the heated ions within the outer magnetosphere layer. When reconnection occurs in the tail current sheet, either on closed field lines during the Vasyliunas-cycle, or on open field lines during the Dungey-cycle, the newly-closed reconnected field lines contract towards the planet. The ions on the contracting field lines are accelerated approximately to the Alfvén speed outside the current sheet, $V_A = B / \sqrt{\mu_0 m_i n_i}$, where B is the field strength outside the current sheet, and m_i and n_i are the ion mass and number density respectively (e.g. Cowley, 1984). If we assume that the plasma is composed of a single ion species (the dominant contributor to the mass density) then the energy of these ions following acceleration will be

$$W_i \approx \frac{1}{2} m_i V_A^2 \approx \frac{1}{2} \frac{B^2}{\mu_0 n_i}. \quad (6.7)$$

The energy per ion hence depends only on the field strength and number density, and not on the ion mass. Considering first the jovian tail current sheet at radial distances of $\sim 100 R_J$ where $B \sim 6$ nT and $n_i \sim 0.01 \text{ cm}^{-3}$ (e.g. Russell et al., 1998; Frank et al., 2002; Kronberg et al., 2005), we obtain from Eq. (6.7) an ion energy of ~ 10 keV. This value is in agreement with ion temperatures in the current sheet presented by Frank et al. (2002). As the flux tubes move from the tail towards the dayside they contract further and the plasma on the flux tubes is adiabatically compressed. Conservation of the bounce invariant, $W_{//} l^2$ implies that as the bounce path l of the plasma decreases (i.e. as the flux tube contracts), the parallel energy of the plasma particles $W_{//}$ must increase; this process is known as Fermi acceleration. The energies of the plasma ions may be augmented by factors of $\sim 2-3$ by Fermi acceleration, such

that we then expect the production of a hot-ion plasma with temperatures of a few tens of keV in the dayside outer magnetosphere, both in the Dungey-cycle and the Vasyliunas-cycle layers. Considering now Saturn’s magnetotail at a distance of a few tens of R_S from the planet, we take values of $B \sim 3$ nT and $n_i \sim 0.01$ cm⁻³ (Ness et al., 1981; Richardson, 1986) to obtain using Eq. (6.7) an ion energy of ~ 2 keV. Again, this energy may be augmented by factors of $\sim 2-3$ due to Fermi acceleration of the plasma as it rotates round to the dayside magnetosphere, such that we anticipate hot ion layers of ~ 5 keV energy in the dayside outer magnetosphere in this case.

Therefore, to the extent that cross-field diffusion does not ‘blur’ the ion composition, it should be possible to identify Dungey-cycle ‘return’ flows in the outer magnetospheres of Jupiter and Saturn, and to distinguish them from regions dominated by the dynamics associated with the transport of plasma from internal sources, by examination of the dominant ion species at energies from a few keV to a few tens of keV. According to Fig. 2.3, the Dungey-cycle flows should form a hot-plasma layer adjacent to the magnetopause in the pre-noon hours if magnetopause reconnection is on-going, but will be more broadly distributed across the dayside region including the dusk sector if it is not. Similar comments apply to the layers of antisunward flow tailward of the reconnection sites in the centre plane of the tail. The tailward-flowing plasma sheet associated with the Dungey-cycle and the closure of open lobe flux on the dawn flank will consist primarily of light ions with \sim keV energies, while that associated with the tailward-propagating plasmoid formed by the Vasyliunas-cycle will consist principally of heavy ions with similar energies. As indicated above, however, Kivelson and Southwood (2005) have recently speculated that the nightside outflow in Jupiter’s magnetotail is associated with sequential outflow events that involve episodes of plasmoid ejection and open flux closure on much smaller spatial scales than is envisaged in Fig. 2.3. In this case the Vasyliunas-cycle and Dungey-cycle ‘return’ flows may become inextricably interlinked, such that no separate flow components with individual ion composition signatures may occur.

With regard to observations, we note that no directly relevant data concerning the composition of ions at energies of a few keV to a few tens of keV per ion have yet been published for the outer magnetosphere regions of either Jupiter or Saturn. This study therefore sets out the groundwork for future experimental tests of the ideas on magnetospheric structure and dynamics at these giant planets, outlined in Fig. 2.3. Unfortunately it appears

unlikely that definitive information can be derived for Jupiter’s outer magnetosphere from existing data from the Galileo orbiter. The reader is referred to publications by e.g. Frank et al. (2002) and Frank and Paterson (2004) for discussion of the limitations in ion mass resolution of the Galileo instrumentation in the above energy range. Mass-resolved ion data is available from Galileo, but at energies of typically hundreds of keV per ion (e.g. Radioti et al., 2005), corresponding to the high-energy tail of the thermal populations of central interest here. The anisotropies of these energetic ions have been employed to study the flows in Jupiter’s magnetosphere (e.g. Krupp et al., 2001; Woch et al., 2004), and have been used to identify flow bursts in the jovian tail attributed to mass-release and the Vasyliunas-cycle (Woch et al., 1999; Kronberg et al., 2005). At Saturn, hot plasma injections from the magnetotail have been observed by Cassini energetic neutral atom imaging data by Mitchell et al. (2005), and have been attributed to tail reconnection similar to substorms at Earth. These data include supra-thermal fluxes of mass-resolved hydrogen and oxygen at energies from several tens to a few hundred keV, again above the thermal ion energy range estimated here. Mass-resolved ion data at thermal energies should also become available from the Cassini plasma spectrometer (Young et al., 2004), but these observations may be difficult at the thermal plasma densities envisaged here (few times 0.01 cm^{-3}). Nevertheless we hope that the theoretical discussion given here concerning the physical significance of such observations will provide impetus for detailed future studies of such data.

6.5 Summary

In this study we have considered the contribution of the solar wind-driven Dungey-cycle to flux transport in the closed field regions of Jupiter’s and Saturn’s magnetospheres. Our estimates of the Dungey-cycle voltage in these systems have been derived from recent studies based on spacecraft measurements of the interplanetary medium near the orbits of these planets, combined with an empirical formula for the magnetopause reconnection rate validated at Earth. These values have then been compared with the voltages associated with the flows driven by planetary rotation. While the traditional comparison with the voltage associated with the rotational transport of the total planetary magnetic flux indicates that Dungey-cycle flows are negligible in these systems, being at most $\sim 1\%$ of the rotational transport, here we point out that most of this rotational transport takes place in the innermost part of the system where the fields are strongest. If instead we consider only the rotational flows associated with the middle and outer regions of these magnetospheres, we find that

while they are still more than an order of magnitude larger than the averaged Dungey-cycle voltages, and those occurring during solar wind rarefaction regions, they are of the same order as the typical Dungey-cycle voltages occurring in these systems during CIR compression regions and CMEs, namely ~ 1 MV at Jupiter and ~ 150 kV at Saturn. Under such conditions, therefore, the Dungey-cycle contributes a significant transport of magnetic flux within the outer parts of the closed field regions of these magnetospheres. Specifically, the width of the Dungey-cycle ‘return’ flow layer inside the pre-noon dayside magnetopause is then estimated to be typically $\sim 4 R_J$ in Jupiter’s magnetosphere and $\sim 2 R_S$ in Saturn’s magnetosphere, occurring $\sim 10\%$ of the time, compared with about one planetary radius or less during rarefaction regions. Thicker layers may occur if the tail reconnection is impulsive, but then lasting for correspondingly shorter intervals of time.

We also suggest that it may be possible to experimentally identify such layers inside these magnetospheres through the hot ion composition, provided the ‘blurring’ effect of cross-field particle diffusion is not too strong. While regions driven by planetary rotation should be dominated by heavy-ion plasmas originating from internal moon sources, the Dungey-cycle layers should principally contain hot light ions originating from either the planet’s ionosphere or the solar wind. Estimates of the typical ion temperatures at Jupiter are ~ 10 keV in the tail and ~ 20 - 30 keV in the dayside outer magnetosphere, while for Saturn the energies are ~ 2 keV in the tail and ~ 5 keV in the dayside outer magnetosphere.

Chapter 7

Relationship of solar wind compressions and the phasing and intensity of Saturn kilometric radiation

7.1 Introduction

In 1980 the Voyager spacecraft made the first detections of radiation from Saturn at kilometric wavelengths (Kaiser et al., 1980). As discussed in Chapter 2, section 2.6, these early measurements revealed two features of the so-called Saturn Kilometric Radiation (SKR) emissions. Firstly, the emission was pulsed at a period close to the rotation period of the planet, and secondly, the SKR power was positively correlated with the solar wind dynamic pressure (Desch and Kaiser, 1981a; Desch, 1982; Desch and Rucker, 1983). These studies did not reveal, however, how these two features are interrelated. More recent case studies using Cassini data have suggested that a solar wind corotating interaction region (CIR) compression can cause both intensification and ‘dropout’ (i.e. no detection) of the modulated SKR emissions (e.g. Bunce et al., 2005b; Jackman et al., 2005; Mitchell et al., 2005). The aim of this chapter is to present a preliminary survey of Cassini data from the magnetometer (MAG) (Dougherty et al., 2004) and Radio and Plasma Wave Science (RPWS) investigation (Gurnett et al., 2004) to investigate the interaction of compressions in the solar wind with the intensity and pulsing of the SKR emission. For example, we are looking for intensifications of the SKR power following arrival of a solar wind compression, any subsequent ‘dropout’ in the emission detected by Cassini, the phasing of the emission peaks during the compression event, and the relative phasing and intensity of the emission peaks before and after. To do this we analyse Cassini data during its approach to Saturn (October 2003 until June 2004) and its first extended orbit following Saturn orbit insertion (SOI) (July – October 2004). These are intervals when Cassini was measuring both the interplanetary conditions upstream of Saturn and SKR emissions from Saturn. The next section describes the Cassini data employed in this study, and following sections detail a selection of the events identified and the results of their analysis. Finally, some general conclusions are drawn about the effects of solar wind compressions on the power and modulation of the detected SKR.

7.2 Cassini measurements of SKR emissions and interplanetary magnetic field strength

The Cassini data used in this study are from late 2003 (day 344) until Cassini entered Saturn's magnetosphere on day 179 of 2004, and then days 195-298 of 2004 when Cassini had exited Saturn's magnetosphere back into the upstream solar wind. Due to the frozen-in nature of the solar wind flow, the interplanetary magnetic field magnitude measured by Cassini MAG can be used as a proxy for the solar wind dynamic pressure, as it was in Chapter 4. A compression region in the solar wind will be observed as an increase in field magnitude. As heliospheric current sheet crossings usually occur within compression regions as part of corotating interaction regions in the solar wind, a reversal in the sense of the B_T interplanetary field component (RTN coordinates) can also be used to identify a compression event. These data were searched for CIR compression events where there was good data coverage of the interval and the few surrounding days. Eleven such events were identified, three of which will be presented as examples below.

The SKR data is presented in two forms in this study to help identify the features within it. The first is a colour-coded electric field spectrogram from the Cassini RPWS instrument, which shows the power in each frequency channel in the range 5 kHz to 2 MHz, encompassing the SKR peak frequency range of 100-300 kHz. These data are at 1 min resolution. The SKR emitted power integrated over this peak frequency band is also shown. The power data are averages over a time interval of approximately one twentieth of the radio rotation period. It is well-established that the SKR period is not constant but drifting slowly over time (e.g. Galopeau and Lecacheux, 2000; Gurnett et al., 2005), therefore we use two nominal SKR periods derived from Cassini data in this analysis. The pre-SOI data uses the corresponding 'pre-arrival' period of 10.7625 h (Gurnett et al., 2005), such that the data are 0.538125 h averages. The post-SOI data uses the post-arrival SKR period of 10.7811 h (Kurth et al., 2005) i.e. the power data are 0.539056 h averages. In late 2003 – 2004 Saturn was experiencing northern hemisphere winter so the southern hemisphere was tilted significantly towards the Sun. Most of the SKR emissions detected by Cassini, which was approaching close to the ecliptic plane, therefore originated in the southern hemisphere i.e. were left-hand (LH) polarized. The RH emissions at Cassini are very weak in comparison so the LH power was used as an approximation for the total SKR power seen by Cassini.

7.3 Drifting period of SKR emissions

One of the purposes of this study is to determine whether solar wind compressions disrupt or shift the timing of the pulsing of the SKR peaks, therefore the times of the expected pulses based on their regular long-term behaviour must be known for comparison with those observed. Kurth et al. (2007) derived an expression for the variation of SKR phase relative to a fixed period ($T_0 = 0.4497$ d) by fitting a third order polynomial to Cassini measurements of the timing of the SKR peaks over the interval from 1 January 2004 to 28 August 2006. This phase drift is a function of time t in days since 1 January 2004, given by

$$\Delta\Phi_{SKR}(t) = C_1 + C_2 t + C_3 t^2 + C_4 t^3, \quad (7.1)$$

where $C_1 = 87.77 (\pm 10.1) \text{ deg}$, $C_2 = -2.527 (\pm 9.05 \times 10^{-2} \text{ deg d}^{-1})$, $C_3 = 3.041 \times 10^{-3} (\pm 2.17 \times 10^{-4}) \text{ deg d}^{-2}$ and $C_4 = -7.913 \times 10^{-7} (\pm 1.47 \times 10^{-7}) \text{ deg d}^{-3}$. This phase drift $\Delta\Phi_{SKR}$ is subtracted from the arbitrary fixed phase to give the phase of the SKR at any time:

$$\Phi_{SKR}(t) = \frac{360}{T_0} \times t - \Delta\Phi_{SKR}(t). \quad (7.2)$$

The drifting SKR period T_{SKR} is then given by:

$$T_{SKR}(t) = \frac{360}{d\Phi_{SKR}/dt} = \frac{360}{\left(\frac{360}{T_0} - (C_2 + 2C_3 t + 3C_4 t^2)\right)}. \quad (7.3)$$

These functions are defined such that when $\Phi_{SKR}(t) = 360n$, where n is an integer, there should be a peak in the SKR emission. To locate the times of the expected SKR peaks we therefore set Eqn. (7.2) equal to $360n$, incorporating Eqn. (7.1), and solve for successive n to find a set of times t . The errors in the constants C_1 , C_2 , etc. given above define the accuracy of the Kurth et al. polynomial fit to the measured SKR peaks, which corresponds to a maximum ‘error’ in the SKR period of ± 25 s over the intervals studied here. However, the spread in the measured timings of the SKR peaks is actually significantly larger than this, as

shown by Kurth et al. (2007) (see their Figure 2), and is partially attributed to the broadness of the peaks of the SKR emission. In this study we use the ‘expected’ times of the peaks in SKR emission (t') as a guide to highlight any change in the pulsing of the SKR associated with solar wind compression events, whilst acknowledging that there is intrinsic uncertainty in these values themselves. In the next section examples of solar wind compression events and the corresponding SKR detections are presented and discussed.

7.4 Examples of solar wind compression events and the corresponding SKR detections

The sections below detail three solar wind compression events from 2004 and the varying responses in the SKR emissions detected by Cassini.

7.4.1 Event 1: 2004 DOY 49 – 55

The Cassini data acquired over days 49-55 (18-24 February) of 2004, when Cassini was at a radial distance of more than $1000 R_S$, are shown in Figure 7.1. The top panel shows the emitted SKR power in Watts per steradian, over the frequency range of 100-300 kHz. The power is normalised to solid angle (steradian) to account for the distance-dependence ($1/r^2$) of the power, as Cassini’s distance from Saturn varies greatly over the interval of interest. The crosses toward the top of the panel mark the timings of the expected SKR peaks according to the Kurth et al. (2007) algorithm described above. The middle panel of Figure 7.1 is an electric field spectrogram, where the relative powers are colour-coded according to the colour bar on the right hand side of the figure, and plotted as a function of frequency and time. The white crosses in the upper part of this panel again show the expected timings of the SKR peaks as in the upper panel. The bottom panel shows the IMF magnitude in nT, colour-coded according to the sense of IMF B_T , where blue represents $B_T < 0$ and red represents $B_T > 0$, as indicated at the right hand side of the panel. The time axis is labelled at intervals of days, with Cassini’s radial distance from Saturn also labelled in units of Saturn radii (here $1 R_S = 60\,268$ km). The time taken for the solar wind to propagate from the spacecraft to the planet, assuming purely radial motion and using a nominal solar wind speed of 500 km s^{-1} , is given at the top of the figure. The actual propagation delay is very uncertain (to many hours) due to non-radial propagation of the solar wind and variations in the flow speed (Crary et al., 2005). In the example shown in Figure 7.1 the radial propagation delay is nominally ~ 15 h,

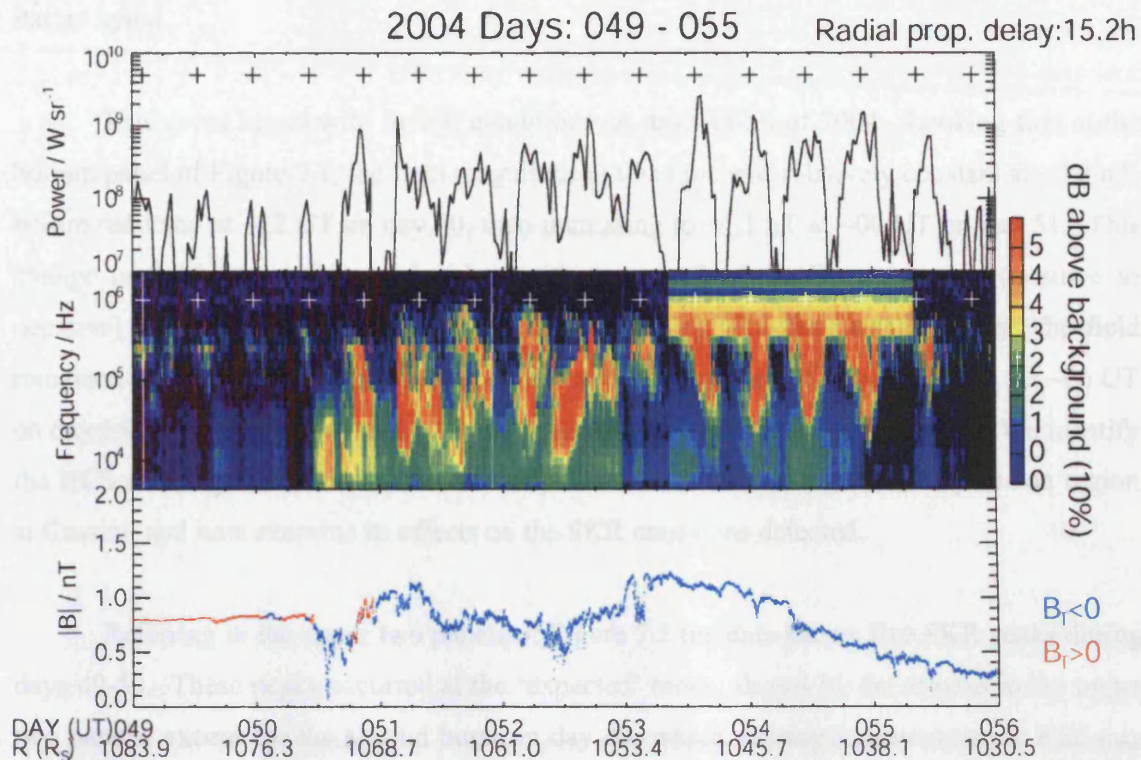


Figure 7.1 SKR and IMF data from event 1 (days 49-55 of 2004). The top panel shows 0.538125 h averages of the emitted power of the SKR integrated over 100-300 kHz. The crosses toward the top of the panel mark the expected times of the SKR peaks given by Kurth et al. (2007), as described in the text. The middle panel shows the electric field power as a function of frequency and time, colour-coded according to the colour bar at the right hand side of the figure. The white crosses on this panel again represent the expected peaks of SKR emission, as in the top panel. The bottom panel is a plot of the interplanetary magnetic field strength in nT, colour coded by the sense of the RTN B_T component as indicated at the right hand side of the panel. The time axis of these plots is marked in units of days, with subdivisions every 6 h. Also marked is the spacecraft range from Saturn in units of Saturn radii (where $1 R_S = 60\,268$ km). At the top of the plot, an estimate of the solar wind propagation delay is marked, estimated assuming purely radial propagation and a constant solar wind speed of 500 km s^{-1} .

varying by ± 0.5 h over the interval, reducing to ~ 11 h for propagation aligned along the Parker spiral.

This event began with ‘quiet’ conditions on days 49-50 of 2004. Looking first at the bottom panel of Figure 7.1, the field magnitude at this time was relatively constant at ~ 0.8 nT, before reducing at ~ 12 UT on day 50, then increasing to ~ 1.1 nT at ~ 06 UT on day 51. This change in field strength was coincident with a reversal of the B_T component (positive to negative) indicating a heliospheric current sheet crossing. For the next three days the field remained disturbed, fluctuating on short timescales between ~ 0.5 nT and ~ 1.2 nT. At ~ 06 UT on day 54 the field began a steady decline, reaching ~ 0.3 nT at the end of day 55. We identify the HCS crossing and disturbed field on day 50 as the arrival of a minor compression region at Cassini, and now examine its effects on the SKR emissions detected.

Referring to the upper two panels of Figure 7.1 the data shows five SKR peaks during days 49-50. These peaks occurred at the ‘expected’ times, shown by the crosses in the upper two panels, except for the second burst on day 49, which occurred approximately half way between two expected peaks. The power of each of these five peaks was $\sim 10^8$ W sr⁻¹. A more intense burst of SKR emission was detected at the next ‘expected’ time (~ 21 UT on day 50), reaching a maximum power of $\sim 10^9$ W sr⁻¹, i.e. an order of magnitude larger than the preceding bursts. This was followed by another burst, which peaked just ~ 8 h later, i.e. sooner than the next expected time of a peak marked by the cross. The timing of this peak was ~ 18 h after the IMF magnitude decreased, indicating the start of the field disturbance. This SKR burst could mark the arrival of the disturbed field at Saturn, as it occurred in addition to the regular pulsed emissions. However, the increased power of the previous burst suggests that perhaps the field disturbance arrived at this earlier time. It is not possible to confirm which of these is the initial response of the SKR however, because there was no sharp shock front in the field data to identify the start of the compression, and there are significant uncertainties in the estimated propagation delay, as described above. Following these bursts over the next four days there were several broad, intense SKR bursts, all at powers of $\sim 10^9$ W sr⁻¹. The enhanced ‘background’ emission observed in the high frequency channels of the spectrogram (middle panel) on days 53-55 is due to an instrument mode change, and has been accounted for when deriving the power values shown in the top panel. The final SKR burst shown on day 55, when the field strength was declining, had a lower power of $\sim 10^8$ W sr⁻¹, similar to that of the bursts before the field disturbance.

7.4.2 Event 2: 2004 DOY 133-139

The next event presented was from days 133-139 (12-18 May) 2004, when Cassini was at a radial distance of $\sim 400 R_S$. The data from this interval are shown in Figure 7.2 in the same format as Figure 7.1. At this distance between Cassini and Saturn the estimated radial propagation delay was ~ 5 h, varying by ± 0.4 h over the interval. The magnetic field data clearly show a CIR forward shock at ~ 12 UT on day 134, when the field strength increased from below 0.2 nT to ~ 0.5 nT. The field remained elevated and disturbed for several days, only returning to ‘quiet’ conditions on day 144, when the SKR had already returned to its pre-compression power and periodicity. The SKR data plotted in the top two panels shows four distinct periodic bursts of SKR during the low field strength interval on days 133-134 (allowing for the ~ 5 h solar wind propagation delay), each peaking at $3 - 5 \times 10^8 \text{ W sr}^{-1}$. These bursts are at the expected timings marked by the crosses, but a few lower power spikes also occurred in addition, e.g. ~ 10 UT on day 134. At ~ 21 UT on day 134 an intense SKR burst was detected, peaking at $\sim 10^9 \text{ W sr}^{-1}$. This was ~ 3 h after the solar wind shock was expected to arrive at Saturn by employing the ~ 5 h propagation delay from the spacecraft to the planet, and occurred in between the timings of the expected SKR peaks. A few hours after this initial intensification, and centred at the time of an expected SKR peak, a double-peaked broad burst was detected with a reduced power of $\sim 2 \times 10^8 \text{ W sr}^{-1}$. For the next two days several bursts of SKR were detected but at relatively low powers (between $\sim 2 \times 10^7$ and $\sim 10^8 \text{ W sr}^{-1}$). Some of these bursts occurred at the expected timings but there were also peaks in between these times e.g. ~ 08 UT on day 136. During days 137 to 138 the SKR emission was intensified again, with a particularly broad and powerful burst centred on ~ 12 UT on day 137, with a maximum power of $\sim 6 \times 10^8 \text{ W sr}^{-1}$. The intensity of the SKR bursts then decreased gradually for the rest of the interval to levels of $\sim 10^8 \text{ W sr}^{-1}$. These emission bursts were again occurring at the expected timings, but with other lower power peaks in between.

7.4.3 Event 3: 2004 DOY 206-219

The final interval presented here included days 206-219 (24 July – 6 August) of 2004 after SOI when Cassini was travelling away from Saturn on the dawn dayside, at distances of ~ 115 - $140 R_S$. However, Cassini was travelling close to the dawn meridian so the displacement in the Sun-planet radial direction was very small, and hence the radial propagation delay was very small (a few minutes). At the start of the interval, shown on

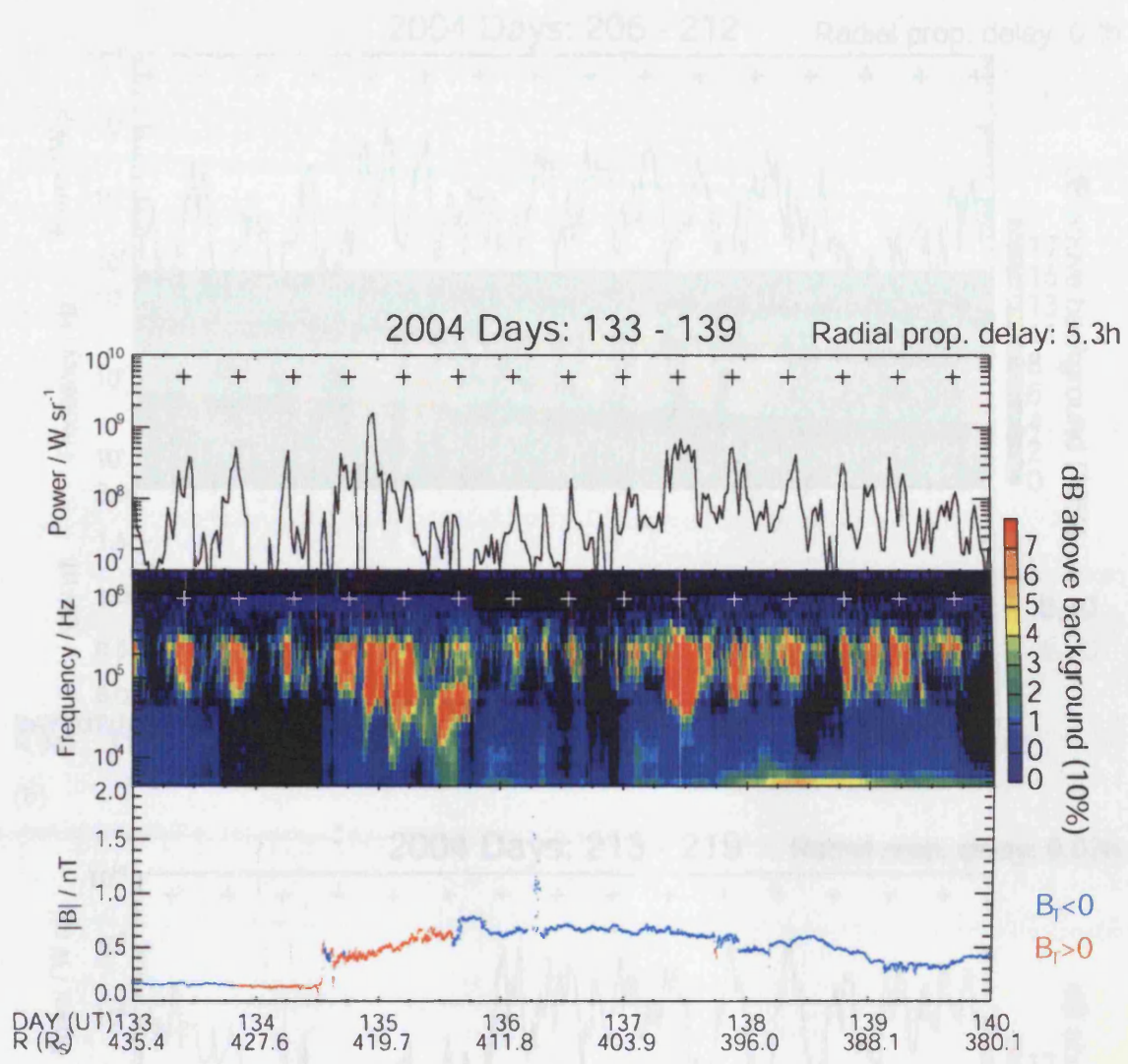
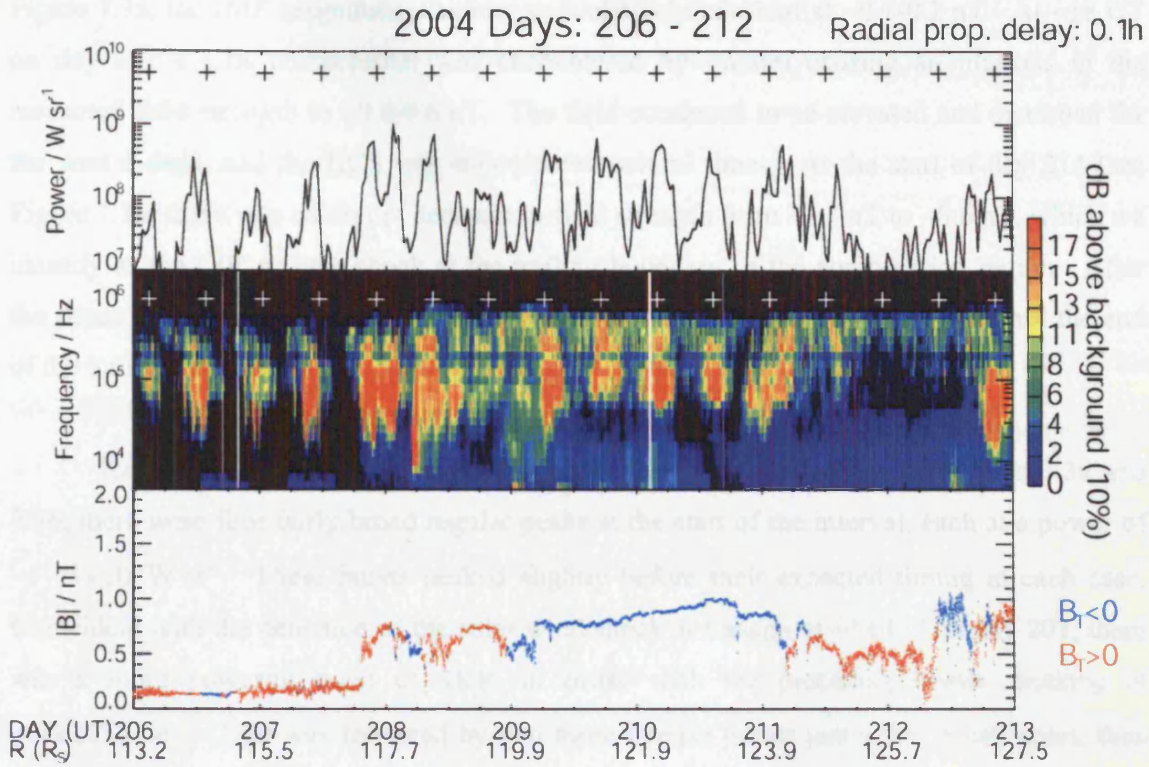


Figure 7.2 SKR and IMF data from event 2 (days 133-139 of 2004), in the same format as Figure 7.1

(a)



(b)

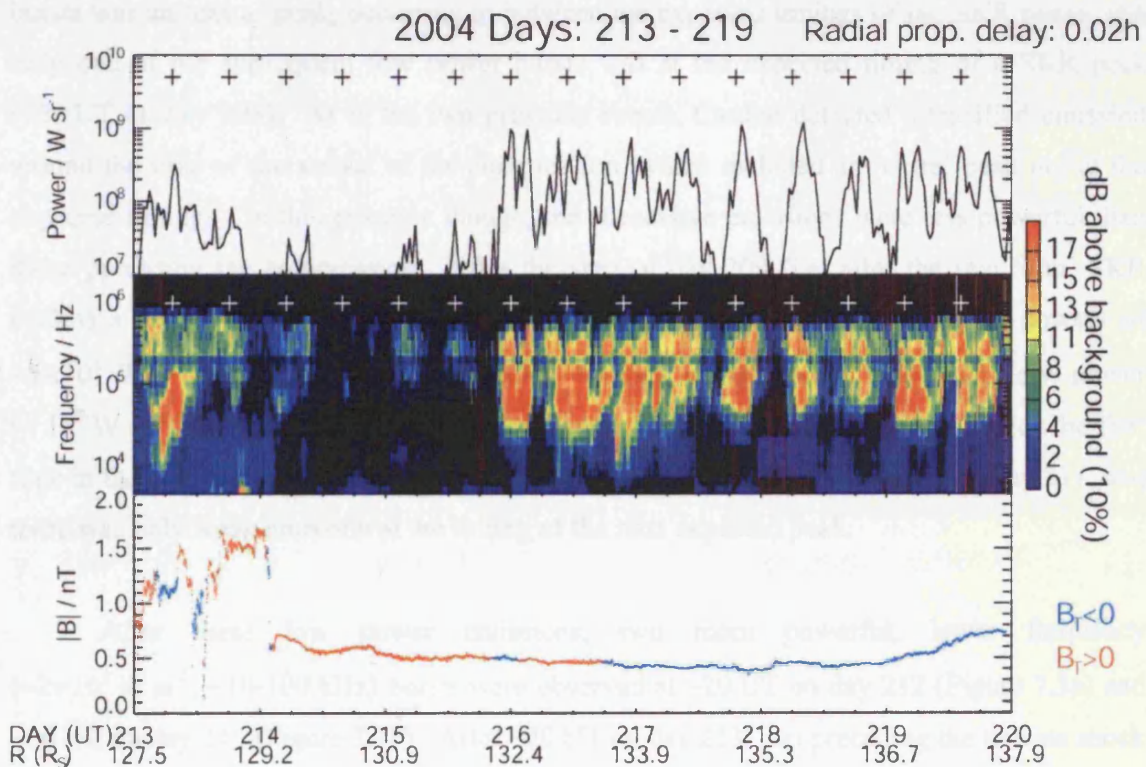


Figure 7.3 SKR and IMF data from event 3: (a) days 206-212, and (b) days 213-219 of 2004, in the same format as Figure 7.1. The SKR power data in the top panel are 0.539056 h averages.

Figure 7.3a, the IMF magnitude was low and relatively constant at $\sim 0.1\text{-}0.2$ nT. At ~ 18 UT on day 207 a CIR compression was encountered by Cassini causing an increase in the measured field strength to $\sim 0.6\text{-}0.8$ nT. The field continued to be elevated and disturbed for the next 6 days, and the HCS was encountered several times. At the start of day 214 (see Figure 7.3b) there was an abrupt decrease in field strength from ~ 1.7 nT to ~ 0.6 nT, which we identify as the CIR reverse shock at the trailing boundary of the compression region. After the shock the field remained approximately constant at ~ 0.5 nT for over 5 days, until the end of the interval shown.

Examining the SKR emissions plotted in the upper two panels of Figures 7.3a and 7.3b, there were four fairly broad regular peaks at the start of the interval, each at a power of $\sim 1 - 3 \times 10^8 \text{ W sr}^{-1}$. These bursts peaked slightly before their expected timing in each case. Coincident with the detection of the solar wind shock at Cassini at ~ 18 UT on day 207, there was a more powerful burst of SKR, in phase with the preceding bursts, peaking at $\sim 6 \times 10^8 \text{ W sr}^{-1}$. This was followed by two more intense bursts just a few hours apart, then several low power ($\sim 10^8 \text{ W sr}^{-1}$) bursts over the next two SKR cycles. The first of the intense bursts was an ‘extra’ peak, occurring in between the expected timings of the SKR peaks, and only one of the subsequent low power bursts was at the expected timing of a SKR peak (~ 20 UT on day 208). As in the two previous events, Cassini detected intensified emission around the time of the arrival of the compression, which included an ‘extra’ peak not at the expected timings. In this example though, the successive emissions were less powerful than those preceding the compression. After the start of day 209 (i.e. after the two ‘dim’ SKR cycles) a series of six broad powerful bursts were detected, each peaking at powers of $\sim 5 \times 10^8 \text{ W sr}^{-1}$ and close to the expected timings of the peaks. Further low power ($< 10^8 \text{ W sr}^{-1}$) emissions were then detected late on day 211 until mid day 212. For the first time in the events shown, the SKR appeared to miss a pulse close to midnight on day 211, and there was only weak emission at the timing of the next expected peak.

After these low power emissions, two more powerful, lower frequency ($\sim 2 \times 10^8 \text{ W sr}^{-1}$, $\sim 10\text{-}100$ kHz) bursts were observed at ~ 20 UT on day 212 (Figure 7.3a) and ~ 06 UT on day 213 (Figure 7.3b). After ~ 20 UT on day 213, just preceding the reverse shock encounter in the solar wind, the SKR emission virtually disappeared. At this time the solar wind velocity would be increased, but the dynamic pressure decreased, such that the magnetosphere expanded. Out of the next four SKR peaks expected, only three very low

power ($< 10^8 \text{ W sr}^{-1}$) bursts were detected. The SKR again missed a pulse at ~ 16 UT on day 214, ~ 12 h after the reverse shock. Powerful SKR emissions reappeared at the end of day 215, with no obvious IMF trigger, and continued, often peaking at powers in excess of 10^9 W sr^{-1} , until the end of the interval shown on day 219. These emissions did peak at the expected times, but there were also many extra peaks of similar powers in between.

7.5 Discussion and Conclusions

It is evident from the descriptions above that a variety of features in the SKR data are detected following a solar wind disturbance. We now attempt to identify any common features from all the events included in this study, and suggest possible explanations for these observations. One persistent feature in the SKR data was the initial high-power burst, usually peaking at $\sim 10^9 \text{ W sr}^{-1}$, which occurred around the time of the arrival of the solar wind compression at the magnetosphere. (The exact timing is approximate due to uncertainties in the propagation delay.) The timing of this burst is usually out of phase with the expected times of the SKR emission peaks to such an extent that it cannot be attributed to the intrinsic deviation of the bursts around the Kurth et al. fit. After the consistent appearance of the initial powerful SKR burst, however, the behaviour of the SKR varied between events. In three of the eleven events identified, the SKR pulses continued at high powers for several days (e.g. days 49-54, shown in Figure 7.1). In another event, no SKR emission is detected by Cassini for more than 12 hours shortly after the disturbance. This is similar to the observations following the reverse shock on day 214 shown in Figure 7.3b, when very low levels of emission were detected for ~ 30 h. Most commonly in the events studied, periods of both intense and dim SKR bursts (relative to those preceding the solar wind disturbance) are detected after solar wind compressions (e.g. days 133-139 shown in Figure 7.2). In general, this study confirms that the emitted SKR power initially increases during solar wind compression regions. After this initial intensification, however, the behaviour is variable: sometimes intensified and sometimes dimmed, and therefore warrants more detailed investigation in the future.

Now considering the pulsing of the SKR bursts, we note that overall the SKR continues to pulse at the expected times, with respect to the Kurth et al. drifting period, during and after the solar wind disturbances. There are two exceptions to this: firstly, the initial powerful SKR burst described above does not always fall coincident with a regular pulse of the SKR e.g. on day 51, shown in Figure 7.1. Also, there are the two occasions mentioned

above where the SKR emission virtually disappears from Cassini's measurements. In these cases, at least one SKR 'beat' is skipped, but when the SKR pulses return, they are in phase with the Kurth et al. pulsing (see Figure 7.3b). In addition to the regular pulsing of the SKR, there are numerous 'extra' bursts at the same frequencies, of lesser or equal power, e.g. days 208-212 in Figure 7.3a.

As there is as yet no complete theory on how SKR is generated and controlled we do not attempt in this preliminary study to give detailed physical reasons for the observed variations in the emitted power and phasing of the SKR. We can, however, suggest how our observations may relate to those presented in other studies. For example, Kurth et al. (2005) noted that intense SKR bursts were coincident with enhanced UV auroral emissions during the January 2004 HST imaging campaign. As discussed in Chapter 4, Cowley et al. (2005a) attribute these enhanced auroral emissions to large reconnection events in the magnetotail, which accelerate large volumes of plasma around the dawn side of the planet, and cause enhanced precipitation into the ionosphere. Compression-induced tail reconnection is then a possible explanation for the intense bursts of SKR observed shortly after the arrival of a solar wind compression at Saturn's magnetosphere. Similarly, any broad 'extra' peaks of SKR over the next few days could be associated with further reconnection events, as described by e.g. Bunce et al. (2005b), Mitchell et al. (2005), Jackman et al. (2007). This is analogous to the behaviour of terrestrial auroral kilometric radiation, which is enhanced during reconnection events in the Earth's magnetotail (e.g. Gurnett, 1974). There is also the suggestion that the fast solar wind flow associated with the CIR compression regions could enhance Kelvin-Helmholtz waves at the magnetopause which are connected to the SKR source, thereby enhancing the SKR emissions as observed (e.g. Galopeau and Lecacheux, 2000; Cecconi and Zarka, 2005). This theory does not account for the dropout in SKR emissions detected following the reverse shock on day 214 (Figure 7.3b), when the solar wind velocity was increased. However, we note that the other interval when the SKR detections became very weak (24-30 January 2004, not shown here) has been discussed in depth by Kurth et al. (2005), who stated that although Cassini RPWS detected very little SKR emission, the Unified Radio and Plasma wave experiment onboard the Ulysses spacecraft did measure SKR at the expected time. They therefore attribute the lack of measurements by Cassini to a beaming effect. This may also explain the lack of detection of SKR after the reverse shock on day 214 (Figure 7.3b), when the magnetosphere is probably rapidly expanding.

To sum up our discussion of the SKR phasing, our analysis suggests that while the period of the SKR pulses is varying slowly over time (e.g. Galopeau and Lecacheux, 2000; Gurnett et al., 2005; Kurth et al., 2007), solar wind disturbances do not have a significant effect on the pulsing of the SKR. In the vast majority of our observations there continue to be SKR emission peaks at the expected times. While SKR bursts during the compression event are intensified or dimmed relative to those before the event, they usually continue to pulse at the same period as the preceding ones. The pulsing of the bursts is therefore the same before and after the compression events.

In conclusion, we have presented three examples of Cassini measurements of compressions in the solar wind, and the corresponding SKR emissions received at the spacecraft. We have examined the relative intensities of the SKR bursts before, during, and after the solar wind disturbances, and also compared the timings of the observed pulses with those predicted using the Kurth et al. (2007) drifting SKR period. The SKR response to the compressions is variable; however, we are able to draw some general conclusions from analysis of the 11 events included in this study. Firstly we confirm that there is an overall positive correlation between the solar wind dynamic pressure (approximated by the interplanetary magnetic field strength) and the emitted SKR power, as identified in Voyager data (Desch, 1982; Desch and Rucker, 1983). The timings of the initial SKR intensifications following the compressions are independent of the long-term phasing of the SKR bursts, but during the disturbed interval the SKR continues to pulse at the expected times. The intensity of the detected emissions during the disturbed intervals is variable: sometimes remaining intense for several days, sometimes dimming, and rarely disappearing. Our final conclusion is that, although variations in the SKR intensity are observed, the pulsing of the SKR bursts in general remains the same after the solar wind CIR compressions as it was before. This preliminary survey of the data has produced many further questions about SKR behaviour, which will be discussed in the next chapter.

Chapter 8

Summary and Future work

8.1 Summary

This thesis has explored the interaction of the solar wind with Saturn's magnetic and plasma environment, employing data from the Cassini spacecraft, and images of Saturn's UV aurora obtained by the Hubble Space Telescope (HST). A broad introduction to this research topic was given in Chapter 1, with a more detailed description of the Saturn system in Chapter 2. The instruments used to gather the data employed in the studies were described in Chapter 3 before the four science studies themselves were described in Chapters 4 to 7.

In Chapter 4 a sequence of auroral images from January 2004 was analysed to estimate the amount of open flux in Saturn's magnetosphere, using the poleward boundary of the aurora as a proxy for the open-closed field line boundary. The amount of open flux was found to range between $\sim 15 - 50$ GWb, such a large variation suggesting a significant interaction between the magnetosphere and the interplanetary medium. Cassini measurements of the upstream interplanetary conditions were then used to estimate the rate at which open flux was created at the dayside magnetopause over the imaging interval. Typical values were ~ 10 kV during the low field rarefaction regions, increasing to ~ 200 kV during the strong field compression regions. These values were then compared with the observed variations in open flux to deduce the rate at which open flux was closed in the magnetotail. Two types of flux closure event were identified: intermittent events during rarefaction regions when the average rates were $\sim 30-60$ kV, and strong events during compression regions when the average rates reached $\sim 100-200$ kV. These rates were finally used to interpret the observed forms of the aurora.

In order to fully relate the observed aurora to their driving magnetospheric processes, it is important to have basic knowledge such as where the aurorae are typically located. In the study described in Chapter 5 a selection of 22 HST images of Saturn's southern aurora, including those used in the study described above, was analysed to determine the median location and width of the auroral oval. On the dayside the poleward

and equatorward boundaries of the oval were found to lie at $\sim 14^\circ$ and $\sim 16^\circ$ co-latitude, respectively, with a median width of $\sim 2^\circ$. These median values vary little with local time although the poleward boundary moves to smaller co-latitudes around noon ($\sim 12.5^\circ$), such that the oval is wider here ($\sim 3.5^\circ$) than at dawn or dusk ($\sim 1.5^\circ$). This study also revealed the wide variability of the location of the auroral oval: the poleward boundary is found to lie between $\sim 2^\circ$ and $\sim 20^\circ$ co-latitude, and the equatorward boundary between 6° and 23° . Comparison with Voyager plasma angular velocity data mapped magnetically from the equatorial magnetosphere into the southern ionosphere indicated that the dayside aurora lie poleward of the main upward-directed field-aligned current region associated with corotation enforcement, which maps to $\sim 20^\circ$ - 24° co-latitude, while agreeing reasonably with the position of the open-closed field line boundary based on estimates of the open flux in Saturn's tail, located between $\sim 11^\circ$ and $\sim 15^\circ$. In this case, the variability in location can be understood in terms of changes in the open flux present in the system, validating the use of the poleward boundary of the aurora as a proxy for the open-closed field line boundary in Chapter 4. Referring again to the observed auroral forms, it is suggested that the broad (few degrees) diffuse auroral emissions and sub-corotating auroral patches observed in the dayside sector at Saturn result from precipitation from hot plasma sub-corotating in the outer magnetosphere in a layer $\sim 4 R_S$ wide adjacent to the magnetopause, probably having been injected either by Dungey-cycle or Vasyliunas-cycle dynamics on the nightside.

The origin and composition of this hot plasma layer were discussed further in Chapter 6. This study considered the contribution of the solar wind-driven Dungey-cycle to flux transport in both Saturn's and Jupiter's magnetospheres, the associated voltages being based on estimates of the magnetopause reconnection rates recently derived from observations of the interplanetary medium in the vicinity of the corresponding planetary orbits. At Saturn, the reconnection voltages were estimated to be ~ 25 kV during several-day weak-field rarefaction regions, increasing to ~ 150 kV during few-day strong-field compression regions, similar to those derived in Chapter 4. The corresponding values at Jupiter were ~ 150 kV for rarefaction regions, increasing to ~ 1 MV for compressions. These values were compared with the voltages associated with the flows driven by planetary rotation. Estimates of the rotational flux transport in the 'middle' and 'outer' magnetosphere regions are shown to yield voltages of several hundred kV and several MV at Saturn and Jupiter respectively, i.e. of the same order as the estimated peak Dungey-cycle voltages. It was concluded that under such circumstances the Dungey-cycle 'return'

flow will make a significant contribution to the flux transport in the outer magnetospheric regions. The ‘return’ Dungey-cycle flows are then expected to form layers inside the dawn and morning magnetopause which are $\sim 2 R_S$ wide at Saturn and $\sim 4 R_J$ wide at Jupiter. This Dungey-cycle layer, occurring during solar wind compression regions, is about half the width of the precipitating hot plasma layer derived from the median auroral morphology in Chapter 5, suggesting that on average the diffuse auroral features will be due to Vasylunas-cycle return flow, but will be enhanced during compression regions by an additional Dungey-cycle return flow population. In the absence of significant cross-field plasma diffusion, these layers will be characterized by the presence of hot light ions originating from either the planetary ionosphere or the solar wind, while the inner layers associated with the Vasylunas-cycle and middle magnetosphere transport will be dominated by hot heavy ions originating from internal moon/ring plasma sources. The temperature of these ions was estimated to be of the order of a few keV at Saturn and a few tens of keV at Jupiter, in both layers.

The final topic investigated in this thesis, and described in Chapter 7, is the effect of the solar wind on another of Saturn’s polar emissions: Saturn Kilometric Radiation (SKR). Voyager-era detections revealed that SKR emission pulses at a period close to Saturn’s rotation period, but this SKR period has subsequently been found to vary slowly over time. These early measurements also identified a positive correlation between the solar wind dynamic pressure and the emitted SKR power. This study investigated how these two features are interrelated, e.g. whether the intensified SKR emissions following a compression continue to pulse at the expected times. Compression regions in the solar wind were identified from Cassini measurements of the interplanetary magnetic field magnitude, as in Chapter 4, and the concurrent SKR data examined for variations in the timing and intensity of the emission peaks. This study confirmed that the emitted SKR power was positively correlated with the solar wind dynamic pressure. Following the initial intensified SKR burst, however, the powers of the emitted SKR peaks were variable; sometimes reduced and sometimes increased relative to those preceding the compression region. During the solar wind compression regions the timings of the observed SKR peaks were compared to those expected from a model of the slowly-varying SKR period. In most events studied, the SKR peaks continue to pulse at the expected times during the compression event. This study allowed some preliminary conclusions to be drawn about the behaviour of SKR during solar wind compressions. However, it has also raised many

questions for further study, as will now be described, along with other possible study topics for the future.

8.2 Future work

There are several obvious extensions to the work described in this thesis. The first of these is to extend the investigation of the solar wind and SKR relationship begun in Chapter 7. For example, it is of interest to determine why the SKR peaks after a solar wind compression are sometimes more powerful, and sometimes less powerful, than those preceding the compression. Further examination of the data could elucidate whether this is a beaming effect, i.e. dependent on the relative location of Cassini, or whether it is perhaps due to the ‘strength’ of the compression, or the state of expansion of the magnetosphere just before the compression arrives, for example. Also, when ‘extra’ bursts of SKR emission are observed, do these have any associated periodicity? Investigating these issues will give further insight into how the solar wind affects SKR emissions.

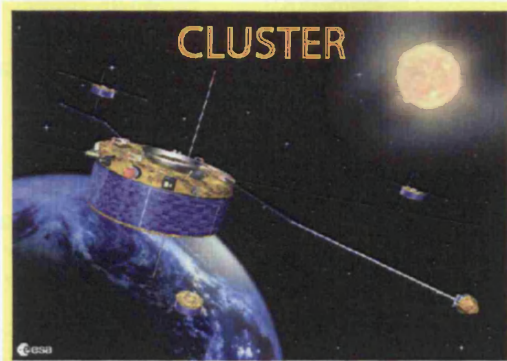
In this thesis, both UV and radio wave (SKR) auroral emissions have been discussed in relation to the solar wind conditions. However, the relationship between the two themselves has not been investigated. These emissions are believed to be generated by a common process, i.e. downward-moving electrons, therefore one might expect measurements of the emissions to show correspondences. The high-cadence HST auroral imaging campaign that took place in early 2007 while Cassini was in orbit around Saturn provides the ideal data set to look for these correspondences, and any additional influence from the solar wind. A similar study could also be carried out for Jupiter using the HST images of its aurora obtained during the same campaign, along with Earth-based measurements of jovian radio emissions.

In these studies of Saturn’s magnetospheric dynamics some ‘Earth-like’ behaviours have been discussed, such as the size of the polar cap bounded by the auroral oval varying according to the solar wind interaction, and some ‘Jupiter-like’, such as the rotationally-driven Vasyliunas-cycle flows. It is obvious, therefore, that much understanding of magnetospheric and auroral processes is built on knowledge gained from studies of other planets. It is important to continue to carry out these comparative studies to obtain thorough understanding of common and unique processes. One example of a suitable

investigation is to search for reconnection events in Saturn's magnetosphere, as have been identified at the Earth and Jupiter, not just looking for the return flows from the tail described in Chapter 6, but also looking for events at the dayside magnetopause. Cassini will remain in orbit around Saturn until 2010, continuing to provide data for these and many other exciting investigations.

Appendix

Quality, not quantity.



Size (each).....	2.9m diameter by 1.3m high
Mass (total).....	4800kg
No. of craft.....	4
No. of onboard instruments (each).....	11
No. of landers carried.....	0
Max distance from Earth.....	119×10^3 km
No. of failed launches.....	1
Lifetime.....	10 years



Size	4m wide by 6.7m high
Mass	5712 kg
No. of craft.....	1
No. of onboard instruments	12
No. of landers carried.....	1
Max distance from Earth.....	1.43×10^9 km
No. of failed launches.....	0
Lifetime.....	4 years

The contents of this page do not represent the views of the University of Leicester, ESA, NASA, or Paul Henderson.

References

- Acuña, M.H. and N.F. Ness: The magnetic field of Saturn – Pioneer 11 observations, *Science*, 207, 444-446, 1980.
- Acuña, M.H., J.E.P. Connerney, and N.F. Ness: Topology of Saturn's main magnetic field, *Nature*, 292, 721-724, 1981.
- Acuña, M.H., K.W. Behannon, and J.E.P. Connerney: Jupiter's magnetic field and magnetosphere, in *Physics of the Jovian Magnetosphere*, edited by A.J. Dessler, p. 1-50, Cambridge Univ. Press, Cambridge, U.K., 1983.
- Achilleos, N., C. Bertucci, C.T. Russell, G.B. Hospodarsky, A.M. Rymer, C.S. Arridge, M.E. Burton, M.K. Dougherty, S. Hendricks, E.J. Smith, B.T. Tsurutani: Orientation, location and velocity of Saturn's bow shock: Initial results from the Cassini spacecraft, *J. Geophys. Res.*, 111, doi:10.1029/2005JA011297, 2006.
- Arridge, C.S., N. Achilleos, M.K. Dougherty, K.K. Khurana, and C.T. Russell: Modeling the size and shape of Saturn's magnetopause with variable dynamic pressure, *J. Geophys. Res.*, 111, A11227, doi: 10.1029/2005JA011574, 2006.
- Arridge, C.S., C.T. Russell, K.K. Khurana, N. Achilleos, N. Andre, A.M. Rymer, M.K. Dougherty, and A.J. Coates: Mass of Saturn's magnetodisc: Cassini observations, *Geophys. Res. Lett.*, 34, doi:10.1029/2006GL028921, 2007.
- Badman, S.V., E.J. Bunce, J.T. Clarke, S.W.H. Cowley, J.-C. Gérard, D. Grodent, and S.E. Milan: Open flux estimates in Saturn's magnetosphere during the January 2004 Cassini-HST campaign, and implications for reconnection rates, *J. Geophys. Res.*, 110, A11216, doi: 10.1029/2005JA011240, 2005.
- Badman, S.V., S.W.H. Cowley, J.-C. Gérard, and D. Grodent: A statistical analysis of the location and width of Saturn's southern auroras, *Ann. Geophys.*, 24, 3533-3545, 2006.
- Bagenal, F.: Empirical model of the Io plasma torus: Voyager measurements, *J. Geophys. Res.*, 99, 11043-11062, 1994.

References

- Behannon, K.W., R.P. Lepping, and N.F. Ness: Structure and dynamics of Saturn's outer magnetosphere and boundary regions, *J. Geophys. Res.*, 88, 8791, 1983.
- Biermann, L.: Kometenschwerfe und solare korpuskularstrahlung, *Z. Astrophys.*, 29, 274, 1951.
- Boudouridis, A., E. Zesta, L.R. Lyons, P.C. Anderson, and D. Lummerzheim: Effect of solar wind pressure pulses on the size and strength of the auroral oval, *J. Geophys. Res.*, 108, 8012, doi: 10.1029/2002JA009373, 2003.
- Boudouridis, A., E. Zesta, L.R. Lyons, P.C. Anderson, and D. Lummerzheim: Magnetospheric reconnection driven by solar wind pressure fronts, *Ann. Geophys.*, 22, 1367, 2004.
- Broadfoot, A.L., B.R. Sandel, D.E. Shemansky, J.B. Holberg, G.R. Smith, D.F. Strobel, J.C. McConnell, S. Kumar, D.M. Hunten, S.K. Atreya, T.M. Donahue, H.W. Moos, J.L. Bertaux, J.E. Blamont, R.B. Pumphrey, and S. Linik: Extreme ultraviolet observations from Voyager 1 encounter with Saturn, *Science*, 212, 206, 1981.
- Bunce, E.J. and S.W.H. Cowley: A note on the ring current in Saturn's magnetosphere: Comparison of magnetic data obtained during the Pioneer-11 and Voyager-1 and -2 fly-bys, *Ann. Geophys.*, 21, 661–669, 2003.
- Bunce, E.J., S.W.H. Cowley, and S.E. Milan: Interplanetary magnetic field control of Saturn's polar cusp aurora, *Ann. Geophys.*, 23, 1405, 2005a.
- Bunce, E.J., S.W.H. Cowley, D.M. Wright, A.J. Coates, M.K. Dougherty, N. Krupp, W.S. Kurth, and A.M. Rymer: In-situ observations of a solar wind compression-induced hot plasma injection in Saturn's tail, *Geophys. Res. Lett.*, 32, L20S04, doi: 10.1029/2005GL022888, 2005b.
- Bunce, E.J., S.W.H. Cowley, C.M. Jackman, J.T. Clarke, F.J. Crary, and M.K. Dougherty: Cassini observations of the interplanetary medium upstream of Saturn and their relation to Hubble Space Telescope auroral data, *Adv. Space Res.*, 38, 806-814, 2006.

References

- Bunce, E.J., S.W.H. Cowley, I.I. Alexeev, C.S. Arridge, M.K. Dougherty, J.D. Nichols, and C.T. Russell, Cassini observations of the variation of Saturn's ring current parameters with system size, submitted to *J. Geophys. Res.*, 2007.
- Cecconi, B., and P. Zarka: Model of a variable radio period for Saturn, *J. Geophys. Res.*, 110, A12203, doi:10.1029/2005JA011085, 2005.
- Cecconi, B., P. Zarka, and L. Lamy: Goniopolarimetry of the SKR, *Magnetospheres of the Outer Planets 2007 Programme and Abstracts*, p. 192, Southwest Research Institute, San Antonio, USA, 2007.
- Chapman, S. and V.C.A. Ferraro: A new theory of magnetic storms, *Terrest. Magnetism Atmos. Elec.*, 36, 171, 1931.
- Clarke, J.T., H.W. Moos, S.K. Atreya, and A.L. Lane: IUE detection of bursts of H Ly α emission from Saturn, *Nature*, 290, 226, 1981.
- Clarke, J.T., J.-C. Gérard, D. Grodent, S. Wannawichian, J. Gustin, J. Connerney, F. Crary, M. Dougherty, W. Kurth, S.W.H. Cowley, E.J. Bunce, T. Hill, and J. Kim: Morphological differences between Saturn's ultraviolet aurorae and those of Earth and Jupiter, *Nature*, 433, 717, 2005.
- Connerney, J.E.P., M.H. Acuna, N.F. Ness: Saturn's ring current and inner magnetosphere, *Nature*, 292, 724-726, 1981.
- Connerney, J.E.P., M.H. Acuna, N.F. Ness: Currents in Saturn's magnetosphere, *J. Geophys. Res.*, 88, 8779-8789, 1983.
- Connerney, J.E.P., M.H. Acuña, N.F. Ness, and T. Satoh: New models of Jupiter's magnetic field constrained by the Io flux tube footprint, *J. Geophys. Res.*, 103, 11929-11940, 1998.

References

- Cowley, S.W.H.: The distant geomagnetic tail in theory and observation, in *Magnetic Reconnection in Space and Laboratory Plasmas*, edited by E.W. Hones, Jr., American Geophysical Union, Washington, D.C., U.S.A., p. 228-239, 1984.
- Cowley, S.W.H.: The magnetosphere and its interaction with the solar wind and with the ionosphere, in *The Behaviour of Systems in the Space Environment*, edited by R.N. Dewitt, D. Duston, A.K. Hyder, Kluwer Acad. Publ., Dordrecht, p. 147, 1993.
- Cowley, S.W.H., and E.J. Bunce: Origin of the main auroral oval in Jupiter's coupled magnetosphere-ionosphere system, *Planet. Space Sci.*, 49, 1067, 2001.
- Cowley, S.W.H. and E.J. Bunce: Modulation of jovian middle magnetosphere currents and auroral precipitation by solar wind-induced compressions and expansions of the magnetosphere: Initial conditions and steady state, *Planet. Space Sci.*, 51, 31-56, 2003a.
- Cowley, S.W.H. and E.J. Bunce: Modulation of Jupiter's main auroral oval emissions by solar wind-induced expansions and compressions of the magnetosphere, *Planet. Space Sci.*, 51, 57, 2003b.
- Cowley, S.W.H., and E.J. Bunce, Corotation-driven magnetosphere-ionosphere coupling currents in Saturn's magnetosphere and their relation to the auroras, *Ann. Geophys.*, 21, 1691, 2003c.
- Cowley, S.W.H. and M. Lockwood, Excitation and decay of solar wind-driven flows in the magnetosphere-ionosphere system, *Ann. Geophysicae*, 10, 103–115, 1992.
- Cowley, S.W.H., A. Balogh, M.K. Dougherty, M.W. Dunlop, T.M. Edwards, R.J. Forsyth, N.F. Laxton, and K. Staines: Plasma flow in the jovian magnetosphere and related magnetic effects: Ulysses observations, *J. Geophys. Res.*, 101, 15197-15210, 1996.
- Cowley, S.W.H., J.D. Nichols, and E.J. Bunce: Distributions of current and auroral precipitation in Jupiter's middle magnetosphere computed from steady-state Hill-Pontius angular velocity profiles: Solutions for current sheet and dipole magnetic field models, *Planet. Space Sci.*, 50, 717-734, 2002.

- Cowley, S.W.H., E.J. Bunce, T.S. Stallard, and S. Miller: Jupiter's polar ionospheric flows: theoretical interpretation, *Geophys. Res. Lett.*, 30, 1220-1223, doi: 10.1029/2002GL016030, 2003.
- Cowley, S.W.H., E.J. Bunce, and R. Prangé: Saturn's polar ionospheric flows and their relation to the main auroral oval, *Ann. Geophys.*, 22, 1379, 2004a.
- Cowley, S.W.H., E.J. Bunce, and J.M. O'Rourke: A simple quantitative model of plasma flows and currents in Saturn's polar ionosphere, *J. Geophys. Res.*, 109, A05212, doi: 10.1029/2003JA010375, 2004b.
- Cowley, S.W.H., S.V. Badman, E.J. Bunce, J.T. Clarke, J.-C. Gérard, D. Grodent, C.M. Jackman, S.E. Milan, and T.K. Yeoman: Reconnection in a rotation-dominated magnetosphere and its relation to Saturn's auroral dynamics, *J. Geophys. Res.*, 110, A02201, doi:10.1029/2004JA010796, 2005a.
- Cowley, S.W.H., I.I. Alexeev, E.S. Belenkaya, E.J. Bunce, C.E. Cottis, V.V. Kalegaev, J.D. Nichols, R. Prangé, and F.J. Wilson: A simple axi-symmetric model of magnetosphere-ionosphere coupling currents in Jupiter's polar ionosphere, *J. Geophys. Res.*, 110, A11209, doi: 10.1029/2005JA011237, 2005b.
- Cowley, S.W.H., J.D. Nichols, and D.J. Andrews: Modulation of Jupiter's plasma flow, polar currents, and auroral precipitation by solar wind-induced compressions and expansions of the magnetosphere: a simple theoretical model, *Ann. Geophys.*, 25, 1433-1463, 2007.
- Crary, F.J., J.T. Clarke, M.K. Dougherty, P.G. Hanlon, K.C. Hansen, J.T. Steinberg, B.L. Barraclough, A.J. Coates, J.-C. Gérard, D. Grodent, W.S. Kurth, D.G. Mitchell, A.M. Rymer, and D.T. Young: Solar wind dynamic pressure and electric field as the main factors controlling Saturn's auroras, *Nature*, 433, 720, 2005.
- Davis, L., Jr., and E.J. Smith: A model of Saturn's magnetic field based on all available data, *J. Geophys. Res.*, 95, 15257, 1990.

References

- Desch, M.D.: Evidence for solar wind control of Saturn radio emission, *J. Geophys. Res.*, 87, 4549, 1982.
- Desch, M.D., and M.L. Kaiser: Voyager measurement of the rotation period of Saturn's magnetic field, *Geophys. Res. Lett.*, 8, 253-256, 1981a.
- Desch, M.D., and M.L. Kaiser: Saturn Kilometric Radiation: satellite modulation, *Nature*, 292, 739-741, 1981b.
- Desch, M.D., and H.O. Rucker: The relationship between Saturn kilometric radiation and the solar wind, *J. Geophys. Res.*, 88, 8999, 1983.
- Dessler, A.: Differential rotation of the magnetic fields of gaseous planets, *Geophys. Res. Lett.*, 12, 299-302, 1985.
- Dougherty, M.K., S. Kellock, D.J. Southwood, A. Balogh, E.J. Smith, B.T. Tsurutani, B. Gerlach, K.-H. Glassmeier, F. Gleim, C.T. Russell, G. Erdos, F.M. Neubauer, and S.W.H. Cowley: The Cassini magnetic field investigation, *Space Sci. Rev.*, 114, 331-383, 2004.
- Dougherty, M.K., N. Achilleos, N. Andre, C.S. Arridge, A. Balogh, C. Bertucci, M.E. Burton, S.W.H. Cowley, G. Erdos, G. Giampieri, K.-H. Glassmeier, K.K. Khurana, J.S. Leisner, F.M. Neubauer, C.T. Russell, E.J. Smith, D.J. Southwood, B.T. Tsurutani: Cassini magnetometer observations during Saturn orbit insertion, *Science*, 307, 1266-1270, 2005.
- Dougherty, M.K., K.K. Khurana, F.M. Neubauer, C.T. Russell, J. Saur, J.S. Leisner, M.E. Burton: Identification of a dynamic atmosphere at Enceladus with the Cassini magnetometer, *Science*, 311, 1406-1409, 2006.
- Dungey, J.W.: Interplanetary field and the auroral zones, *Phys. Rev. Lett.*, 6, 47, 1961.
- Fairfield, D.H.: Average magnetic field configuration of the outer magnetosphere, *J. Geophys. Res.*, 73, 7329-7338, 1968.

References

- Frank, L.A., W.R. Paterson, and K.K. Khurana: Observations of thermal plasmas in Jupiter's magnetotail, *J. Geophys. Res.*, 107, A11003, doi: 10.1029/2001JA000077, 2002.
- Frank, W.A. and W.R. Paterson: Plasmas observed near local noon in Jupiter's magnetosphere with the Galileo spacecraft, *J. Geophys. Res.*, 109, A11217, doi: 10.1029/2002JA009795, 2004.
- Galopeau, P.H.M. and A. Lecacheux: Variations of Saturn's radio rotation period at kilometre wavelengths, *J. Geophys. Res.*, 105, 13089-13102, 2000.
- Galopeau, P.H.M., P. Zarka, and D. Le Queau: Source location of Saturn's kilometric radiation: The Kelvin-Helmholtz instability hypothesis, *J. Geophys. Res.*, 100, 26397-26410, 1995.
- Gérard, J.-C., V. Dols, D. Grodent, J.H. Waite, G.R. Gladstone, and R. Prangé: Simultaneous observations of the saturnian aurora and polar haze with the HST/FOC, *Geophys. Res. Lett.*, 22, 2685, 1995.
- Gérard, J.-C., D. Grodent, J. Gustin, A. Saglam, J.T. Clarke, and J.T. Trauger: Characteristics of Saturn's FUV aurora observed with the Space Telescope Imaging Spectrograph, *J. Geophys. Res.*, 109, doi:10.1029/2004JA010513, 2004.
- Gérard, J.-C., E.J. Bunce, D. Grodent, S.W.H. Cowley, J.T. Clarke and S.V. Badman: Signature of Saturn's auroral cusp: Simultaneous HST FUV observations and upstream solar wind monitoring, *J. Geophys. Res.*, 110, A11201, doi:10.1029/2005JA011094, 2005.
- Gérard, J.-C., D. Grodent, S.W.H. Cowley, D.G. Mitchell, W.S. Kurth, J.T. Clarke, E.J. Bunce, J.D. Nichols, M.K. Dougherty, F.J. Crary, and A.J. Coates: Saturn's auroral morphology and activity during quiet magnetospheric conditions, *J. Geophys. Res.*, 111, doi:10.1029/2006JA011965, 2006.
- Giampieri, G. and M.K. Dougherty: Rotation rate of Saturn's interior from magnetic field observations, *Geophys. Res. Lett.*, 31, doi: 10.1029/2004GL020194, 2004.

References

- Gong, B. and T.W. Hill: Variations of jovian and saturnian auroras induced by changes of solar wind dynamic pressure, *Magnetospheres of the Outer Planets 2005 Programme and Abstracts*, p. 129, University of Leicester, Leicester, UK, 2005.
- Gosling, J.T., and V.J. Pizzo: Formation and evolution of corotating interaction regions and their three dimensional structure, *Space Sci. Rev.*, 89, 21, 1999.
- Grodent, D., J.T. Clarke, J. Kim, J.H. Waite, Jr., and S.W.H. Cowley: Jupiter's main auroral oval observed with HST-STIS, *J. Geophys. Res.*, 108, 1389, doi:10.1029/2003JA009921, 2003.
- Grodent, D., J.-C. Gérard, S.W.H. Cowley, E.J. Bunce, and J.T. Clarke: Variable morphology of Saturn's southern ultraviolet aurora, *J. Geophys. Res.*, 110, doi:10.1029/2004JA010983, 2005.
- Guillot, T., G. Chabrier, D. Gautier, and P. Morel: Effect of radiative transport on the evolution of Jupiter and Saturn, *Astrophys. J.*, 450, 463-472, 1995.
- Gurnett, D.A.: The earth as a radio source: terrestrial kilometric radiation, *J. Geophys. Res.*, 79, 4227-4238, 1974.
- Gurnett, D.A., W.S. Kurth, and F.L. Scarf: Plasma waves near Saturn: Initial results from Voyager 1, *Science*, 212, 235-239, 1981.
- Gurnett, D.A., W.S. Kurth, D.L. Kirchner, G.B. Hospodarsky, T.F. Averkamp, P. Zarka, A. Lecacheux, R. Manning, A. Roux, P. Canu, N. Cornilleau-Wehrin, P. Galopeau, A. Meyer, R. Boström, G. Gustafsson, J.-E. Wahlund, L. Åhlen, H.O. Rucker, H.P. Ladreiter, W. Macher, L.J.C. Woolliscroft, H. Alleyne, M.L. Kaiser, M.D. Desch, W.M. Farrell, C.C. Harvey, P. Louarn, P.J. Kellogg, K. Goetz and A. Pedersen: The Cassini Radio and Plasma Wave Investigation, *Space Sci. Rev.*, 114, 395-463, 2004.

References

- Gurnett, D.A., W.S. Kurth, G.B. Hospodarsky, A. Persoon, T.F. Averkamp, B. Cecconi, A. Lecacheux, P. Zarka, P. Canu, N. Cornilleau-Wehrin, P. Galopeau, A. Roux, C. Harvey, P. Louarn, R. Boström, G. Gustafsson, J.-E. Wahlund, M.D. Desch, W.M. Farrell, M.L. Kaiser, K. Goetz, P.J. Kellogg, G. Fischer, H.-P. Ladreiter, H.O. Rucker, H. Alleyne, A. Pedersen: Radio and plasma wave observations at Saturn from Cassini's approach and first orbit, *Science*, 307, 1255–1259, 2005.
- Hansen, C.J., L. Esposito, I.A.F. Stewart, J. Colwell, A. Hendrix, W. Pryor, D. Shemansky, and R. West: Enceladus' water vapor plume, *Science*, 311, 422-425, 2006.
- Hartle, R.E., E.C. Sittler, Jr., F.M. Neubauer, R.E. Johnson, H.T. Smith, F. Crary, D.J. McComas, D.T. Young, A.J. Coates, D. Simpson, S. Bolton, D. Reisenfeld, K. Szego, J.J. Berthelier, A. Rymer, J. Vilppola, J.T. Steinberg, and N. André: Preliminary interpretation of Titan plasma interaction as observed by the Cassini Plasma Spectrometer: Comparisons with Voyager 1, *Geophys. Res. Lett.*, 33, doi: 10.1029/2005GL024817, 2006.
- Hill, T.W.: Inertial limit on corotation, *J. Geophys. Res.*, 84, 6554, 1979.
- Hill, T.W.: The jovian auroral oval, *J. Geophys. Res.*, 106, 8101, 2001.
- Hundhausen, A.J.: The solar wind, in *Introduction to Space Physics*, edited by M.G. Kivelson and C.T. Russell, p91, Cambridge Univ. Press, Cambridge, UK, 1995.
- Hughes, W.J.: The magnetopause, magnetotail and magnetic reconnection, in *Introduction to Space Physics*, edited by M.G. Kivelson and C.T. Russell, p227, Cambridge Univ. Press, Cambridge, UK, 1995.
- Isbell, J., A.J. Dessler, J.H. Waite, Jr.: Magnetospheric energization by interaction between planetary spin and the solar wind, *J. Geophys. Res.*, 89, 10 716, 1984.

References

- Jackman, C.M., N. Achilleos, E.J. Bunce, S.W.H. Cowley, M.K. Dougherty, G.H. Jones, S.E. Milan, and E.J. Smith: Interplanetary magnetic field at ~9 AU during the declining phase of the solar cycle and its implications for Saturn's magnetospheric dynamics, *J. Geophys. Res.*, 109, doi:10.1029/2004JA010614, 2004.
- Jackman, C.M., N. Achilleos, E.J. Bunce, B. Cecconi, J.T. Clarke, S.W.H. Cowley, W.S. Kurth, and P. Zarka: Interplanetary conditions and magnetospheric dynamics during the Cassini orbit insertion fly-through of Saturn's magnetosphere, *J. Geophys. Res.*, 110, A10212, doi: 10.1029/2005JA011054, 2005.
- Jackman, C.M. and S.W.H. Cowley: A model of the plasma flow and current in Saturn's polar ionosphere under conditions of strong Dungey-cycle driving, *Ann. Geophysicae*, 24, 1029-1055, 2006.
- Jackman, C.M., N. Achilleos, C.S. Arridge, H.J. McAndrews, D.G. Mitchell, W.S. Kurth, T.W. Hill, N. Krupp, C.T. Russell, M.K. Dougherty, E.J. Bunce, and A.J. Coates: A multi-instrument view of tail reconnection at Saturn, *Magnetospheres of the Outer Planets 2007 Programme and Abstracts*, p. 96, Southwest Research Institute, San Antonio, USA, 2007.
- Joy, S.P., M.G. Kivelson, R.J. Walker, K.K. Khurana, C.T. Russell, and T. Ogino: Probabilistic models of the jovian magnetopause and bow shock locations, *J. Geophys. Res.*, 107, 1309-1325, doi: 10.1029/2001JA009146, 2002.
- Judge, D.L., F.M. Wu, and R.W. Carlson: Ultraviolet photometer observations of the Saturnian system, *Science*, 207, 431, 1980.
- Jurac, S. and J.D. Richardson: A self-consistent model of plasma and neutrals at Saturn: Neutral cloud morphology, *J. Geophys. Res.*, 110, doi: 10.1029/2004JA010635, 2005.
- Jurac, S., M.A. McGrath, R.E. Johnson, J.D. Richardson, V.M. Vasyliunas, A. Eviatar: Saturn: Search for a missing water source, *Geophys. Res. Lett.*, 29, doi:10.1029/2002GL015855, 2002.

References

- Kaiser, M.L., M.D. Desch, J.W. Warwick, J.B. Pearce, Voyager detection of non-thermal radio emission from Saturn, *Science*, 209, 1238-1240, 1980.
- Kane, M., B.H. Mauk, E.P. Keath, and S.M. Krimigis: Hot ions in the jovian magnetodisc: A model for Voyager 2 low-energy charged particle measurements, *J. Geophys. Res.*, 100, 19473-19486, 1995.
- Kennel, C.F. and F.V. Coroniti: Is Jupiter's magnetosphere like a pulsar's or Earth's?, in: *The magnetospheres of Earth and Jupiter*, edited by: Formisano, V., D. Reidel, Norwell, Mass., p. 451-477, 1975.
- Khurana, K.K. and M.G. Kivelson: Inference of the angular velocity of plasma in the jovian magnetosphere from the sweepback of magnetic field, *J. Geophys. Res.*, 98, 67-80, 1993.
- Kivelson, M.G. and D.J. Southwood: Dynamical consequences of two modes of centrifugal instability in Jupiter's outer magnetosphere, *J. Geophys. Res.*, 110, A12209, doi: 10.1029/2003JA011176, 2005.
- Krimigis, S.M., D.G. Mitchell, D.C. Hamilton, et al.: Dynamics of Saturn's magnetosphere from MIMI during Cassini's orbital insertion, *Science*, 307, 1270-1273, 2005.
- Kronberg, E.A., J. Woch, N. Krupp, A. Lagg, K.K. Khurana, and K.-H. Glassmeier: Mass release at Jupiter: Substorm-like processes in the jovian magnetotail, *J. Geophys. Res.*, 110, A03211, doi: 10.1029/2004JA010777, 2005.
- Krupp, N., A. Lagg, S. Livi, B. Wilken, J. Woch, E.C. Roelof, and D.J. Williams: Global flows of energetic ions in Jupiter's equatorial plane: First-order approximation, *J. Geophys. Res.*, 106, 26017-26032, 2001.
- Krupp, N., A. Lagg, J. Woch, S.M. Krimigis, S. Livi, D.G. Mitchell, E.C. Roelof, C. Paranicas, B.H. Mauk, D.C. Hamilton, T.P. Armstrong, and M.K. Dougherty: The Saturnian plasma sheet as revealed by energetic particle measurements, *Geophys. Res. Lett.*, 32, doi: 10.1029/2005GL022829, 2005.

References

- Kurth, W.S., J.D. Sullivan, D.A. Gurnett, F.L. Scarf, H.S. Bridge, and E.C. Sittler Jr., Observations of Jupiter's distant magnetotail and wake, *J. Geophys. Res.*, 87, 10373, 1983.
- Kurth, W.S., D.A. Gurnett, J.T. Clarke, P. Zarka, M.D. Desch, M.L. Kaiser, B. Cecconi, A. Lecacheux, W.M. Farrell, P. Galopeau, J.-C. Gérard, D. Grodent, R. Prangé M.K. Dougherty, and F.J. Crary: An Earth-like correspondence between Saturn's auroral features and radio emission, *Nature*, 433, 722, 2005.
- Kurth, W.S., A. Lecacheux, T.F. Averkamp, J.B. Groene, and D.A. Gurnett: A Saturnian longitude system based on a variable kilometric radiation period, *Geophys. Res. Lett.*, 34, doi:10.1029/2006GL028336, 2007.
- Lyons L.R., G.T. Blanchard, J.C. Samson, R.P. Lepping, T. Yamamoto, T. Moretto: Coordinated observations demonstrating external substorm triggering, *J. Geophys. Res.*, 102, 27039, 1997.
- McGrath, M.A., and J.T. Clarke: HI Lyman alpha emission from Saturn (1980-1990), *J. Geophys. Res.*, 97, 13691, 1992.
- Menietti, J.D., J.B. Groene, T.F. Averkamp, G.B. Hospodarsky, W.S. Kurth, D.A. Gurnett, P. Zarka: The influence of Saturnian moons on SKR, submitted to *J. Geophys. Res.*, 2007.
- Meurant, M., J.-C. Gérard, C. Blockx, B. Hubert, and V. Coumans: Propagation of electron and proton shock-induced aurora and the role of the interplanetary magnetic field and solar wind, *J. Geophys. Res.*, 109, doi: 10.1029/2004JA010453, 2004.
- Milan, S.E., M. Lester, S.W.H. Cowley, K. Oksavik, M. Brittnacher, R.A. Greenwald, G. Sofko, and J.-P. Villain: Variations in polar cap area during two substorm cycles, *Ann. Geophys.*, 21, 1121, 2003.

References

- Milan, S.E., S.W.H. Cowley, M. Lester, D.M. Wright, J.A. Slavin, M. Fillingim, C.W. Carlson, and H.J. Singer: Response of the magnetotail to changes in the open flux content of the magnetosphere, *J. Geophys. Res.*, 109, doi: 10.1029/2003JA010350, 2004.
- Milan, S.E., J.A. Wild, A. Grocott, and N.C. Draper: Space- and ground-based investigations of solar wind-magnetosphere-ionosphere coupling, *Adv. Space Res.*, 38, 1671-1677, 2006.
- Milan, S.E., G. Provan, and B. Hubert: Magnetic flux transport in the Dungey cycle: A survey of dayside and nightside reconnection rates, *J. Geophys. Res.*, 112, A01209, doi: 10.1029/2006JA011642, 2007.
- Millward G., S. Miller, T. Stallard, A.D. Aylward, N. Achilleos: On the dynamics of the jovian ionosphere and thermosphere III: The modelling of auroral conductivity, *Icarus*, 160, 95-107, 2002.
- Mitchell, D.G., P.C. Brandt, E.C. Roelof, J. Dandouras, S.M. Krimigis, B.H. Mauk, C.P. Paranicas, N. Krupp, D.C. Hamilton, W.S. Kurth, P. Zarka, M.K. Dougherty, E.J. Bunce, D.E. Shemansky: Energetic ion acceleration in Saturn's magnetotail: Substorms on Saturn?, *Geophys. Res. Lett.*, 32, No. 20, L20S01 doi: 10.1029/2005GL022647, 2005.
- Ness, N.F.: Magnetometers for space research, *Space Sci. Rev.*, 11, 459-554, 1970.
- Ness, N.F., M.H. Acuña, R.P. Lepping, J.E.P. Connerney, K.W. Behannon, L.F. Burlaga, and F.M. Neubauer: Magnetic field studies by Voyager 1: Preliminary results at Saturn, *Science*, 212, 211, 1981.
- Ness, N.F., M.H. Acuña, K.W. Behannon, L.F. Burlaga, J.E.P. Connerney, R.P. Lepping, and F.M. Neubauer: Magnetic field studies by Voyager 2: Preliminary results at Saturn, *Science*, 215, 558-563, 1982.

References

- Nichols, J.D. and S.W.H. Cowley, Magnetosphere-ionosphere coupling currents in Jupiter's middle magnetosphere: Effect of precipitation-induced enhancement of the ionospheric Pedersen conductivity, *Ann. Geophys.*, 22, 1799, 2004.
- Nichols, J.D. and S.W.H. Cowley: Magnetosphere-ionosphere coupling currents in Jupiter's middle magnetosphere: effect of magnetosphere-ionosphere decoupling by field-aligned auroral voltages, *Ann. Geophys.*, 23, 799-808, 2005.
- Nichols J.D., S.W.H. Cowley, and D.J. McComas: Magnetopause reconnection rate estimates for Jupiter's magnetosphere based on interplanetary measurements at ~5AU, *Ann. Geophys.*, 24, 393-406, 2006.
- Nichols, J.D., E.J. Bunce, J.T. Clarke, S.W.H. Cowley, J.-C. Gérard, D. Grodent, and W.R. Pryor: Response of Jupiter's UV auroras to interplanetary conditions as observed by the Hubble Space Telescope during the Cassini fly-by campaign, *J. Geophys. Res.*, 112, A02203, doi: 10.1029/2006JA012005, 2007.
- Parker, E.N.: Dynamics of the interplanetary magnetic field, *Astrophys. J.*, 128, 664, 1958.
- Peredo, M., J.A. Slavin, E. Mazur, and S.A. Curtis: Three-dimensional position and shape of the bowshock and their variation with Alfvénic, sonic and magnetosonic Mach numbers and interplanetary magnetic field orientation, *J. Geophys. Res.*, 100, 7907-7916, 1995.
- Perrault, P. and S.-I. Akasofu: A study of geomagnetic storms, *Geophys. J. R. Astron. Soc.*, 54, 547-573, 1978.
- Pontius, D.H., Jr.: Radial mass transport and rotational dynamics, *J. Geophys. Res.*, 102, 7137-7150, 1997.
- Porco, C.C., P. Helfenstein, P.C. Thomas, A.P. Ingersoll, J. Wisdom, R. West, G. Neukum, T. Denk, R. Wagner, T. Roatsch, S. Kieffer, E. Turtle, A. McEwen, T.V. Johnson, J. Rathbun, J. Veverka, D. Wilson, J. Perry, J. Spitale, A. Brahic, J.A. Burns, A.D. DelGenio, L. Dones, C.D. Murray, and S. Squyres: Cassini observes the active south pole of Enceladus, *Science*, 311, 1393-1401, 2006.

References

- Prangé, R., L. Pallier, K.C. Hansen, R. Howard, A. Vourlidas, R. Courtin, and C. Parkinson: An interplanetary shock traced by planetary auroral storms from the Sun to Saturn, *Nature*, 432, 78, 2004.
- Priest, E.R.: The Sun and its magnetohydrodynamics, in *Introduction to Space Physics*, edited by M.G. Kivelson and C.T. Russell, p58, Cambridge Univ. Press, Cambridge, UK, 1995.
- Radioti, A., N. Krupp, J. Woch, A. Lagg, K.-H. Glassmeier, and L.S. Waldrop: Ion abundance ratios in the Jovian magnetosphere, *J. Geophys. Res.*, 110, A07225, doi: 10.1029/2004JA010775, 2005.
- Rego, D., R. Prangé, and J.-C. Gérard: Lyman α and H₂ bands from the giant planets: 1. Excitation by proton precipitation in the jovian aurorae, *J. Geophys. Res.*, 99, 17 075, 1994.
- Richardson, J.D.: Thermal ions at Saturn: Plasma parameters and implications, *J. Geophys. Res.*, 91, 1381-1389, 1986.
- Richardson, J.D. and E.C. Sittler, Jr.: A plasma density model for Saturn based on Voyager observations, *J. Geophys. Res.*, 95, 12019-12031, 1990.
- Russell, C.T. and R.J. Walker: The magnetospheres of the outer planets, in *Introduction to Space Physics*, edited by M.G. Kivelson and C.T. Russell, p503, Cambridge Univ. Press, Cambridge, UK, 1995.
- Russell, C.T., K.K. Khurana, D.E. Huddleston, M.G. Kivelson: Localized reconnection in the near jovian magnetotail, *Science*, 280, 1061-1064, 1998.
- Sandel, B.R., and A.L. Broadfoot: Morphology of Saturn's aurora, *Nature*, 292, 679, 1981.

References

- Sandel, B.R., D.E. Shemansky, A.L. Broadfoot, J.B. Holberg, G.R. Smith, J.C. McConnell, D.F. Strobel, S.K. Atreya, T.M. Donahue, H.W. Moos, D.M. Hunten, R.B. Pomphrey, and S. Linik: Extreme ultraviolet observations from the Voyager 2 encounter with Saturn, *Science*, 215, 548, 1982.
- Sergis, N., S.M. Krimigis, D.G. Mitchell, D.C. Hamilton, N. Krupp, B.M. Mauk, E.C. Roelof, and M.K. Dougherty: Ring current at Saturn: Energetic particle pressure in Saturn's equatorial magnetosphere measured with Cassini/MIMI, *Geophys. Res. Lett.*, 34, doi:10.1029/2006GL029223, 2007.
- Shemansky, D.E. and J.M. Ajello: The Saturn spectrum in the EUV: Electron excited hydrogen, *J. Geophys. Res.*, 88, 459, 1983.
- Shemansky, D.E., P. Matheson, D.T. Hall, H.-Y. Hu, and T.M. Tripp: Detection of the hydroxyl radical in the Saturn magnetosphere, *Nature*, 363, 329-331, 1993.
- Sibeck, D.G., R.E. Lopez, E.C. Roelof: Solar wind control of the magnetopause shape location and motion, *J. Geophys. Res.*, 96, 5489–5495, 1991.
- Siscoe, G. L. and Huang, T. S.: Polar cap inflation and deflation, *J. Geophys. Res.*, 90, 543–547, 1985.
- Sittler, E.C., Jr., M. Thomsen, D. Chornay, M.D. Shappirio, D. Simpson, R.E. Johnson, H.T. Smith, A.J. Coates, A.M. Rymer, F. Crary, D.J. McComas, D.T. Young, D. Reisenfeld, M.K. Dougherty, and N. Andre: Preliminary results on Saturn's inner plasmasphere as observed by Cassini: Comparison with Voyager, *Geophys. Res Lett.*, 32, doi: 10.1029/2005GL022653, 2005.
- Southwood, D.J. and M.G. Kivelson: A new perspective concerning the influence of the solar wind on Jupiter, *J. Geophys. Res.*, 106, 6123, 2001.
- Stallard, T.S., S. Miller, L.M. Trafton, T.R. Geballe, and R.D. Joseph: Ion winds in Saturn's southern auroral/polar region, *Icarus*, 167, 2004.

- Stallard, T.S., S. Miller, H. Melin, M. Lystrup, M.K. Dougherty, N. Achilleos: Saturn's auroral/polar infrared H_3^+ emission I: General morphology and ion velocity structure, *Icarus*, 189, 2007.
- Szego, K., Z. Bebesi, G. Erdos, L. Foldy, F. Crary, D.J. McComas, D.T. Young, S. Bolton, A.J. Coates, A.M. Rymer, R.E. Hartle, E.C. Sittler, D. Reisenfeld, J.J. Bethelier, R.E. Johnson, H.T. Smith, T.W. Hill, J. Vilppola, J. Steinberg, N. Andre: The global plasma environment of Titan as observed by Cassini Plasma Spectrometer during the first two close encounters with Titan, *Geophys. Res. Lett.*, 32, L20S05, doi: 10.1029/2005GL022646, 2005.
- Tokar, R.L., R.E. Johnson, T.W. Hill, D.H. Pontius, W.S. Kurth, F.J. Crary, D.T. Young, M.F. Thomsen, D.B. Reisenfeld, A.J. Coates, G.R. Lewis, E.C. Sittler, and D.A. Gurnett: The interaction of the atmosphere of Enceladus with Saturn's plasma, *Science*, 311, 1409-1412, 2006.
- Trauger, J.T., J.T. Clarke, G.E. Ballester, R.W. Evans, C.J. Burrows, D. Crisp, J.S. Gallagher, III, R.E. Griffiths, J.J. Hester, J.G. Hoessel, J.A. Holtzman, J.E. Krist, J.R. Mould, R. Sahai, P.A. Scowen, K.R. Stapelfeldt, and A.M. Watson: Saturn's hydrogen aurora: Wide field and planetary camera 2 imaging from the Hubble Space Telescope, *J. Geophys. Res.*, 103, 20 237, 1998.
- Vasyliunas, V.M.: Plasma distribution and flow, in *Physics of the Jovian Magnetosphere*, edited by A.J. Dessler, p. 395, Cambridge Univ. Press, Cambridge, UK, 1983.
- Waite, J.H., Jr., T.E. Cravens, J. Kozyra, A.F. Nagy, S.K. Atreya, and R.H. Chen: Electron precipitation and related aeronomy of the jovian thermosphere and ionosphere, *J. Geophys. Res.* 88, 6143, 1983.
- Waite, J.H., Jr., T.E. Cravens, W.-H. Ip, W.T. Kasprzak, J.G. Luhmann, R.L. McNutt, H.B. Niemann, R.V. Yelle, I. Mueller-Wodarg, S.A. Ledvina, and S. Scherer: Oxygen ions observed near Saturn's A ring, *Science*, 307, 1260-1262, 2005.
- Waite, J.H., Jr., M.R. Combi, W.-H. Ip, T.E. Cravens, R.L. McNutt, Jr., W. Kasprzak, R. Yelle, J. Luhmann, H. Niemann, D. Gell, B. Magee, G. Fletcher, J. Lunine, and

References

- W.-L. Tseng: Cassini Ion and Neutral Mass Spectrometer: Enceladus plume composition and structure, *Science*, 311, 1419-1422, 2006.
- Warwick, J.W., D.R. Evans, J.H. Romig, J.K. Alexander, M.D. Desch, M.L. Kaiser, M. Aubier, Y. Leblanc, A. Lecacheux, B.M. Pedersen: Planetary radio astronomy observations from Voyager 2 near Saturn, *Science*, 215, 582-587, 1982.
- Williams, J.D., D.B. Reisenfeld, H. Martens, J. Dilorenzo, M. Thomsen, H.T. Smith, R.E. Johnson, D.T. Young, E.C. Sittler, Jr., and R.A. Baragiola: Abundances and energetics for water group and molecular oxygen ions in Saturn's magnetosphere after 24 Cassini orbits, *Magnetospheres of the Outer Planets 2007 Programme and Abstracts*, p. 137, Southwest Research Institute, San Antonio, USA, 2007.
- Woch, J., N. Krupp, K.K. Khurana, M.G. Kivelson, A. Roux, S. Perraut, P. Louarn, A. Lagg, D.J. Williams, S. Livi, and B. Wilken: Plasma sheet dynamics in the Jovian magnetotail: Signatures for substorm-like processes?, *Geophys. Res. Lett.*, 26, 2137-2140, 1999.
- Woch, J., N. Krupp, A. Lagg, and A. Tomás: The structure and dynamics of the jovian energetic particle distribution, *Adv. Space. Res.*, 33, 2030-2038, 2004.
- Woodgate, B.E., R.A. Kimble, C.W. Bowers, et al., The space telescope imaging spectrograph design, *Publications of the Astronomical Society of the Pacific*, 110, 1183-1204, 1998.
- Wu, C.S. and L.C. Lee, A theory of the terrestrial kilometric radiation, *Astrophys. J.*, 230, 621-626, 1979.
- Young, D.T., J.-J. Berthelier, M. Blanc et al.: The Cassini plasma spectrometer investigation, *Space Sci. Rev.*, 114, 1-112, 2004.
- Young, D.T., J.-J. Berthelier, M. Blanc, et al.: Composition and dynamics of plasma in Saturn's magnetosphere, *Science*, 307, 1262-1266, 2005.

References

Zarka, P.: Auroral radio emissions at the outer planets: observations and theory, J. Geophys. Res., 103, 20159-20194, 1998.

Zarka, P. and W.S. Kurth: Radio wave emission from the outer planets before Cassini, Space Sci. Rev., 116, 371-397, 2005.